3-12-2004

Experimental Investigation into the Aerodynamic Performance of Both Rigid and Flexible Wing Structured Micro-Air-Vehicles

Anthony M. DeLuca

EXPERIMENTAL INVESTIGATION INTO THE AERODYNAMIC PERFORMANCE OF BOTH RIGID AND FLEXIBLE WING STRUCTURED MICRO-AIR-VEHICLES

THESIS

Anthony M. DeLuca, Captain, USAF

AFIT/GAE/ENY/04-M06

DEPARTMENT OF THE AIR FORCE
AIR UNIVERSITY

AIR FORCE INSTITUTE OF TECHNOLOGY

Wright-Patterson Air Force Base, Ohio

The views expressed in this thesis are those of the author and do not reflect the official policy or position of the United States Air Force, Department of Defense, or the United States Government.

AFIT/GAE/ENY/04-M06

EXPERIMENTAL INVESTIGATION INTO THE AERODYNAMIC PERFORMANCE OF BOTH RIGID AND FLEXIBLE WING STRUCTURED MICRO-AIR-VEHICLES

THESIS

Presented to the Faculty

Department of Aeronautics and Astronautics

Graduate School of Engineering and Management

Air Force Institute of Technology

Air University

Air Education and Training Command

In Partial Fulfillment of the Requirements for the

Degree of Master of Science in Aeronautical Engineering

Anthony M. DeLuca, B.S.M.E, MBA

Capt, USAF

March 2004

AFIT/GAE/ENY/04-M06

EXPERIMENTAL INVESTIGATION INTO THE AERODYNAMIC PERFORMANCE OF BOTH RIGID AND FLEXIBLE WING STRUCTURED MICRO-AIR-VEHICLES

Anthony M. DeLuca, B.S.M.E, MBA
Capt, USAF

Approved:

//SIGNED//	12 March 2004
Dr. Mark F. Reeder	date
(Committee Chairman)	
//SIGNED//	12 March 2004
Dr. Ralph A. Anthenien	date
(Committee Member)	
//SIGNED//	12 March 2004
Lt. Col Montgomery C. Hughson, PhD, USAF	date
(Committee Member)	

AFIT/GAE/ENY/04-M06

Abstract

The Air Force Research Lab, Munitions Directorate, Eglin Air Force Base, Florida has designed a man-portable carbon-fiber Micro-Air-Vehicle (MAV) used for on-the-spot surveillance by Special Operations Forces (SOF) for enemy reconnaissance as well as post-strike Battle Damage Assessment (BDA).

The main goals of this experiment are: 1) characterize the flow quality of the new AFIT 3' x 3' wind tunnel and 2) determine the aerodynamic performance characteristics of the 24″ span, 6″ chord flexible and rigid wing MAVs. The freestream turbulence intensity of the wind tunnel was approximately 2%. Both MAVs had an average lift slope within 3.5% of the theoretical value. Flexible wings deformed in response to perturbations in local flow field conditions, promulgating the delay of wing stall by nearly double. Aeroelastic effects begin to dominate low speed, laminar Reynolds number effects at tunnel velocities greater than 30 miles per hour. The flexible wing MAV displayed static stability in all three principal control axes (Pitch, Roll, Yaw), while the rigid MAV was not definitively stable in any axis. All flexible wing control surface configurations resulted in predictable and consistent performance between -10° and +10° elevon deflection. Reponses declined steadily after ±10° showing dramatic direction changes.

Acknowledgements

The accomplishment of this experiment and subsequent writing of this manuscript were only possible through the trust and tireless devotion of those involved. At the first level, my lab technician, Mr. Dwight Gehring, did a yeoman's job troubleshooting the wind tunnel and seeing that the numerous "bugs" in the LabView software were conquered before the start of any testing. He expertly calibrated and installed the balance and the MAV in the wind tunnel and assisted in "tweaking" the model to work in our experiment. I want to thank the team members at Eglin's Air Force Research Lab, Munitions Directorate, for giving me such an intriguing and challenging task and having the patience to wait through my slow, but methodical process of data reduction before demanding any results. My thesis advisor, Dr. Mark Reeder, was a great confidant and friend. He gave me support where needed, freedom to find my way, and championed my progress to others when necessary—a true blessing throughout. My wife, we were newlyweds upon arrival at AFIT, and since then, has suffered through more lonely nights than reasonably expected. Her love, understanding, patience, support, affection, and numerous other attributes, whose effects were incalculable, can never be repaid-thank-you. Finally, my Lord God above provided me a never-ending source of strength, humility, and encouragement without which, nothing written hereafter would be possible.

Anthony M. DeLuca

Table of Contents

Page

List of Figures

Figure Page

Page

Page

Page

List of Tables

Table Page

Page

Page

Page

List of Symbols

A	Axial Force (Body Axis)
Y	Side Force (Body Axis)
N	Normal Force (Body Axis)
D	Drag Force (Wind Axis)
S	Side Force (Wind Axis)
L	Lift Force (Wind Axis)
N_1 & N_2	Balance Normal Sensors
S_1 & S_2	Balance Side Sensors
A_1	Balance Axial Sensor
$\boldsymbol{\ell}_1$	Balance Roll Moment Sensor
AR	Aspect Ratio
S	Wing Area
C	Wing Root Chord
$\bar{c}$	Wing Mean Chord
Re_c	Reynolds Number at the Chord
L/D	Lift-to-Drag Ratio
M	Mach Number
T	Thrust
P	Power
R	Ideal Gas Constant
J	Advance Ratio
CG	Center of Gravity
RPM	Revolutions Per Minute
RPS	Revolutions Per Second
M.A.C.	Mean Aerodynamic Center
MAV	Micro-Air-Vehicle
2b	Wing Span
m	Lift Curve Slope
m_o	Elliptical or Theoretical Lift Slope
$q\infty$	Far Field Dynamic Pressure
$U\infty$	Far Field Velocity
a	Speed of Sound
$\boldsymbol{\ell}$	Roll Moment
$\boldsymbol{m}$	Pitch Moment
$\boldsymbol{n}$	Yaw Moment
ρ	Air Density
μ	Air Viscosity
γ	Ratio of Specific Heats (c_p / c_T)
τ_w	Shear at the Wall
α	Angle of Attack ($\alpha = \theta$)
α_{Stall}	Angle of Wing Stall

α_{LO}	Angle of Zero Lift
β	Sideslip Angle
ψ	Yaw Angle ($\psi = -\beta$)
Γ	Wing Dihedral Angle
Φ	Wing Roll Angle
δ_e	Elevon Deflection Angle
C_T	Thrust Coefficient
C_P	Power Coefficient
C_L	Lift Coefficient
C_Y	Side Force Coefficient
C_D	Drag Force Coefficient
C_{ℓ}	Roll Moment Coefficient
C_m	Pitch Moment Coefficient
C_n	Yaw Moment Coefficient
$C_{m\alpha}$	Longitudinal Stability Derivative
$C_{n\beta}$	Directional Stability Derivative
$C_{\ell\beta}$	Roll Stability Derivative
lb_f	Pounds Force
lb_m	Pounds Mass
$''$	Inches
$'$	Feet
$^\circ$	Degrees ($360^\circ = 2\pi$ radians)

EXPERIMENTAL INVESTIGATION INTO THE AERODYNAMIC PERFORMANCE OF BOTH RIGID AND FLEXIBLE WING STRUCTURED MICRO-AIR-VEHICLES

I. Introduction

Background

The tremendous success of Unmanned Aerial Vehicles (UAVs) in both military and civilian applications has prompted academic institutions to pursue greater innovations in the arena of unmanned powered flight. UAVs were initially designed as Intelligence, Surveillance, and Reconnaissance (ISR) gathering platforms, which carry an array of cameras, sensors, and communications equipment (fas.org). The Global War on Terror presents a new facet of military warfare for the United States; reclusive enemies using unconventional tactics require leading edge combat capabilities. As a result, the UAV's mission is expanding to include direct combat missions with UAVs capable of autonomous target acquisition and attack as well as unit level deployables. Military acquisition of UAVs began in 1964; of the 11 Department of Defense (DoD) UAV acquisition programs, three have been successfully funded through full production (fas.org). The three successful UAV programs, Hunter, Predator, and Global Hawk, were designed to fulfill surveillance requirements at Close Range (50 km), Short Range (200 km) and Endurance Loitering (beyond 200 km) (fas.org).

As the payloads and capabilities evolve, so do the mission requirements. Time sensitive, mission critical targets, require decisive action for American troops to maintain an asymmetric advantage over the fluidity of today's dynamic battlefield. National or regional assets like Global Hawk or Predator are not a viable means of intelligence gathering in these situations because of their prolonged response time from notification to execution. Special Tactics Teams, Navy Seals, and Special Operating Forces need real-time ISR at small distances (1 km – 5 km) of small areas (caves or concealed defilades). To meet this demand, the Defense Advanced Research Projects Agency (DARPA) defined a new category of UAVs, Micro-Air-Vehicles (MAVs), to explore the military relevance for future military operations, and to develop and demonstrate flight-enabling technologies for very small aircraft. James McMichael, DARPA's MAV Program Manager uniquely described the MAV concept as:

> MAVs should be thought of as aerial robots, as six-degree-of-freedom machines whose mobility can deploy a useful micro payload to a remote or otherwise hazardous location where it may perform any of a variety of missions, including reconnaissance and surveillance, targeting, tagging and bio-chemical sensing. (McMichael and Francis, 1997)

Lt Jeff Mustin, in an article about the future development, tactics, and applications of UAVs, stated, "The necessity of real-time BDA is far too hazardous for manned assets but perfect for UAVs. The adventuresome undertaking of collecting SIGINT *sic [Signals Intelligence]* on surface-to-air missile (SAM) sites is also well suited for unmanned assets" (Mustin, 92).

The Air Force Research Lab, Munitions Directorate, Flight Vehicles Integration Branch (AFRL/MNAV) developed a carbon-fiber matrix MAV with a flexible,

rectangular reflexed wing, a 21″ span, and a 6″ chord called Combat-Camera (BATCAM), for Air Force Special Tactics Teams in Afghanistan. Torres and Mueller succinctly surmised the purpose of these man-portable MAVs as "answering the question: 'What's over the next hill'? (Torres and Mueller, 2001:116). BATCAM weighs 400 grams, can be folded and carried in a troop ruck-sack, and remotely piloted using a hand-held navigational device. AFRL/MNAV designed BATCAM and a number of variants without performing a thorough engineering analysis on the aerodynamic performance properties of the airfoil, control surfaces, or fully assembled aircraft before deployment to forward operating locations. Limited flight-tests were conducted to tailor the autopilot features and fine-tune camera operation. AFRL/MNAV requested AFIT perform an extensive wind tunnel engineering analysis of the aerodynamic performance characteristics on the first generation flexible wing MAV (tapered reflex wing, 24″ span, 6″ chord) and compare it to a geometrically identical rigid wing prototype. Their objective is to answer how the flexible wing structure affects the fundamental aerodynamic physics of the wing.

Scope of Experimental Effort

The primary objectives of this experimental study are to:

- Measure and compare the aerodynamic forces and moments on the flexible and rigid wing MAVs.
- Calculate the lift, drag, and side force coefficients, C_L, C_D, C_Y, on both MAVs at four different tunnel speeds: U_∞ = 10, 20, 30, & 50 mph.
- Calculate the pitch, roll, and yaw moment coefficients, C_m, C_ℓ, C_n, on both MAVs at 30 mph for four different yaw angles: ψ = 0°, 4°, 8°, & 12°.

- Calculate the stability derivatives, C_{m_α}, C_{ℓ_β}, C_{n_β}, for the flexible wing MAV where four yaw angles, $\psi = 0°, 4°, 8°, \& 12°$, are measured at each of four separate angles of attack, $\alpha = 0°, 2°, 4°, \& 6°$.

- Calculate the aerodynamic force and moment coefficients on both MAVs at 30 mph with various combinations of control surface (elevons) deflection settings.

- Calculate the thrust and power coefficients, C_T & C_P, at various motor RPM settings for the flexible wing MAV where three Angles of Attack, $\alpha = 0°, 4°, \& 8°$, are measured at each of three separate tunnel speeds: $U_\infty = 10, 20, \& 30$ mph.

The Air Force Institute of Technology (AFIT) installed a 3'x 3' low-speed, open circuit wind tunnel in early 2003. As with all wind tunnels, its characteristics needed to be defined and measurement systems calibrated to ensure data collected from it has a high degree of accuracy. The secondary objective of this experiment is to assess the tunnel flow quality and ensure consistent flow properties throughout the test section.

II. Literature Review

A new field of academic endeavor has emerged in the area of low Reynolds number, miniaturized UAVs. These Micro-Air-Vehicles (MAVs), as they are known, have a typical Reynolds number (Re_c) regime on order of 5.0×10^4 to 2.5×10^5 (Torres and Mueller, 2001:116; Mueller, 1999:1; Gad-el-Hak, 2001:419). Vast improvements in the field of miniaturized electronics have successfully reduced the weight and volume of sensing equipment such that a full complement of video, IR, chemical and biological detection, and signals emission detection equipment are all possible platform payloads for the new generation of MAVs (Mueller, 1999:2). This chapter reviews some of the contemporary work in the field of low Reynolds number aircraft design and its associated performance and difficulties.

Low Reynolds Number Design

MAVs operational uses are generally limited by three factors resulting from their unusually small construction (Kellogg and Bowman, 2004:1):

- Their size restricts their capabilities; robustness is incongruent with the goal of miniaturization.
- Size and weight constraints restrict the on-board power generation capacity, usually provided by battery packs, which severely limit mission duration.
- Compactness and portability motivate MAV designers, as such; their flight controls are incapable of mitigating the large crosswind gusts and updrafts generated by localized thermal variations. These disturbances reduce wing lift at moderate angles of attack -- both of which result in a catastrophic loss of the MAV.

Because their physical size and motor/propeller combinations are indeed small, MAVs have a small chord length and travel at low velocities in the range of 10 – 50 mph, resulting in flight Reynolds numbers much smaller than typical manned aircraft (Kellogg and Bowman, 2004:1; Torres and Mueller, 2001:116). The Reynolds number is the parameter of critical concern in the design of MAVs. The Reynolds number is the ratio of inertial forces to viscous forces- a function of the relative velocity, medium density, viscosity, and characteristic dimension.

The airfoil cross-section and wing planform present a vexing design conundrum for MAV engineers (Mueller, 1999:3). Portable, wispy, and undetectable are the milestones engineers use to benchmark cutting edge miniaturized flight vehicles, but aerodynamic efficiency, measured as the lift-to-drag ratio [$C_{L,\,max} / C_D$] becomes elusive as the Reynolds number decreases below 100,000 (Mueller, 1999:3). The choice of wing size and shape determine the operating Reynolds number, which in turn affects mission parameters such as payload capacity, loiter time, operational radius, climb rates, etc (Mueller, 1999:3). According to Michael Kellogg's XFOIL calculations and wind tunnel verification on several low Reynolds number airfoils ($Re_c = 6.0\times10^4$ to 1.5×10^5), an increase in operating Reynolds number, where both laminar and turbulent boundary layers influence the flow, increased the aerodynamic efficiency of the lifting surface under consideration (Kellogg and Bowman, 2004:5). Figure 1 illustrates the Reynolds number range for some common flight vehicles, including the operating region in this experiment (Jacob, 1998:4).

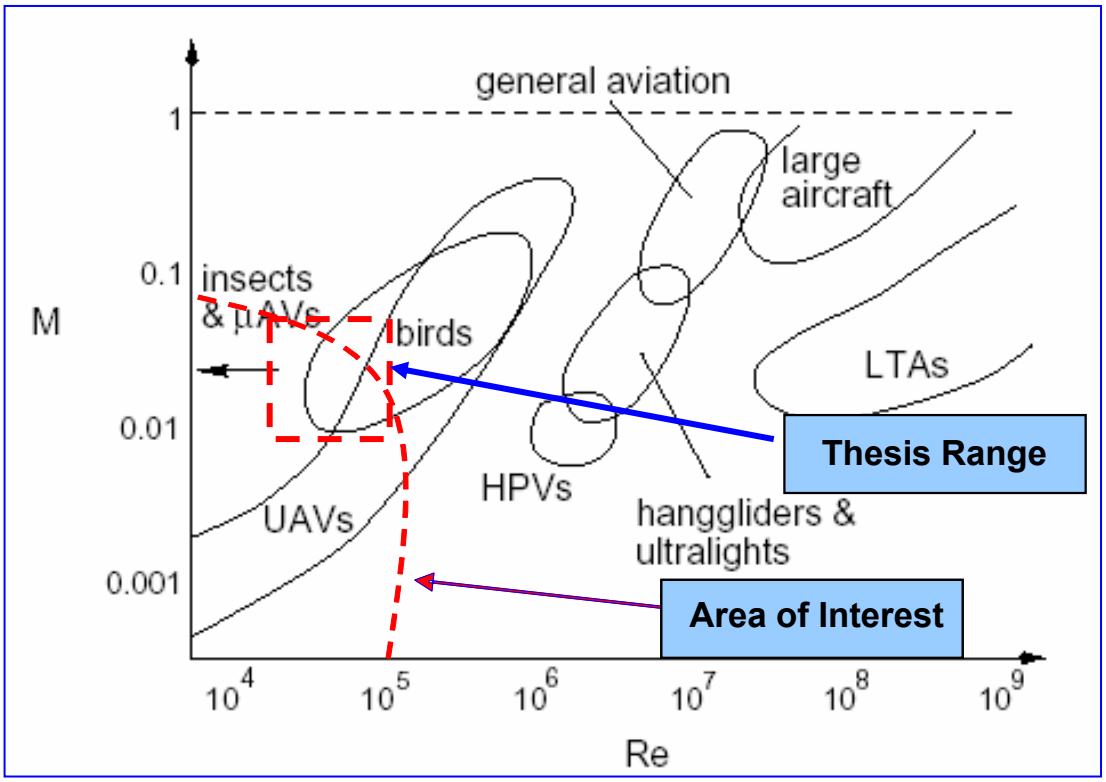

Figure 1. Mach number vs Chord Reynolds Number (Re_c) For Various Airfoils

According to Thomas Mueller, the design methods used over the past several decades maximize aerodynamic efficiency for aircraft with chord Reynolds numbers greater than 200,000, but are usually insufficient for vehicles operating at Reynolds numbers below that threshold (Mueller, 1999:4). The aerodynamics of these low Reynolds number aircraft present unique flow field interactions uncommon to larger aircraft.

Aerodynamic Considerations

The Reynolds number has a large effect on both the lift and drag forces generated over an airfoil. The low Reynolds numbers associated with autonomous MAVs render their lifting surfaces extremely susceptible to flow separation from leading to trailing

edge resulting in diminished capacity (Gad-el-Hak, 2000:419). This diminished capacity, the product of viscous effects, flow separation, and vortical structures on the wing tips combine to reduce the lift-to-drag ratio; and therefore, the efficiency (Gad-el-Hak, 2000:419). The Particle Image Velocimetry (PIV) image shown in Figure 2, taken from a conference paper by David Munday at the University of Kentucky, demonstrates the formation of a laminar separation bubble over an LNV109A airfoil stemming from flow separation at a Reynolds number of 2.5×10^4 and 0° angle of attack (Munday et al, 2002:2).

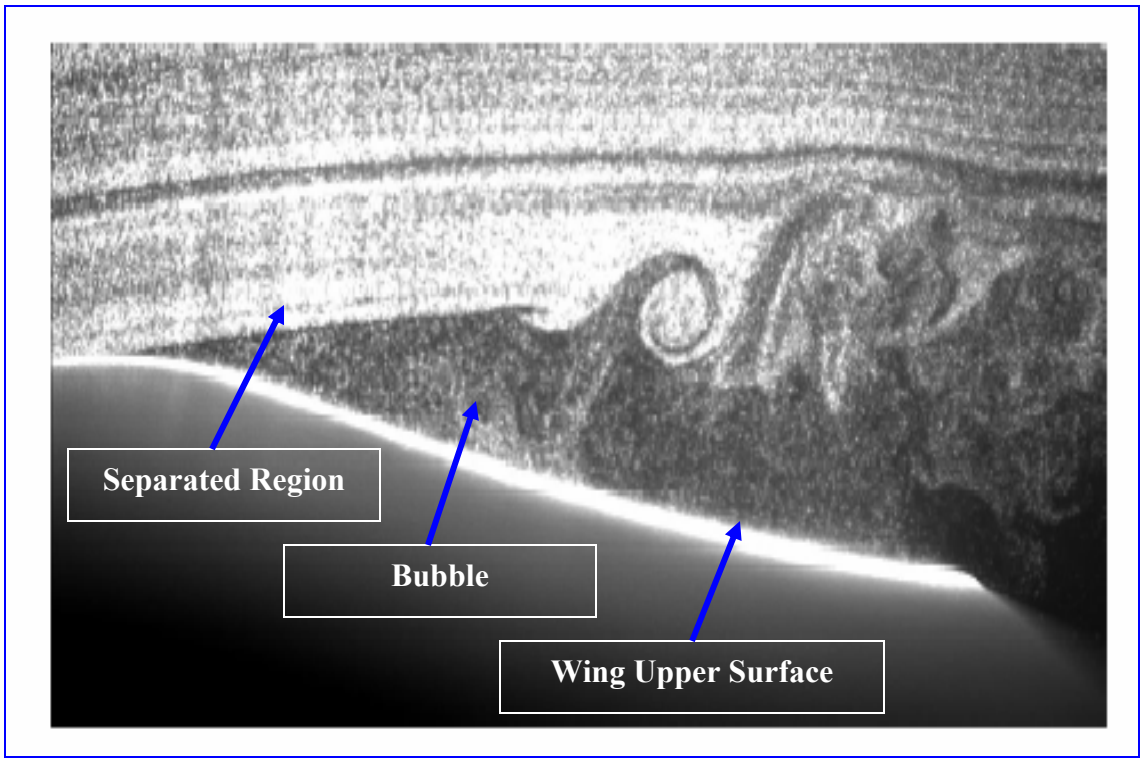

Figure 2. Laminar Separation Bubble at $Re_C = 2.5\times10^4$

The separation bubble shown above de-energizes the flow over the wing resulting in decreased lifting efficiency. In the Reynolds number range of $Re_c < 10^4$, the flow is completely laminar and can only maintain its streamlines in very small adverse pressure

gradients (Biber et al., 2004:7). In this range, aerodynamic efficiency is very low and viscous forces produce higher drag in the shear layer. These wings experience spontaneous separation of the laminar layer at the wing's leading edge leading to stall at small angels of attack (Mueller, 1999:4). Flow parameters also experience oscillations due to the presence of Von Karman vortex streets (Biber et al., 2004:1). The problems of dynamic fluid behavior are condensed at intermediate Reynolds numbers, $10^4 < Re_c < 5.0\times10^5$, the phenomenon of fluid separation, bubble propagation, transition to turbulence, and subsequent boundary layer reattachment all occur over very small lengths -- substantially altering performance (Gad-el-Hal, 2000:420). Transition to turbulence energizes the flow thereby enhancing momentum transfer and entraining fluid at the separation point, pulling the flow back towards the airfoil surface and creating the separation bubble (Gad-el-Hak, 2000:421). An order of magnitude higher in Reynolds number, $5.5\times10^5 < Re_c < 10^6$, presents more refined and well-behaved flow. However, the boundary layer thickens producing a thick wake and a thinner surface free-shear layer, which further reduces the lift-to-drag ratio (Biber et al., 2004:1). The optimal situation for MAV designers is to create a scenario where the size of the separation bubble decreases as the incident angle of attack increases through the stall angle, α_{stall}, at which point the flow enters a turbulent transition state near the trailing edge (Biber et al, 2004:7). The lift-to-drag ratio is lower for longer bubbles ($\approx$ 0.2-0.3*chord) because they alter the shape of the outer potential flow, significantly changing the pressure distribution; thereby, decreasing the lift slope (Gad-el-Hak, 2000:422). Figure 3 pictorially represents the phenomenon of a separation bubble forming on the top surface of an airfoil operating at a low Reynolds number (Gad-el-Hak, 2000:421).

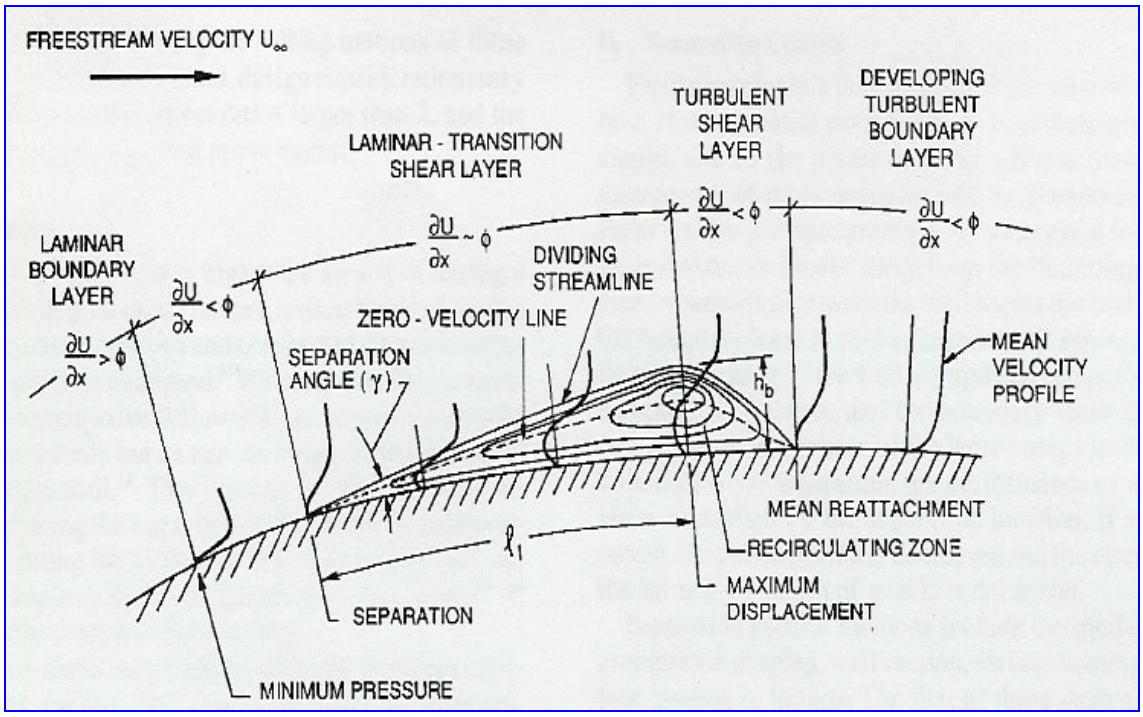

Figure 3. Development of a Laminar Separation Bubble Over a Wing

The flow over the planform of an aircraft with $Re_c > 10^6$ transitions to turbulent flow ahead of the laminar separation point (Gad-el-Hak, 2000:420). The increase in effective Reynolds number brings a corresponding decrease in the laminar boundary layer across a wing, which present both positive and negative benefits. Because laminar boundary layers have a lower velocity gradient at their surface they have lower skin friction drag than turbulent boundary layers. However, the downside of the lower drag associated with laminar boundary layers is a corresponding decrease in energy -- less energy leads to less inertia with which to negotiate surface irregularities and geometric discontinuities. According to viscous flow theory, the shear at the wall $\tau_w(x)$ decreases as the square- root of the axial dimension "x"; therefore, the drag force due to friction per uunit span is (White, 1986:397):

$$D(x) = b * \int_0^x \tau_w(x) * dx = 0.664 * b * \sqrt{\rho * \mu * x} * U\infty^{1.5} \quad \textbf{(1)}$$

The drag increases as the square root of the projected length (chord). The nondimensional drag coefficient due to skin friction, $C_{D(\text{Skin Friction})}$ is (White, 1986:397):

$$C_{D(\text{Skin Friction})} = \frac{2 * D(L)}{\rho * U\infty^2 * b * C} = \frac{1.328}{\sqrt{\text{Re}_c}} \quad \textbf{(2)}$$

Note, C_D is twice the value of the skin friction at the trailing edge -- or equivalent to the drag on *one* side of a flat plate. This result matches equations **(3)** & **(4)**, which give the contributions of skin friction drag over an entire wing for a given Reynolds number in both laminar and turbulent boundary layers (Barlow et al., 1999:303):

$$C_{D,LAMINAR} = \frac{2.656}{\sqrt{\text{Re}_c}} \quad \textbf{(5)}$$

$$C_{D,TURBULENT} = \frac{0.148}{\text{Re}_c^{0.2}} \quad \textbf{(6)}$$

The onset of turbulent flow is not necessarily a detriment to the MAV airfoil designer. Drag does not alter the airworthiness of a MAV; however, it does increase the thrust required to maintain straight and level flight. Resulting in higher engine output, increased battery consumption, and reduced mission endurance – detrimental to critical design objectives. Turbulent boundary layer growth may cause the skin friction drag to increase, but turbulence also delays boundary layer separation at large angles of attack.

Flow separation over a wing equates to the loss of lift due to the presence of adverse pressure gradients across the top of the wing where favorable pressure gradients previously resided. Adverse pressure gradients have a *positive* gradient such that the resulting pressure force is aligned in a direction that decelerates the flow. The mechanism, which specifically helps prevent flow separation, is the exchange of momentum from the freestream through the boundary layer (Tennekes and Lumley, 2001:2). According to Barlow, the value of C_D will continue to decrease with increasing Reynolds number in the laminar region until the minimum pressure point is reached (Barlow et al., 1999:305). Any further increase in Reynolds number will not move the transition point any further toward the wing's leading edge because it is already centered at the minimum pressure point for the particular airfoil. Increasing the operating Reynolds number, usually accomplished by higher velocities, trips the flow into turbulence and increases drag, again reducing the lift-to-drag ratio.

Flexible Wing MAVs

An innovative method to counteract the detrimental flow properties MAVs experience in the low Reynolds number regime is a wing structure that adapts to local flow conditions (Waszak and Jenkins: 2001:1). The University of Florida is the frontrunner in designing successful MAVs with root chord lengths 6″ and smaller. These MAVs have achieved critical success winning the ISSMO (International Society of Structural and Multidisciplinary Optimization) Micro Aerial Vehicle Competition three straight years (Waszak and Jenkins: 2001:1). The wings are constructed of a carbon fiber matrix leading edge with carbon fiber ribs attached orthogonally to the leading edge

supporting a parachute-latex membrane, which composes the planar surface of the wing. Adaptive washout is the principle designers use to characterize the effect these pliable aeroelastic wings achieve in flight. Sailboats use the adaptive washout technique to aid control of the sail through twist of the sail edge normal to the relative wind (Waszak and Jenkins: 2001:2). Adaptive washout contorts and twists the wing surface in response to localized disturbances, spontaneous changes in the attitude and speed, which change the angle of attack along the span. This ameliorates unsteadiness in the flight regime and insulates the MAV from flow field disturbances (Waszak and Jenkins: 2001:2). Figure 4, reproduced from a University of Florida briefing on MAV flight control, demonstrates the flexible response to a typical disturbance – wind gust (Nechyba and Ifju, 2002:11).

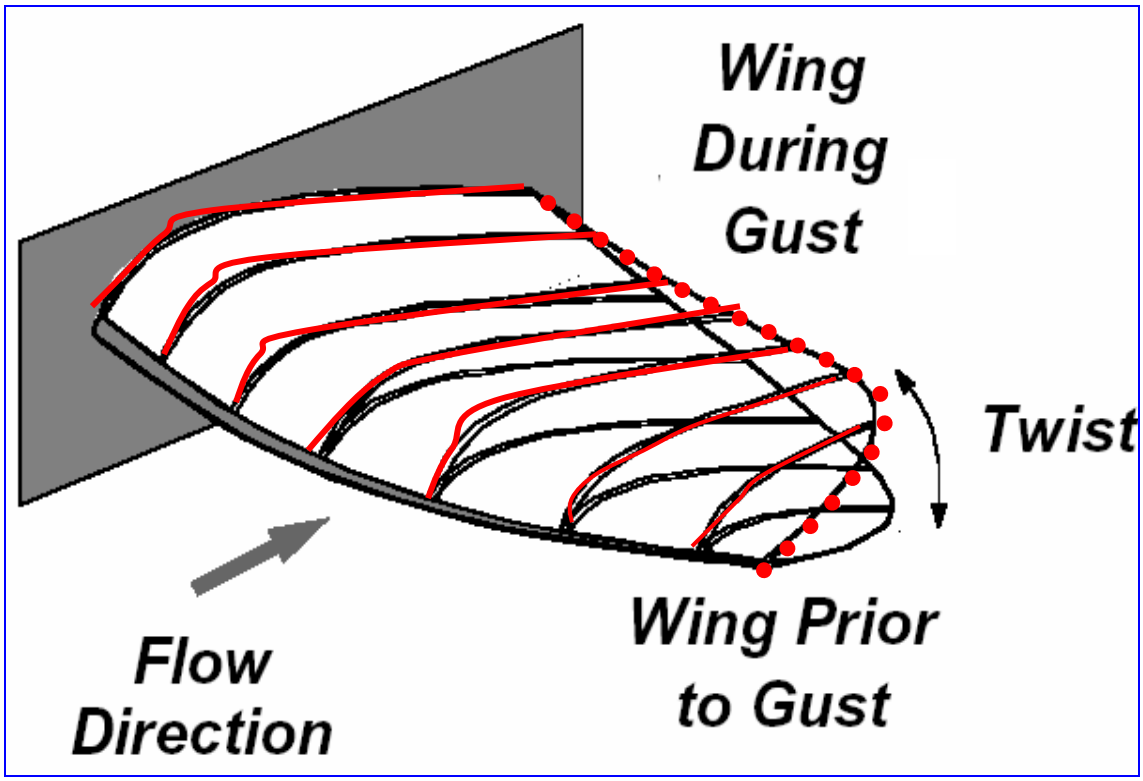

Figure 4. Flexible Wing Response to Localized Disturbance

The concept presupposes that biological aircraft (bats, insects, birds) can out-maneuver and outperform any manmade miniature flight vehicle (Nechyba and Ifju, 2002:10). Small flying organisms experience extremely low Reynolds numbers, but do not experience the same drastic aerodynamic difficulties small, manmade, rigid wing structures suffer. Wings found in nature typically have thin (less than 2% thick), slightly cambered, flexible wing structures that are extremely efficient (Nechyba and Ifju, 2002:10).

Kellogg and Bowman experimented with varying thickness airfoils in low Reynolds number tests and concluded thinner airfoils are, on average, 15% more efficient than thicker airfoils over the range $6.0\times10^4 < Re_c < 1.5\times10^5$ (Kellogg and Bowman, 2004:5). Moments of inertia are very small in MAVs constructed of epoxy, latex membrane, and carbon fiber. This physical characteristic severely limits the MAV's resistance to unsteady flow effects developed from atmospheric gusts or vehicle maneuvers (McMichael and Francis, 1997).

Two of the MAVs developed at the University of Florida are 1) a 6″ span, 3.3″ mean chord MAV used in the ISSMO competition and 2) a 24″ span, 6″ root chord MAV used for government research. Figure 5 is the 6″ span MAV (Nechyba and Ifju, 2002:3).

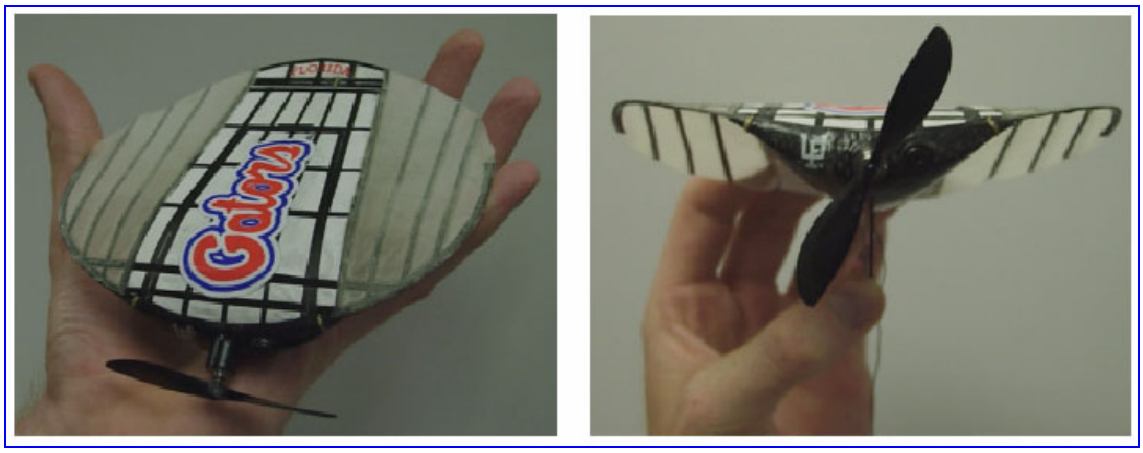

Figure 5. University of Florida's 6″ Span and 3.3″ Mean Chord MAV

Note the wing comprises nearly the entire structure of the vehicle. Figure 6 is the 24″ Span MAV (Nechyba and Ifju, 2002:3).

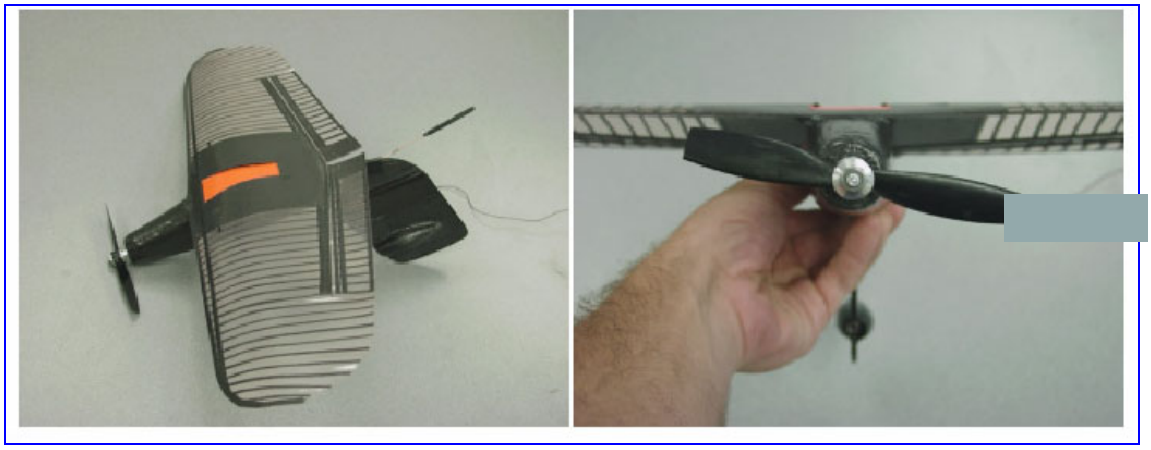

Figure 6. University of Florida's 24″ Span and 6″ Root Chord MAV

Vehicle Descriptions

The MAVs used in this experiment are similar to the University of Florida's 24″ Span and 6″ Root Chord MAV. AFRL/MNAV, in conjunction with the University of Florida, developed a separate MAV as the baseline for their combat camera MAV

program. The AFRL/MNAV MAV design has changed several times since this experiment -- the design has evolved from a 24″ span aircraft to an 11″ span aircraft, with a 21″ span aircraft called BATCAM currently deployed with Air Force Combat Controllers in Afghanistan. The vital characteristics of the MAVs used in this experiment are:

- Flex wing mass: 320 gr (0.705 lb_m); Rigid wing mass: 360 gr (0.794 lb_m)
- Carbon fiber matrix body, tapered rectangular shaped fuselage
- Thin, hollow boxed tail boom
- High mounted, tapered reflexed wing
- One wing is constructed of an approximate ¼ chord length carbon fiber leading edge with carbon fiber ribs spaced evenly from root-to-tip draped with a military parachute membrane material covering the planform area. The other wing is a solid rigid wing constructed entirely of carbon fiber.
- The control surfaces are elevons (combination of elevators and rudder) attached in a V-tail configuration at approximately 45° to the tail boom.

Table 1 and Table 2 summarize the salient geometric properties of the wing and tail surfaces.

Table 1. Wing Geometric Properties

Area	93.5 in^2
Root Chord	6″
Mean Aerodynamic Chord (c_{bar})	4.2″
Span	24″
Carbon Fiber Leading Edge Thickness	0.025″
Parachute Planform Thickness	0.005″
Aspect Ratio	6.16

Table 2. Tail Geometric Properties

Area	14.8 in^2
Chord	2.35″
Span	6.3″
Thickness	0.03″
Aspect Ratio	2.7

Figure 7 shows the two MAVs provided by AFRL/MNAV used in this experiment. The rigid wing MAV is on the lower left and the flexible wing MAV in on the upper right of the picture. Please refer to Appendix C for more pictures of the MAVs.

Figure 7. MAVs Provided by AFRL/MNAV used in this Experiment

III. Methodology

This chapter describes the equipment used in the hot-wire anemometry and the MAV wind tunnel experiments, followed by an explanation of the research methodology used to characterize the flow quality of the new AFIT 3' x 3' wind tunnel and the aerodynamic properties of the rigid and flexible wing MAVs.

Hot-Wire Anemometry

Equipment.

A motorized, fully automatic and programmable, 3-axis traversing system fixed with an x-wire measured flow quality in the tunnel. The measurement collection equipment was a Dantec-Dynamics Streamline 90N10 Constant Temperature Anemometer (CTA) X-Probe, with a $\pm 45^{o}$ wire sensor offset with respect to the probe orientation in the tunnel flow (probe is normal to flow). Figure 8 shows the probe orientation in the test section.

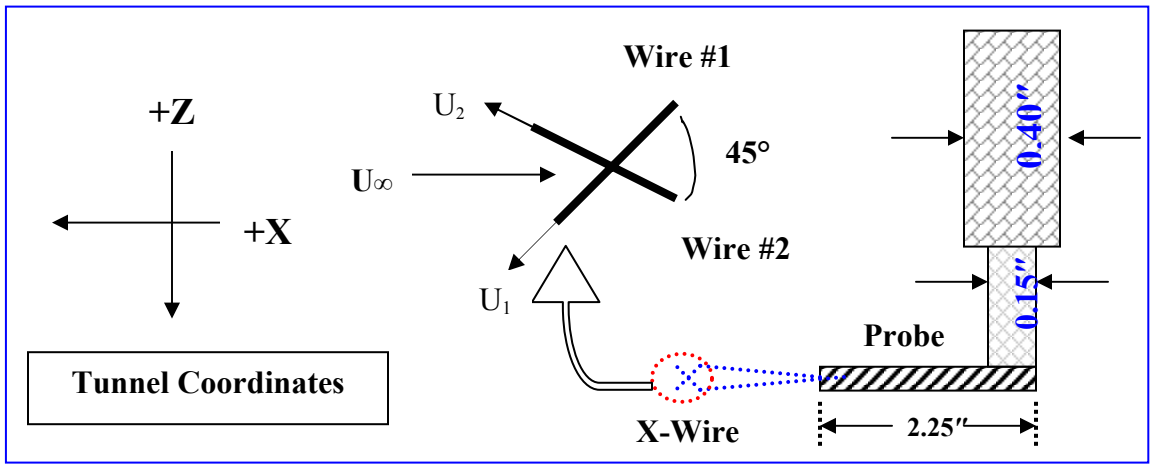

Figure 8. Orientation of X-probe in Flow

The angle between the U-velocity component and wire axis-1 is α_1 and the angle between the U-velocity component and the wire axis-2 is α_2. To convert the wire-fixed axis measured values of [(U_1, U_2) and (V_1, V_2)] velocities to the system reference axis system velocities, [U, V], the following equations were used (Subramanian: 31)

$$U = U_1 * \cos(\alpha_1) + U_2 * \cos(\alpha_2)$$
$$V = U_1 * \sin(\alpha_1) - U_2 * \sin(\alpha_2) \quad \textbf{(7)}$$

The measurement probe collects data on two channels at a frequency of 512 Hz each, for a combined data collection rate of 1.0 kHz. The probe has a maximum range of 500 mm in the horizontal and vertical directions (y & z-axis respectively) and the traversing mechanism has a maximum displacement in the longitudinal direction of 3 feet (x-axis). A commercial data acquisition software package developed by Dantec called Streamware®, was used for data collection, processing, and formatting. Once the probe signal is collected, the signal passes through a *gain amplifier conditioning* unit. This process conditions the response, boosts the intensity of the data signal, filters the signal with a low-pass filter to eliminate external noise and crossover interference, and finally converts the analog signal to a digital signal.

Table 3. Probe and Equipment Specifics

Probe Type	Sensor (wire) Resistance (R_{20})	Lead Resistance (R_L)	Total Probe Operating Resistance (R_{tot})
55 P61	3.5 Ohms	0.5 Ohms	$R=R_{tot}+\alpha_{20}R_{20}(T_{sensor}-T_o)$

Experimental Procedure.

Velocity measurements were collected along two orthogonal axes at various vertical and horizontal positions with respect to the tunnel axis system. The hot-wire system is located on top of the wind tunnel. A removable Plexiglas plate with slotted grooves allows the probe access to the test section. The plate has one slot oriented in the x-axis of the flow and six equally spaced slots oriented in the y-axis of the flow. Figure 9 shows the removable plate with the first slot open and the remaining five plugged.

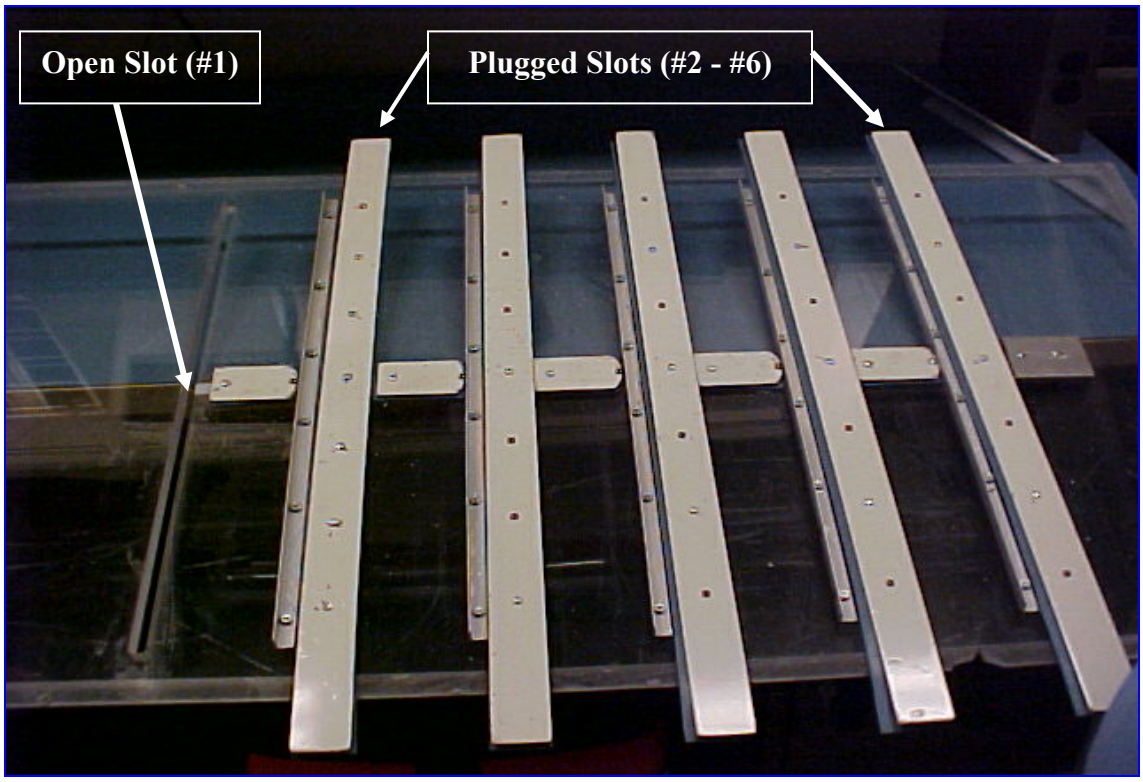

Figure 9. Removable Plexiglas Tunnel Top

To sample the flow quality of the complete test section, the probe was inserted through various slots and velocities were measured for several tunnel speeds in the test section. Table 4 details the various slot and velocity configurations tested.

Table 4. Hot-Wire Test Configurations

Slot Number	Distance From Front of Test Section	Tunnel Speeds Tested
1	2 ¼ ″	10, 30, 60, 90 mph
4	17 ¾ ″	10, 30, 60, 90 mph
6	27 ¾ ″	10, 30, 60, 90 mph

Three separate y-z planes at the four tunnel speeds indicated above were measured in the test section. The first plane was 2.25 ″ downstream of the start of the test section, the second plane is 15″ back from the first, and the third plane is 10″ back from the second. In each run, the probe is initially inserted 3.75″ into the test section through the Plexiglas plate and 12″ from the side of the test section walls. The probe descends in the +z-direction in 50 mm increments until it is 7.625″ from the bottom of the test section. At the bottom of maximum descent, the probe travels 50 mm in the –y-direction and begins to ascend in 50 mm increments in the –z-direction until it reaches its maximum height below the top surface of the plate and the process begins again until the entire measurement survey is completed. The entire grid is comprised of 121 velocity measurements taken in the y-z plane. Figure 10 illustrates a notional probe grid test pattern in the first plane.

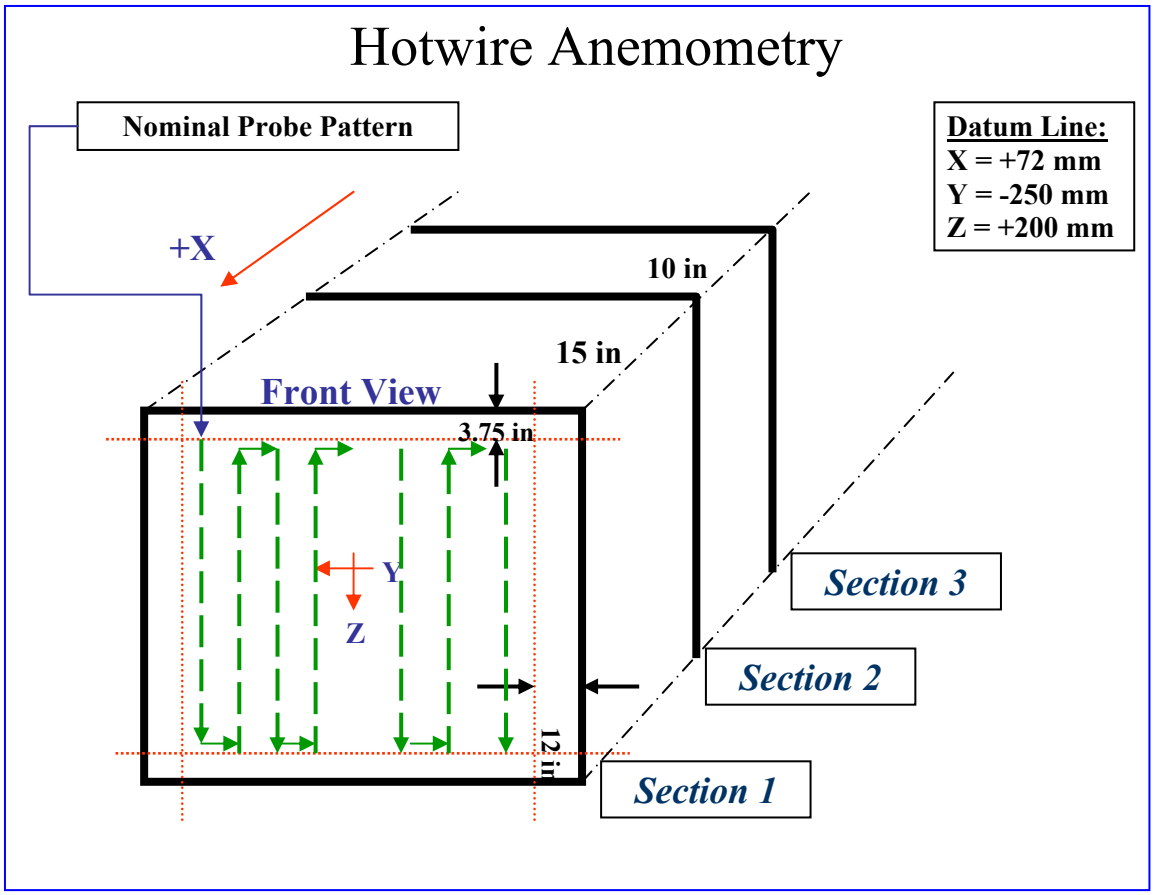

Figure 10. Nominal Probe Traversing Path

Data Analysis.

The Dantec Streamware® software stored the data files from each run as a Comma Separated File (.csv). Each file was manually assigned an index from 1-121 denoting the starting position of the probe through the finishing position of the probe. The Streamware® software automatically calculated the mean velocity at each data point. A Matlab® routine was written to read the *.csv* data file into an [11 x 11] matrix and create a contour plot of the mean velocities plotted against the vertical (z-axis) and horizontal (y-axis) probe motion during each test. This process was repeated four times for each tunnel speed in each of the three test planes.

MAV Wind Tunnel Test

Equipment.

The new AFIT 3'x3' wind tunnel was used for this experiment. New York Blower Company manufactured the tunnel and the ACF/PLR Class IV fan, Siemens manufactured the Adjustable Frequency Tunnel Controller, and Toshiba manufactured the Premium Efficiency (EQP III) fan motor. The basic specifications of the motor are as follows:

- 3 phase induction
- 200 Brake Horse Power
- Maximum theoretical speed is 150 mph
- Maximum tested speed is 148 mph
- 4 Poles
- 1785 RPM Operating Speed
- 230/460 Volts
- 60 Hz
- 444/222 Amps

The controller specifications are as follows:

- 460 Volts
- 315 Amps
- 250 max HP

The tunnel is an open circuit configuration with a closed test section. The flow follows a straight line from the entrance through the converging section to the test section through the diffuser and is then channeled 90^{o} toward the ceiling where it is exhausted. The fan is located at the end of the tunnel, sucking ambient air from the room through the test section. The opening is 122″w x 111″h x 70″d. Four, 20x20 steel mesh anti-turbulence screens and a ¼″ aluminum honeycomb flow-straightener, with a minimum aspect ratio

of 15, fills the front 70 inches of the opening, assuring well-defined laminar streamlines. Figure 11 shows a side view of the tunnel opening.

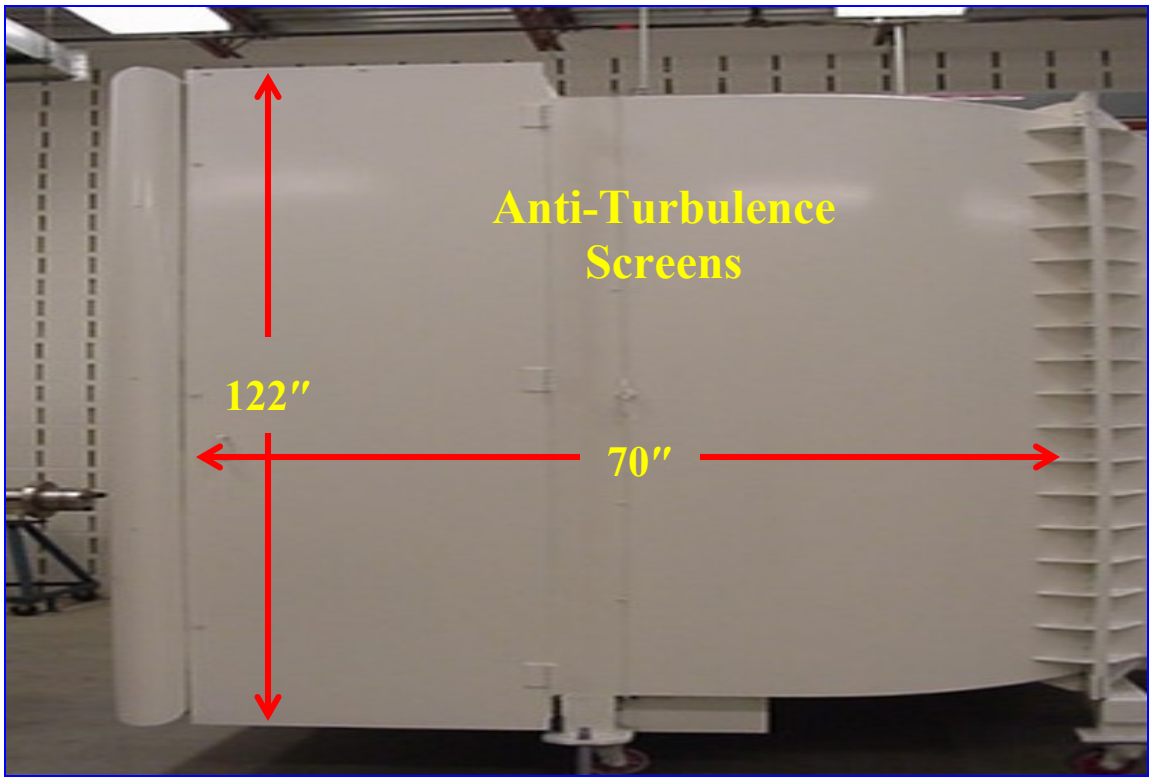

Figure 11. Side View of the Wind Tunnel Opening

The converging section has a contraction ratio of 9.5:1. The height of the tunnel after the last anti-turbulence screen is 111″ and the height just before the beginning of the test section is 31.5″. The length from the end of the last anti-turbulence screen to the beginning of the test section is 95.5″. Figure 12 shows the contracting section of the wind tunnel.

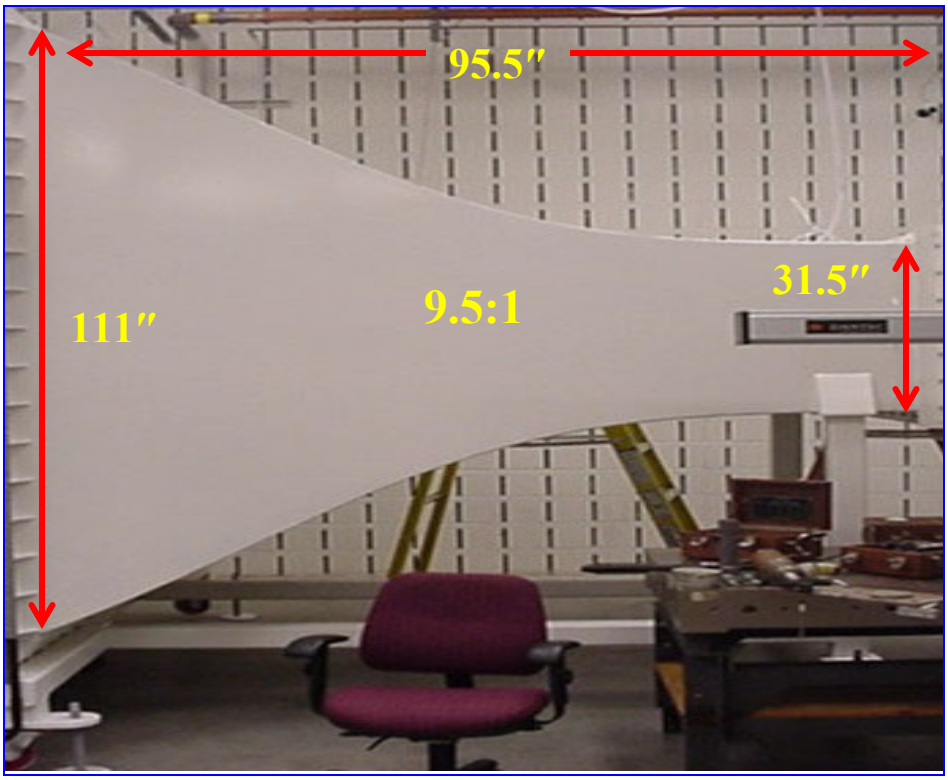

Figure 12. Wind Tunnel Converging Section

The test section is octagonal in shape with gas-actuated Plexiglas doors on both sides and a removable Plexiglas top panel. The Plexiglas doors enable easy access to the test article and internal balance, while the removable top Plexiglas panel can accommodate a hot-wire anemometry traversing system. The test section is 31″h x 44″w x 72″l. The MAV span-to-tunnel width ratio is: $\frac{b}{w} = \frac{24"}{44"} = .0545 \approx 0.55$, where the generally accepted rule of thumb is $\frac{b}{w} \leq 0.8$ (Barlow et al., 1999:28). See Figure 13 for a schematic of the tunnel.

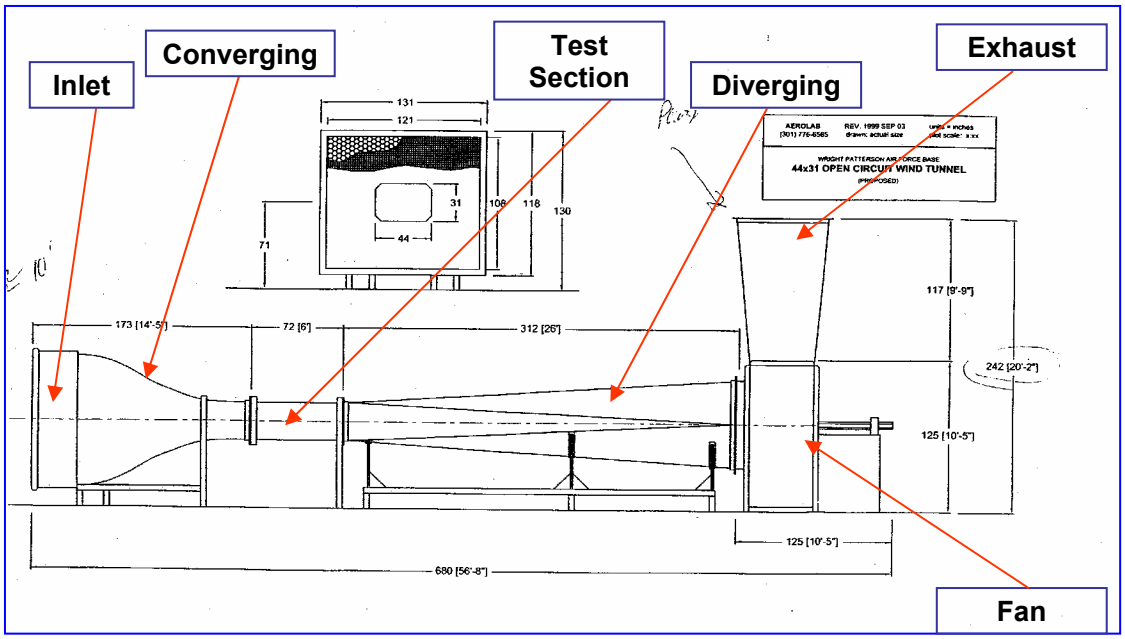

Figure 13. General Wind Tunnel Schematic

The measurement system is a remotely controlled automatic sting, which can accommodate a variety of six-component internal strain gauge balances. The sting enters the tunnel through a slot at the bottom of the test section. The sting can measure angles of attack (α) from -20^{o} to $+20^{o}$, and sideslip angles (β) from -15^{o} to $+15^{o}$. The force and moment data was collected with an Able Corporation, MKII 8-lb_f, six-component internal strain gauge balance. The balance is accurate to 0.25% of full capacity ($\approx$ 0.0125 lb_f). Table 5 lists the maximum loads on each of the MK II's six strain gauge rosettes.

Table 5. Maximum Sensor Loads

N_1 & N_2	8 lb_f
S_1 & S_2	5 lb_f
A_1	5 lb_f
ℓ_1	2 in-lb_f

The distance between the two normal force sensors, N_1 & N_2, is 2.10″, and the distance between the two side force sensors, S_1 & S_2, is 1.7″. The MK II balance is featured in Figure 14 below.

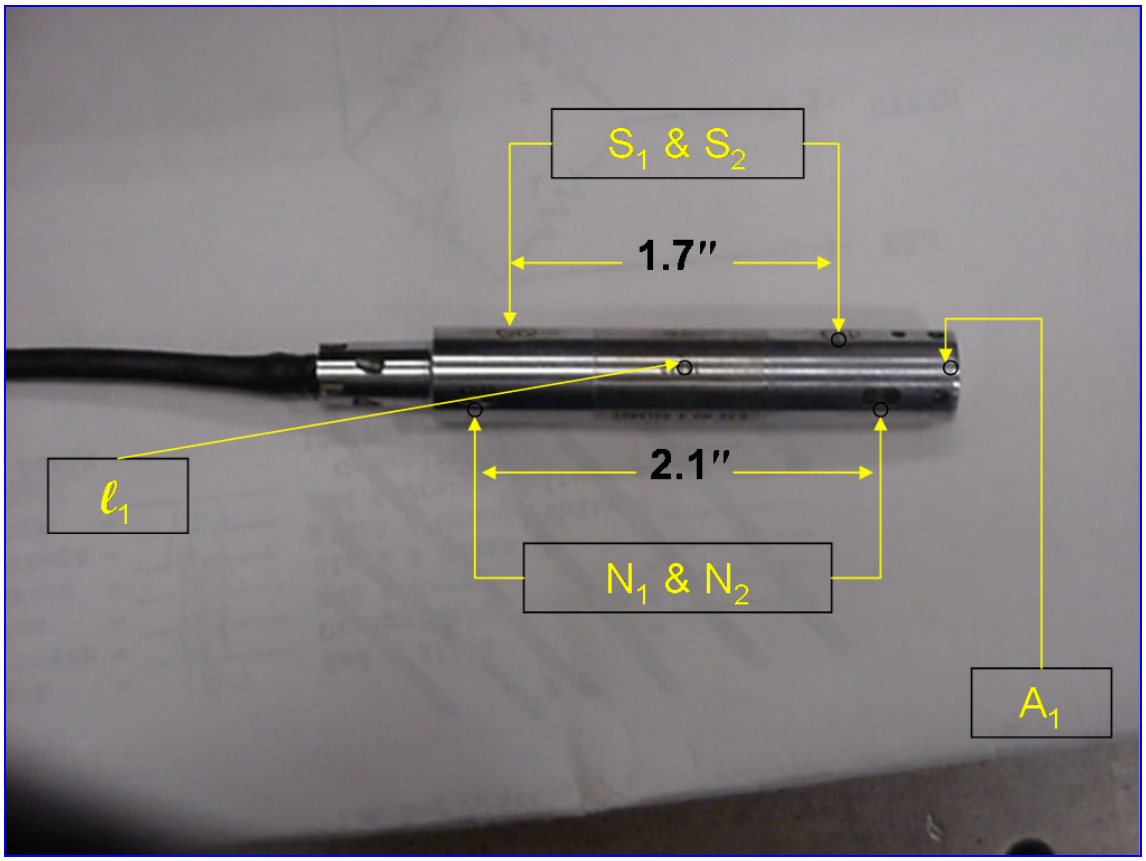

Figure 14. MKII 8 lb_f Balance

A 16-bit electronic data acquisition card and controller collected the balance force and moment data. The controller converts the strain gauge analog output to a digital signal, amplifies and conditions the signal with a low pass filter, and stores the data in a PC.

Experimental Procedure.

The tunnel technician, Mr. Dwight Gehring, calibrated the balance by attaching calibrated static weights to the balance and adjusting the calibration constants in the data collection software so the loads registered on the PC matched the weights attached to each sensor. Linearity in the balance was checked by applying weights to each sensor and ensuring the output voltage corresponded linearly to the increases in load. A roll angle offset between the MAV and the sting of 0.05^{o} was measured with a digital inclinometer. No roll angle offset corrections were applied because the MAV is mounted square on the balance and the roll is negligible. The tunnel speed, angle of attack, and yaw angles were controlled by a computer loaded LabView Virtual Instrument interface program and checked with analog feedback boxes. The analog feedback boxes use a pressure transducer and pitot-static tube to verify the tunnel speed, while the angle of attack and yaw angles were monitored with optical encoders mounted on the sting strut assembly.

The measured data from the balance is stored in the form of two normal force components (N_1 & N_2), two side force components (S_1 & S_2), an axial force component (A_1), and a roll moment (ℓ_1). Each sensor is a single axis, strain gage rosette. Voltage is continuously applied to the rosette and the resistance measured across a wire filament. When a load is applied, strain is produced in the wire causing an elongation in the wire

and a corresponding increase in the resistance. This change in resistance produces an output voltage, which is equated to strain and eventually to a force through a series of programmed calibration equations. See Appendix F for more detail on strain gauge operation. The coordinate axis system used in the tunnel is: +x is along the longitudinal axis (A_1) pointing toward the tunnel opening, +y is along the wing axis (S_1 & S_2) pointing toward the control room, and +z is perpendicular to the wings (N_1 & N_2) pointing toward the ground. Figure 15 illustrates the tunnel coordinate system, which is the convention used in wind tunnel model tests.

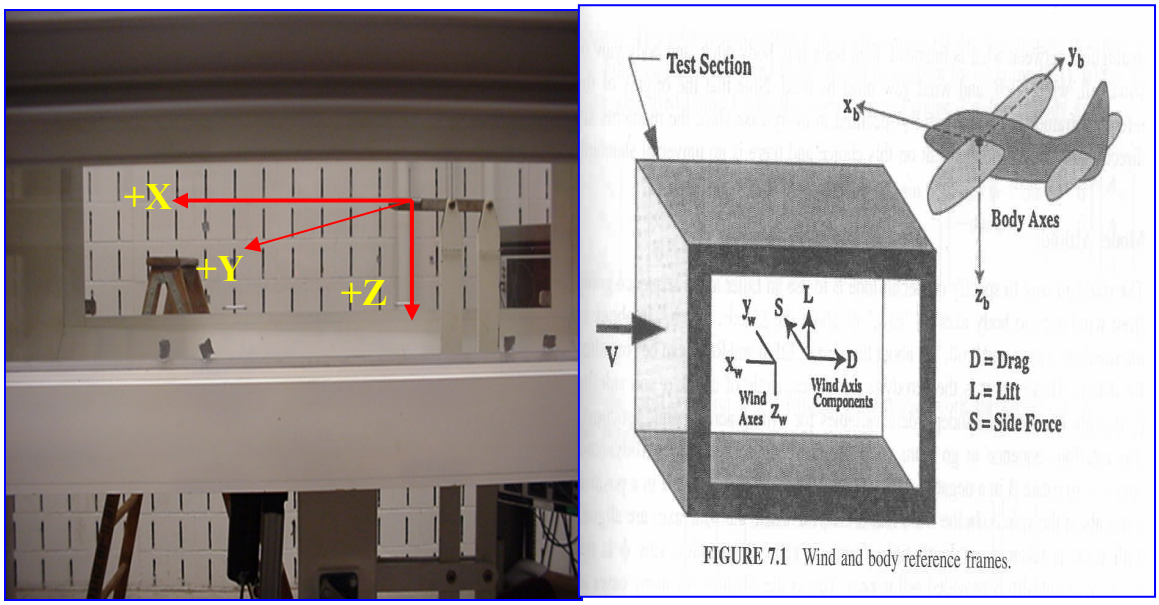

Figure 15. Positive Tunnel Coordinate System

The MAVs were attached to the sting/balance assembly with set-screws fixed to a polymer mounting block. The mounting block was drawn in AutoCAD and fabricated in AFIT's 3-D rapid prototyping machine. The polymer block was attached flush to the bottom of the MAV, beneath the battery compartment, to minimize center of gravity

(CG) displacement, and sealed with epoxy resin. Figure 16 shows the mounting block attached to the rigid wing MAV.

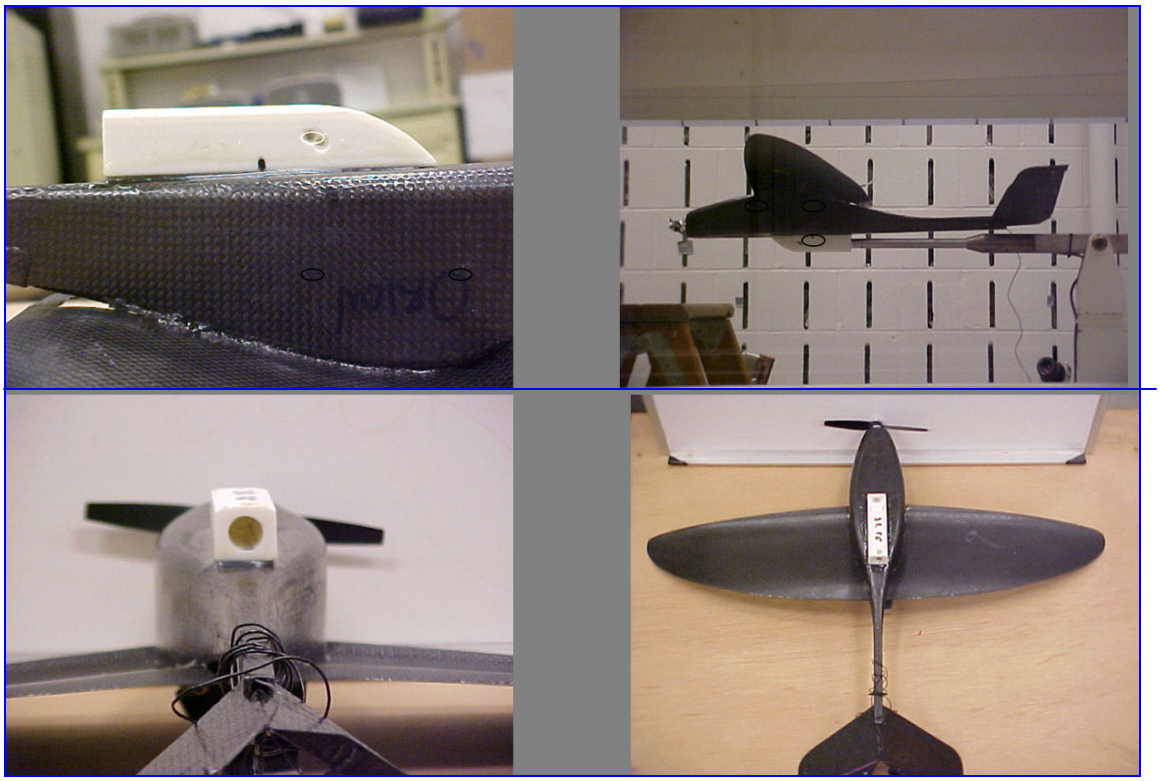

Figure 16. Polymer Mounting Block

Four categories of tests were conducted on each MAV (See Appendix D for Test Matrix):

- Alpha Sweeps (Propeller Removed)
- Beta offset Alpha Sweeps (Propeller Removed)
- Alpha offset Elevon Deflection Sweeps (Propeller Removed)
- Alpha offset Motor Power Sweeps (Propeller On)

Before each set of tests, data was collected on the MAV with no tunnel velocity. Determination of the effect of the MAVs static weight on the balance is necessary to remove the tare effects on the axial force sensor, which dramatically alters the drag coefficient. Data was collected at a sample of alpha and beta angles without the wind for this purpose.

For the alpha sweeps, the initial angle of attack was set to $\alpha = -4°$ for the flexible wing MAV and $\alpha = -10°$ for the rigid wing MAV. The velocity was increased until the desired test speed was reached followed by the start of each test. Data was collected for 20 seconds at each data point, defined by one increment increase in the angle of attack. The α angle was increased by +2°, except near the suspected stall angle (α_{stall}) where the increments were reduced to 0.5°, until $\alpha = +18°$. Table 6 lists the details for all of the alpha tests.

Table 6. Alpha Sweeps Test Matrix

β = 0°	**10 mph**	**20 mph**	**30 mph**	**50 mph**
Flex	-4°α to +18°α	-4°α to +18°α	-4°α to +18°α	-10°α to +8°α
Rigid	-10°α to +18°α	-10°α to +18°α	-10°α to +18°α	-7°α to +6°α

For the beta sweeps, the sting was rotated to the desired starting yaw angle, then declined to $\alpha = -4°$. The tunnel speed was set to $U_\infty = 30$ mph for each of the runs in the beta test sequence, then data was collected over a series of alpha angles, similar to the alpha sweeps test. Table 7 lists the details for all of the beta tests.

Table 7. Beta Sweeps Test Matrix

U∞ = 30 mph	**β = 0°**	**β = -4°**	**β = -8°**	**β = -12°**
Flex	-4°α to +18°α	-4°α to +18°α	-4°α to +18°α	-4°α to +18°α
Rigid	-10°α to +18°α	Not Tested	-10°α to +18°α	Not Tested

The elevon deflected runs were conducted at a tunnel speed of U_∞ = 30 mph and an angle of attack of $\alpha = 0°$ for each test. The elevon deflection angles were determined using a combination of the RC controller and a digital inclinometer. The elevons were set to 0° deflection with the trim tabs and then their angle measured with the inclinometer for each stick/trim change in the controller. Then a combination of controller stick clicks and trim offset changes were sampled until the desired elevon deflections were achieved. The precise combination of trim and elevon controller stick clicks were recorded for each of the test deflection angles. Table 8 lists the elevon settings used in the flexible wing tests. Three separate series of elevon deflection tests were conducted:

- Single elevon deflection ($\delta_{e,\,PORT} = 0°$ & $\delta_{e,\,STARBOARD}$ = Varied)
- Tandem elevon deflection ($\delta_{e,\,PORT} = \delta_{e,\,STARBOARD}$)
- Opposed elevon deflection ($\delta_{e,\,PORT} = -\delta_{e,\,STARBOARD}$)

Table 8. Flex Elevon Deflection Matrix

FLEX	$\delta_{e,\,PORT}$	$\delta_{e,\,STARBOARD}$
Single	0°	-20°
	0°	-10°
	0°	-5°
	0°	0°
	0°	+5°
	0°	+10°
	0°	+20°
Tandem	+10°	+10°
	+20°	+20°
	-10°	-10°
	-20°	-20°
Opposed	-10°	+10°
	-20°	+10°

Table 9 lists the elevon deflection settings used in the rigid wing tests.

Table 9. Rigid Elevon Deflection Matrix

RIGID	$\delta_{e,\ PORT}$	$\delta_{e,\ STARBOARD}$
Tandem	+10°	+10°
	-10°	-10°
Opposed	-10°	+10°

Each powered run was conducted at a specific angle of attack and tunnel speed, which did not change throughout the duration of the specified run. The throttle settings were determined similarly to the elevon deflection angles. The number of stick clicks were counted from the bottom to the top of the controller range. The number of clicks were divided by four to establish an approximate representation of ¼ throttle, ⅜ throttle, ½ throttle, and ⅝ throttle -- 6 clicks on the controller ≈ ¼ increase in throttle. Luminescent tape was affixed to one blade of the 4.75″ propeller. A General Radio Company_ *Strobotal* Strobe light was used to "*freeze*" the propeller indicating the approximate RPMs at each throttle setting. Table 10 specifies the tunnel speed, angle of attack, and RPM settings for each powered test.

Table 10. Powered Run Test Matrix

	U∞	α	Throttle	RPM
Test #1	10 mph	4°	¼	4300
			⅜	7500
			½	10,000
			⅝	12,400
			¾	13,200
Test #2	20 mph	0°	¼	5000
			½	8000
			⅝	10,000
Test #3	20 mph	4°	¼	5000
			⅜	8000
			½	10,400
Test #4	20 mph	8°	¼	4700
			⅜	7900
			½	10,300
Test #5	30 mph	0°	¼	6000
			⅜	8800
			½	10,600
Test #6	30 mph	4°	¼	6100
			⅜	8700
			½	10,600
Test #7	30 mph	8°	¼	6100
			⅜	8900
			½	10,500
			⅝	12,700

Data Analysis.

Data was collected for approximately 20 seconds per point. The data is stored directly into the control computer as a tab-delimited text file. Twenty seconds of data collection corresponds to approximately 30 lines of recorded tunnel data, which is $\frac{1.5\,\text{data points}}{\text{Second}}$ or a 1.5 Hz data-sampling rate. Microsoft Excel® was used to view and process the data files from each run. To process the data in preparation for reduction; spurious data, the data collected while the tunnel conditions were being initialized, and the transition data between test points were all deleted. Next, a single composite line of data representing [$U\infty$, α, β, N_1, N_2, S_1, S_2, A_1, $\boldsymbol{\ell}$] for each test point was calculated by averaging the 30 lines of data collected at each test point. Finally, the averaged test points for each run were copied to a text file and imported into MATLAB®. A MATLAB® program was written to reduce all of the test files, calculate all of the aerodynamic properties, and export the results in tabular format. The numeric results were imported to Excel and all of the aerodynamic properties were plotted according to standard aerodynamic practice.

The room temperature and pressure were recorded for each run and the ideal gas law was used to calculate the air density:

$$\rho = \frac{P}{R * T} \qquad \textbf{(8)}$$

The essential flight parameters were calculated next: the Reynolds number evaluated at the root chord, the dynamic pressure, and the Mach number were calculated for each wind speed. The Reynolds number is given by:

$$\mathrm{Re}_c = \frac{\rho * U\infty * C}{\mu}$$

Where:

ρ = The medium density

U_∞ = Tunnel Velocity

C = Root Chord Length

μ = Fluid Viscosity **(9)**

The dynamic pressure is given by:

$$q\infty = \frac{1}{2} * \rho * U\infty^2 \quad \textbf{(10)}$$

The Mach number is given by:

$$M = \frac{U\infty}{a} \quad \textbf{(11)}$$

a = speed of sound = $\sqrt{\gamma * \mathrm{R} * \mathrm{T}_{\mathrm{room}}}$

Next, the tare effects of the MAV's static weight were removed by fitting a 4th order polynomial in the form of :

$$y = ax^4 + bx^3 + cx^2 + dx + e$$

Where: **(12)**

x = tare alpha (independent variable)

y = individual sensor force (dependent variable)

to the tare data for each individual sensor [N_1, N_2, S_1, S_2, A_1, ℓ]. A matrix of polynomials was created from the six tare polynomials and the actual test alpha was substituted for the independent variable, "x", yielding the tare forces at the actual test alpha. The resulting test tare forces are used to calculate the unbiased sensor forces through the simple relation:

$$\mathrm{Forces}_{\mathrm{U}} = \mathrm{Forces}_{\mathrm{TEST}} - \mathrm{Forces}_{\mathrm{TARE}} \quad \textbf{(13)}$$

Once the tare effects are removed, the balance interactions must be removed. The sensors are not perfectly orthogonal; therefore, a component of force in each principal axis registers on the other "off-axis" sensors. For a perfectly centered balance with all sensors orthogonal, the readings on the five unloaded sensors should not theoretically register any voltage. Although designed to measure only directly applied loads, the close proximity of the rosettes to one another in the balance make it impossible to prevent some effect of loads from one sensor affecting another. Furthermore, any slight angle in the rosette will further exacerbate the effect one sensor has on another. These effects are captured in the manufacturer's balance interaction sheets. The balance manufacturer supplied a matrix of balance interactions resulting from applying 1 lb_f to each sensor and recording the output on the other five sensors. Each sensor was loaded twice with its maximum positive load and twice with its maximum negative load. Each sheet contains the registered voltage on the five unloaded sensors along with the particularly loaded sensor. A six-component balance has 27 interactions. This data is in volts; however, the balance output for [N_1, N_2, S_1, S_2, A_1, ℓ] is in lb_f. Therefore, the interaction data must be converted from volts to pounds-force. The voltage output for each loaded sensor was divided by its applied load to calculate the number of volts per 1 lb_f applied at each sensor. Next, the values in each sheet were divided by the applied load at that sensor. Finally, a row vector comprised of each sensor's $\frac{V}{1\,\mathrm{lb_f}}$ value was multiplied by each sheet. The balance interactions are removed from the unbiased forces through the equation (Barlow et al., 1999:261):

$$\left[\ F_{\text{Actual Load}}\ \right] = \left[K_{ij}\right]^{-1} * \left[F_{\text{Measured Load}}\right] \tag{14}$$

Where:
$\left[K_{ij}\right]$ = Matrix of Balance Interactions

Now, the tunnel corrections due to the MAV in the tunnel altering the flow dynamics have to be applied to the dynamic pressure and tunnel velocity. The first set of corrections are collectively called the *blockage correction*. The equations used to correct for the tunnel blockage are (Barlow et al., 1999:368-370):

$$\begin{aligned}
&\varepsilon_{Total} = \varepsilon_{sb} + \varepsilon_{wb} \\
&sb = \text{solid blockage} \\
&wb = \text{wake blockage (taken as negligible)} \\
&\varepsilon_{sb} = \varepsilon_{sb,wing} + \varepsilon_{sb,body} \\
&\varepsilon_{sb,wing} = \left(\frac{\kappa_1 \tau_1 * WingVolume}{C^{3/2}} \right) \\
&\tau_1 = \Im(\text{Test Section Shape} \,\&\, \frac{2b}{B}) = 0.83125 \\
&\kappa_1 = \text{body shape factor} = 0.9 \\
&\varepsilon_{sb,body} = \left(\frac{\kappa_3 \tau_1 * BodyVolume}{C^{3/2}} \right) \\
&\kappa_3 = 0.93
\end{aligned} \tag{15}$$

Next, the tunnel velocity and dynamic pressure have to be adjusted to account for alterations caused by the presence of the MAV in the tunnel (Barlow et al., 1999:414):

$$\begin{aligned}
q_{corrected} &= q_A (1 + \varepsilon_T)^2 \\
V_{corrected} &= V_A (1 + \varepsilon_T)
\end{aligned} \tag{16}$$

Once all of the tunnel corrections are calculated and the dynamic pressure and tunnel velocity are adjusted appropriately, the aerodynamic forces in the MAV body axis system are calculated from the corrected sensor forces. Once the loads were corrected to reflect the true loads at each sensor, the Axial, Side, and Normal forces, $[A \quad Y \quad N]$, were calculated from [N_1, N_2, S_1, S_2, A_1, ℓ]. The equations used to calculate $[A \quad Y \quad N]$ are (Barlow et al., 1999:237):

$$\begin{aligned} A &= A_1 \\ Y &= S_1 + S_2 \\ N &= N_1 + N_2 \end{aligned} \tag{17}$$

The equations used to calculate the Roll, Pitch and Yaw moments, $[\ell \quad m \quad n]$ are:

$$\begin{aligned} \ell_{body_{bc}} &= Sensor \\ m_{body_{bc}} &= N_1 * d_1 - N_2 * d_1 \\ n_{body_{bc}} &= S_1 * d_2 - S_2 * d_2 \end{aligned} \tag{18}$$

Where :
d_1 & d_2 = distances between sensors

$[A \quad Y \quad N]$ are forces measured with respect to the MAV's body axis and must be converted to the wind (earth) reference axis system. These forces in the wind axis are called Drag, Side Force, and Lift, $[D \quad S \quad L]$, and are the standard aeronautical engineering parameters used in the design and analysis of aircraft. The equations used to calculate $[D \quad S \quad L]$ in the wind axis system are (Barlow el al., 1999:237):

$$\begin{bmatrix} D \\ S \\ L \end{bmatrix} = \begin{bmatrix} A*\cos\theta*\cos\psi + Y*\sin\psi + N*\sin\theta*\cos\psi \\ -A*\sin\psi*\cos\theta + Y*\cos\psi - N*\sin\theta*\sin\psi \\ -A*\sin\theta + N*\cos\theta \end{bmatrix} \tag{19}$$

Similarly, the moments are also with respect to the MAV's body axis system and must be converted to a set of wind axes. The equations used to calculate $\begin{bmatrix} \ell & m & n \end{bmatrix}$ in the wind axis, centered at the balance/mounting block interface (bc), are (Barlow el al., 1999:238):

$$\begin{bmatrix} \ell \\ m \\ n \end{bmatrix}_{wind_{bc}} = \begin{bmatrix} \ell * \cos\theta\cos\psi - m * \sin\psi + n * \sin\theta\cos\psi \\ \ell * \sin\psi\cos\theta + m * \cos\psi + n * \sin\theta\sin\psi \\ -\ell * \sin\theta + n * \cos\theta \end{bmatrix}_{body_{bc}} \quad \textbf{(20)}$$

Lastly, the moments must be moved from the balance center reference frame to the MAV's body center located at the vehicle CG. The movement of the CG away from the balance center to the body center was calculated using a system of scales placed side-by-side with the MAV suspended in between by a long bar attached to the propeller shaft. The weight on each scale and the distance between each scale was recorded and a simple static analysis was applied to sum the moments about one end of the bar, solving for the only unknown in the equation, the CG distance. Figure 17 shows the basic methodology used to determine the location of the vehicle CG .

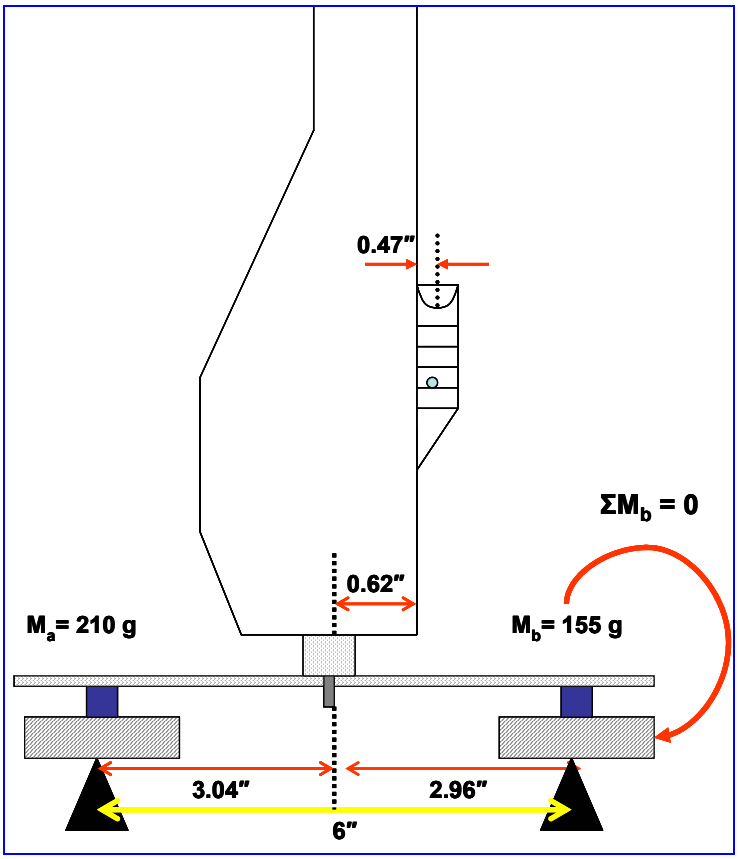

Figure 17. Sample Rigid Wing (Prop Off) CG Determination Drawing

The following equations illustrate how the final CG in the z-axis was calculated:

$$\begin{aligned} \sum M_b &= (210g * 6'') - (359.9g * Z_{CG}) = 0 \\ Z_{CG} &= 3.5'' - 2.96'' = 0.54'' \therefore \text{From Shaft Ctr} \\ Z_{\text{CG, MAV}} &= -(0.54'' + 0.47'' + 0.62'') = -1.63'' \end{aligned} \quad \textbf{(21)}$$

The CG was similarly calculated for both MAVs in the x & z-axes. The y-axis balance center and the vehicle CG were coincident.

Table 11 lists the distances from the balance center set-screw to the body center CG for the different MAV configurations.

Table 11. CG Locations from Balance Center for Propeller Off & On the MAV

	Flex Prop off	Flex Prop on	Rigid Prop off	Rigid Prop on
x_{cg}	1.95″	2.03 ″	1.78 ″	1.78 ″
y_{cg}	0.0 ″	0.0 ″	0.0 ″	0.0 ″
z_{cg}	-1.31 ″	-1.31 ″	-1.63 ″	-1.63 ″

With the CG locations determined and the moments calculated about the wind axis reference system, the following equations were used to transfer the moments to the body centered, wind axis frame (Barlow el al., 1999:238):

$$\begin{bmatrix} \ell \\ m \\ n \end{bmatrix}_{wind_{CG}} = \begin{bmatrix} \ell + S * z_{CG} + L * y_{CG} \\ m - L * x_{CG} + D * z_{CG} \\ n - D * y_{CG} - S * x_{CG} \end{bmatrix}_{wind_{bc}} \tag{22}$$

Now that the aerodynamic properties are calculated in the appropriate coordinate reference system, their presentation is more effectively conveyed as nondimensional parameter coefficients. The force and moment coefficients allow engineers to parametrically compare an assortment of otherwise dissimilar aircraft.

The forces and moments are nondimensionalized through the following equations:

$$\begin{bmatrix} C_D \\ C_Y \\ C_L \end{bmatrix} = \begin{bmatrix} D \\ S \\ L \end{bmatrix} * \left(q_C * WingArea\right)^{-1}$$
$$\begin{bmatrix} C_\ell \\ C_m \\ C_n \end{bmatrix} = \begin{bmatrix} \ell \\ m \\ n \end{bmatrix}_{wind_{CG}} * \left(q_c * WingArea * \bar{c}\right)^{-1} \tag{23}$$

Some texts, notably Nelson's *Aircraft Stability and Control*, use the wingspan to nondimensionalize the roll and yaw moments, but for consistency with the text used in this analysis, *Low Speed Wind Tunnel Testing*, the root chord was used for all three moments.

The angle of attack, drag coefficient, and pitching moment all require slight corrections due to test section geometry and flow field interference. The first set of corrections is applied to the geometric angle of attack. The indicated angle of attack in the control software changes under influence of the fluid streamlines being contained within the tunnel boundaries. According to Helmholtz's vortex theorem, in free flight, trailing vortices generated at the wing tips will extended indefinitely; however, in a closed tunnel, the walls become themselves a streamline of the flow where no fluid passes (Barlow et al., 1999:377). These added streamlines reduce both the induced drag and induced angle of attack for a specified lift condition. The induced drag corrections are (Barlow et al., 1999:416):

$$C_{D_{Corrected}} = C_{D_u} + \Delta C_{D_{up}} + \Delta C_{D_w}$$

$$\Delta C_{D_w} = \frac{\delta * S}{C}(C_{L_w})^2$$

Where:

C = Tunnel cross sectional area $= 31'' * 44''$

$\delta = \dfrac{\text{Model Span}\,(b)}{\text{Tunnel Width}\,(B)} = 0.1125$

C_{D_U} = Measured Drag

$\Delta C_{D_{UP}} = 0$

(24)

The angle of attack correction is (Barlow et al., 1999:416):

$$\alpha_c = \alpha_g + \Delta\alpha_{up} + \Delta\alpha_w$$
$$\Delta\alpha_w = \frac{\delta * S}{C}(57.3)C_{L_w}$$

Where: **(25)**

$\Delta\alpha_{UP} = 0$

α_g = Measured α

$\Delta\alpha_w$ = Change due to Walls

The final correction is the pitching moment correction. This involves a series of estimations about the wing and tail lift slopes; which were not independently tested, so pseudo approximations were assumed based on vehicle geometry and the lifting surface aspect ratios. The pitching moment correction procedure followed is (Barlow et al., 1999:399-400 and Nelson, 1998:48):

$$C_{m,CG_{Corrected}} = C_{m,CG_u} - \Delta C_{m,CG_t}$$

$$\Delta C_{m,CG_t} = \left(\frac{\partial C_{m,CG}}{\partial \delta_S}\right)\delta\tau_2\left(\frac{S}{C}\right)C_{L_W} \quad (57.3)$$

$$C_{m,CG_t} = -\left(\frac{S_t * l_t}{S_w * \bar{c}_w}\right)\left(\frac{q_t}{q_w}\right)C_{L_t} = -\overline{V} * \eta * C_{L_t} = -\overline{V} * \eta * C_{L\alpha_t} * \alpha_t$$

$$\left(\frac{\partial C_{m,CG}}{\partial \delta_S}\right)_t = -\overline{V} * \eta * C_{L\alpha_t}$$

$$C_{L\alpha_t} = \left(\frac{dC_L}{d\alpha}\right)_t \approx \left(\frac{0.1 * AR_w}{AR_t + 2.0}\right)(0.8) \qquad \& \qquad \left(\frac{q_t}{q_w}\right) \approx 1.0 \qquad \textbf{(26)}$$

Where:

$\overline{V}$ = Horizontal Tail Volume Ratio

$\bar{c}$ = Root Chord

$\overline{l_t}$ = Distance from CG to $\frac{1}{4}$ $M.A.C$ of the Tail

$\eta = \left(\frac{q_t}{q_w}\right) \approx 1.0$ = Ratio of Tail - to - Wing Dynamic Pressure

An analysis of the powered run data required a calculation of the thrust and power coefficients and an estimation of the vehicle's endurance capabilities, which is the reciprocal of the power number. The equations used to calculate the power coefficient, C_P, are (Barlow et al., 1999:509):

$$C_P = \frac{P}{\rho \eta^3 d^5} = \text{Power Coeffcient}$$

Where:

P = Prop Power = $(-\ell * \eta)$ - $(\ell * \eta)_{0\,\text{RPM}}$ **(27)**

ρ = density in $slugs/ft^3$

ℓ = Sensor Roll Moment $in - lb_f$

η = Prop Speed in Revolutions per Second

d = Prop diameter in $feet$

The propeller power is not directly measured. However, the definition of power is the product of torque and rotational speed. The torque developed with the *motor on* is nothing more than the reaction put forth by the set-screws connecting the mounting block to the balance, preventing the MAV from freely rotating about the x-axis. The rolling moment measured at *0 RPMs* (motor off condition) is subtracted from the power calculated at each RPM setting to remove the aerodynamic artifices present in the balance generated by the flow field and angle of attack. The equations used to calculate the thrust coefficient, C_T, are (Barlow et al., 1999:509):

$$C_T = \frac{T}{\rho \eta^2 d^4} = \text{Thrust Coefficient}$$
$$\text{Where:} \qquad \textbf{(28)}$$
$$T = \text{Thrust generated} = Axial\ Force - Axial\ Force_{0\,\text{RPM}}$$

The power coefficients are plotted against a nondimensional parameter called the advance ratio, J, which is: $J = \frac{V_c}{\eta * d}$ **(29)**

Various plots of the above parameters are presented as results in the next chapter.

IV. Results & Analysis

This chapter presents the data and results of the wind tunnel experiments performed on both the rigid and flexible wing MAVs. Unless specified otherwise, plots containing data for both the flexible and rigid wing vehicles will be delineated by solid lines for the flexible wing MAV and dashed lines for the rigid wing MAV. Table 12 summarizes the relevant flight parameters for the tunnel conditions tested. Refer to Appendix D for the data presented in tabular format.

Table 12. Summary of Flight Conditions

U_∞ (mph)	Mach #	q_c (lb_f / ft^2)	Re_c
10	0.013	0.25	4.5×10^4
20	0.025	0.90	8.55×10^4
30	0.038	2.16	1.32×10^5
50	0.065	6.15	2.23×10^5

Alpha Sweeps

The following plots characterize flexible and rigid MAV lift and drag coefficient performance versus change in angle of attack. Figure 18 depicts the lift and drag for both the flexible and rigid wing MAV over the entire range of tunnel speeds tested.

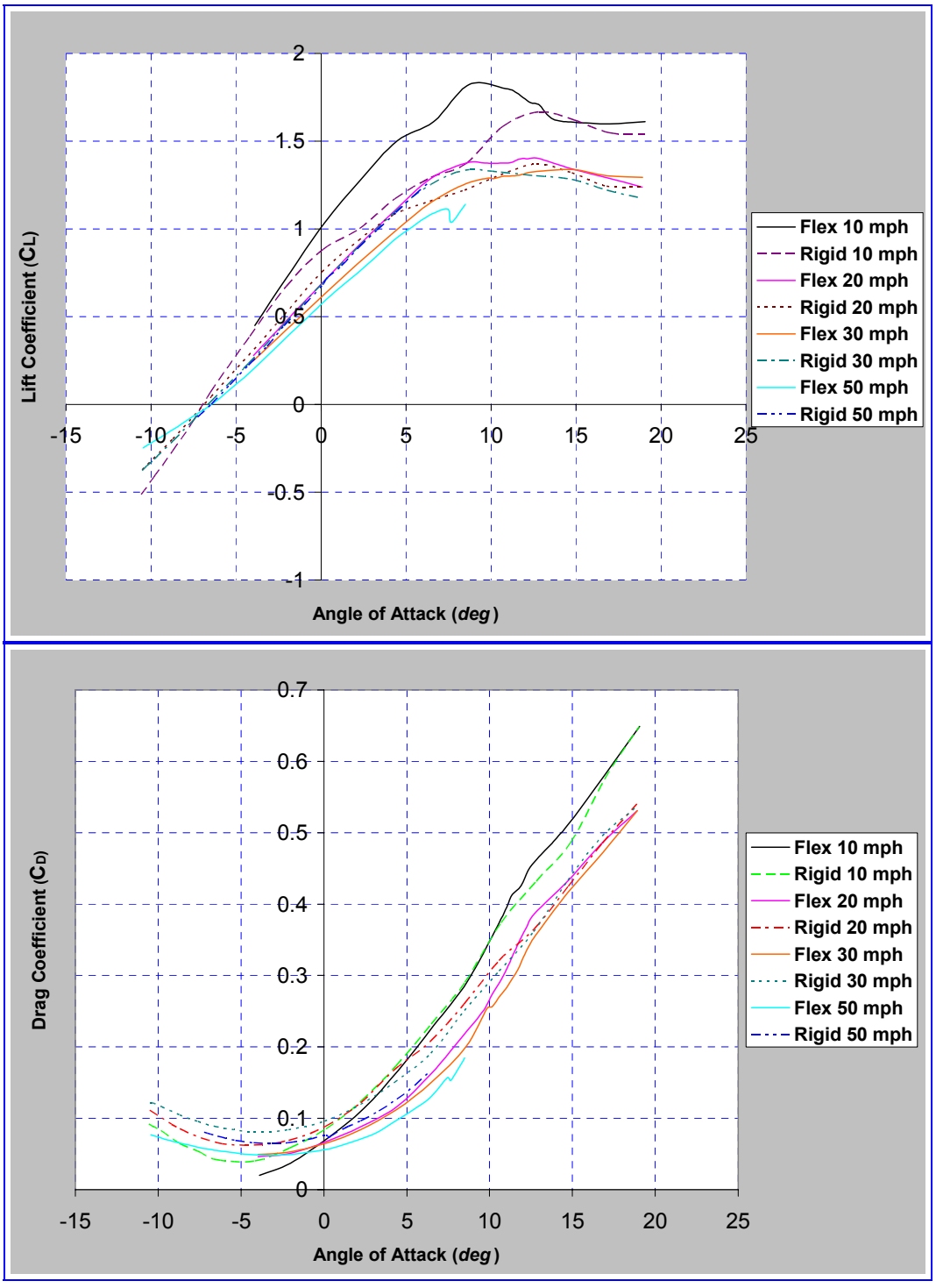

Figure 18. Flexible and Rigid Wing MAV C_L vs. α and C_D vs. α

This plot readily demonstrates that the rigid wing lift slopes are nearly coincident with a slight increase in slope attributed to Reynolds number effects eclipsing the laminar separation bubble as the flow moves through the transition region. The flexible wing lift slopes show considerable spread decreasing in slope due to the aeroelastic effects of the wing at higher Re_c. Near the zero lift line, $\alpha_{LO} \approx -6.5^{\circ}$, the rigid wing MAV exhibits higher drag at every airspeed than the flexible wing MAV. However, near the stall angle, α_{Stall}, the maximum drag values at each airspeed are nearly identical for the flexible and rigid wing MAVs. Further, the rate of drag increase is also very similar for both MAVs.

Figure 19 presents the flexible wing lift and drag curves with more detail. It is clear from Figure 19 that aeroelastic effects dominate the behavior of the lift slope over any Reynolds number effects in this vehicle as the tunnel speed increases. The drag data at 20, 30, & 50 mph are nearly coincident, while the 10 mph data is considerably higher. The two possible explanations for this occurrence are: 1) the forces at 10 mph are on order of the balance precision or 2) the laminar separation bubble in this Reynolds number regime cause a substantial increase in skin friction drag. Further investigation into the sources of error reveal the separation itself is not a consequence of error, but rather the aeroelastic deformation of the wings; however, the magnitude of the separation is due to balance error. See Appendix E for the error analysis. Furthermore, the laminar separation bubble manifests itself as the slight undulations seen in the 10 mph lift line, which represent the separation/reattachment of the boundary layer along the wing – causing degraded aerodynamic efficiency.

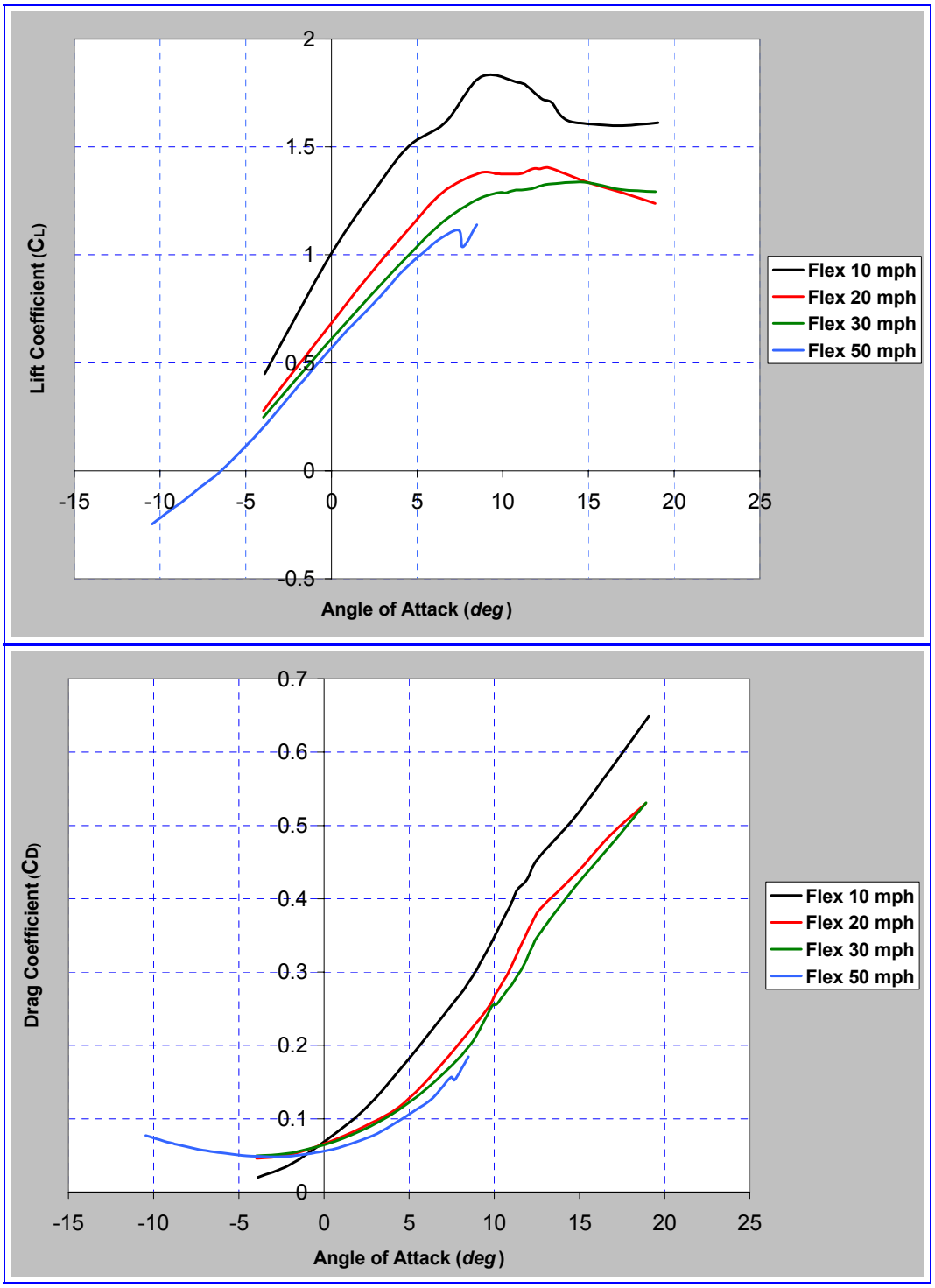

Figure 19. Flexible Wing MAV C_L vs. α and C_D vs. α

According to the laminar and turbulent skin friction drag equations on page 11 (equations 3 & 4) as the flow proceeds from strictly laminar to transitional, the drag increases by a factor of three as the Reynolds number increases. Therefore, the separation in the drag curves between the 10 mph data and the other three runs could strictly be attributable to the transitional machinations of undefinitized flow. Table 13 lists the $C_{D,\text{Skin Friction}}$ values for the Reynolds numbers tested.

Table 13. C_D (Skin Friction) for Laminar & Turbulent Boundary Layers

	10 mph	20 mph	30 mph	50 mph
	45,000	85,500	132,000	223,000
LAMINAR	0.0123	0.0091	0.0073	0.0056
TURBULENT	0.0173	0.0153	0.014	0.013
%Δ	*39%*	*68%*	*92%*	*124%*

Examination of the rigid wing lift and drag curves show that the wing's lift slope is independent of Re_c, in accordance with classical airfoil predictions. Similar to the flexible wing MAV, the presence of slight undulations in the 10 mph lift is a result of unsteady aerodynamics resulting from rapid separation/reattachment of the boundary layer at low Reynolds numbers. The drag is higher at 10 mph than in the other three runs and is mainly attributable to the fact the axial forces are on the order of the balance resolution. Figure 20 shows the rigid MAV curves.

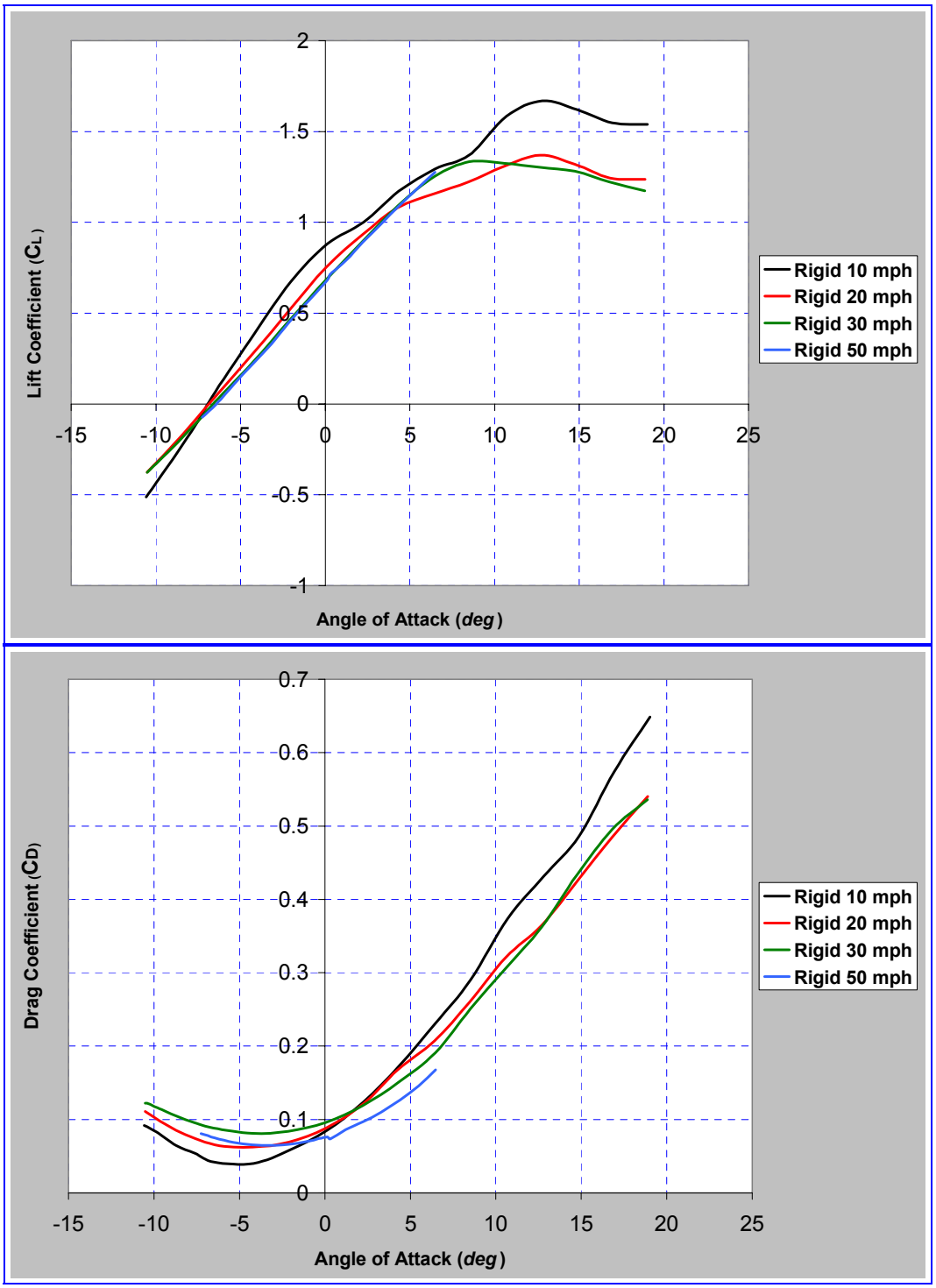

Figure 20. Rigid Wing MAV C_L vs. α and C_D vs. α

The next series of plots show C_L and C_D vs. α on the same plot for the flexible and rigid MAV at individual tunnel speeds. Figure 21 show the lift and drag coefficients vs. angle of attack for 10 and 20 mph respectively.

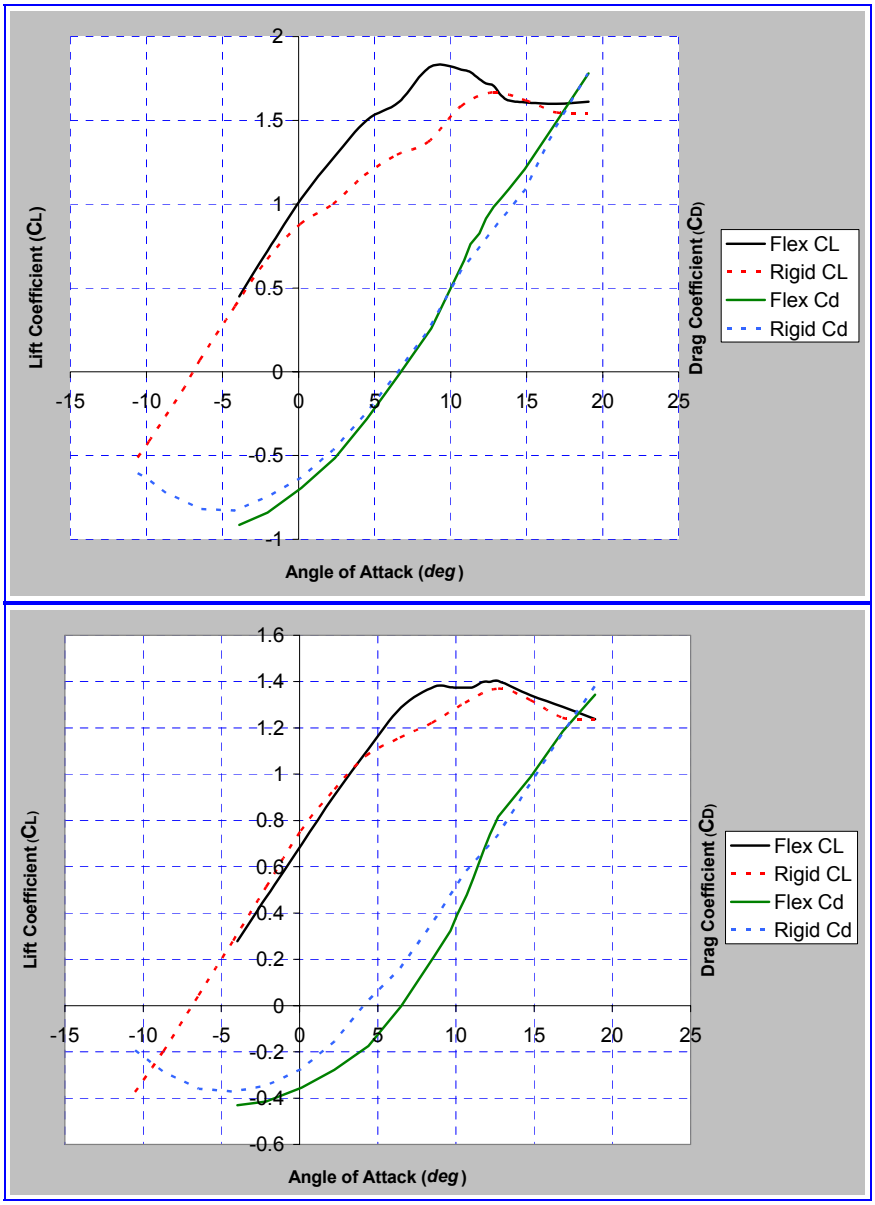

Figure 21. Lift and Drag at 10 & 20 mph

Figure 22 shows the same data for 30 and 50 mph respectively.

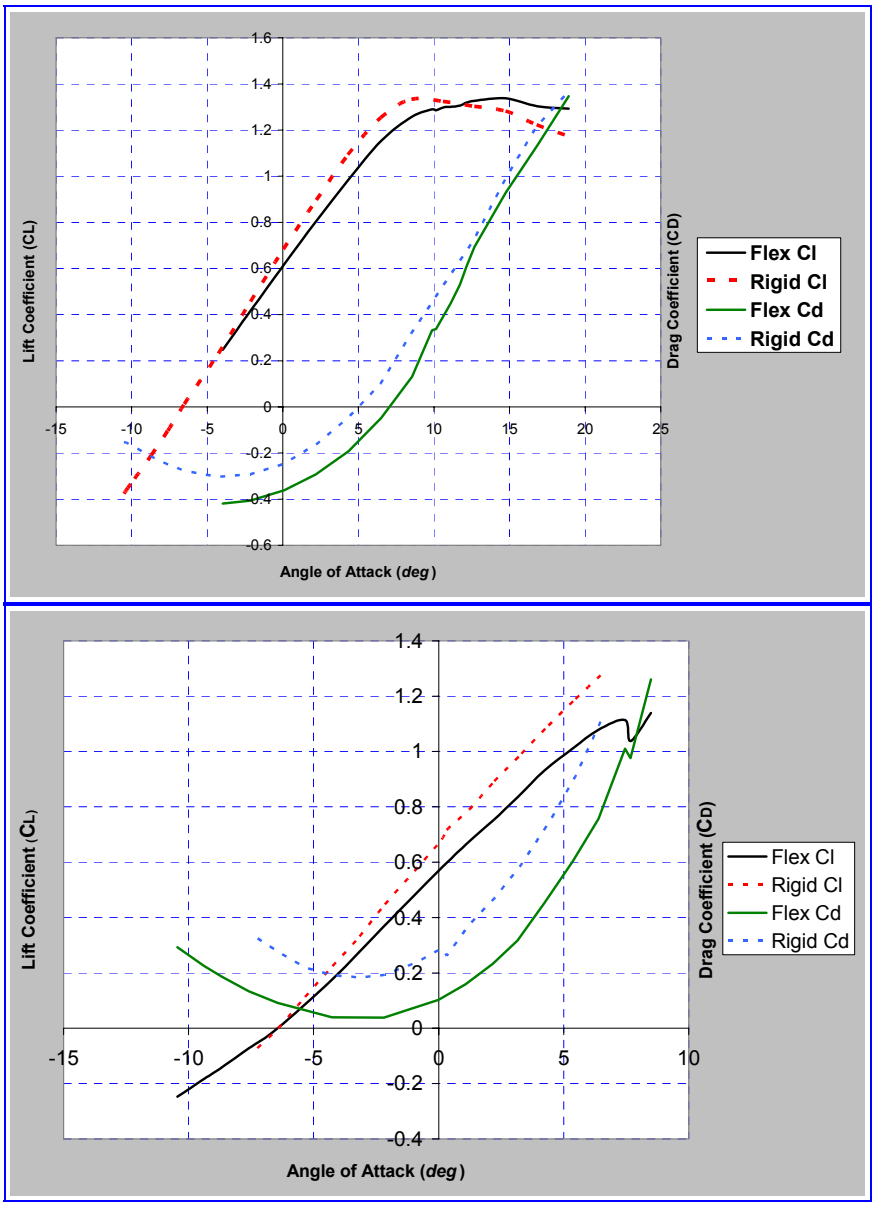

Figure 22. Lift and Drag at 30 & 50 mph

It is clear that at lower speeds, and therefore, lower Re_c, the flexible wing MAV has a steeper lift slope, and as Re_C increased, aeroelastic effects on the flexible wing MAV caused the lift slope to decrease. The prevailing velocity and Reynolds number for this transition appear to be 30 mph and 1.32×10^5, respectively. Another noteworthy trend is the separation in drag values between the flexible and rigid wing MAV increase with

increasing Re_C. Traditionally, as seen in the rigid wing MAV, as the velocity and Reynolds number increase, so does the drag; however, the flexible wing MAV appears to provide some resiliency against this increase in drag.

The 50 mph data is incomplete for both MAVs. At $\alpha = 7.5°$, the load on the N_1 sensor on the rigid wing MAV approached the 8 lb_f limit. At $6° \leq \alpha \leq 7°$, the wings on the flexible wing MAV started to bend excessively about the root chord to the point the tips nearly clapped together. After the flexible wing 50 mph test, the wings delaminated at the root and required repair. Fortunately, this was the last test run on the flexible wing MAV. Figure 23 shows the flexible wing before and after the 50 mph run.

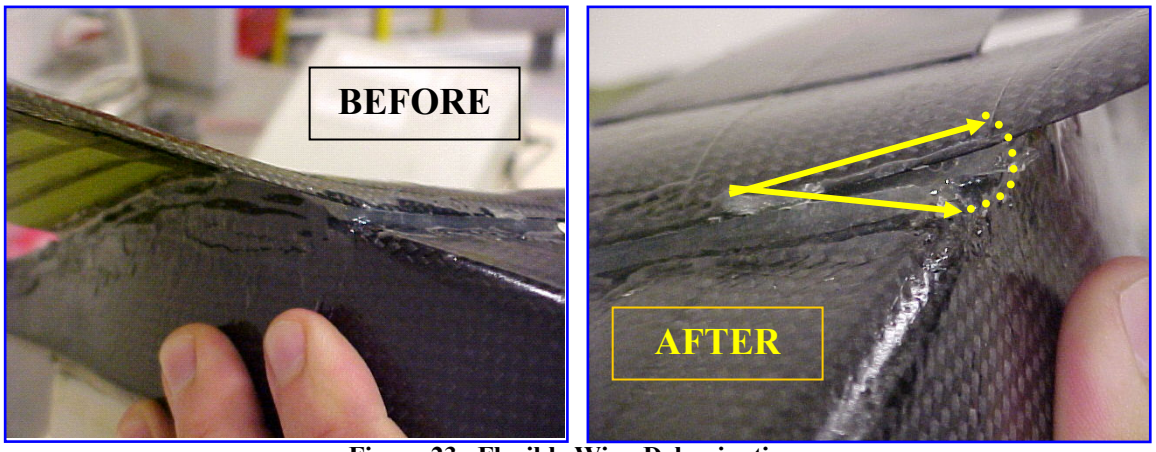

Figure 23. Flexible Wing Delamination

Table 14 summarizes the salient characteristics of the alpha sweeps tests. Both MAVs show a decrease in $C_{L,\,max}$ with increasing Re_c; however, the flexible MAV experienced a faster rate of decrease in $C_{L,\,max}$ than did the rigid wing MAV. Another important trend is in the change of the stall angle for each MAV. As expected, the rigid wing MAV's stall angle decreased with increasing Re_c, while the flexible wing MAV

showed the opposite trend, an increase in α_{stall} with increasing Re_c. Aeroelastic wing deformation is the primary factor corresponding to the delay in α_{stall}. The wing deforms under load from the ¼ M.A.C to the trailing edge. The trailing edge is deflected upwards, causing a net decrease in the wing incidence angle, resulting in a lower relative angle of attack.

Table 14. Summary of Maximum Lift and Stall Angles

	10 mph		20 mph		30 mph		50 mph	
	$C_{L,max}$	α_{stall}	$C_{L,max}$	α_{stall}	$C_{L,max}$	α_{stall}	$C_{L,max}$	α_{stall}
Flex	1.82	8.7°	1.40	12.7°	1.34	14.8°	1.11	7.5°
Rigid	1.67	12.8°	1.37	12.7°	1.33	8.5°	1.23	--
%Δ	***-8.2%***	***47.1%***	***-2.2%***	***0.0%***	***-0.7%***	***-39%***	***10.8%***	***--***

A plot of Lift over Drag (L/D) versus angle of attack is useful to illustrate the development of a vehicle's most efficient operating range. Figure 24 shows the L/D vs. α plot for both the flexible and rigid wing MAV. The rigid wing MAV's max L/D point decreased as the velocity increased except for the 50 mph data. Where the flexible wing MAV demonstrated relatively consistent L/D behavior at 20, 30, & 50 mph, again the 10 mph run shows either extreme laminar separation bubble consequences or the forces generated at that speed are on the order of the balance resolution and therefore were

removed from this plot. See Appendix E for the error analysis conducted on the 10 mph data as well as error bar plots of the 10 mph data against the 30 mph data for comparison of the error propagation when operating near the balance limits. The rigid wing max L/D point occurs at -5° < α < 0°, while the flex wing max L/D point moves to the right in the region of 0° < α < 4°. Comparing the more reliable 20 and 30 mph data, the flexible MAV has a maximum L/D of 10, while the rigid MAV had a value between 7 and 8.

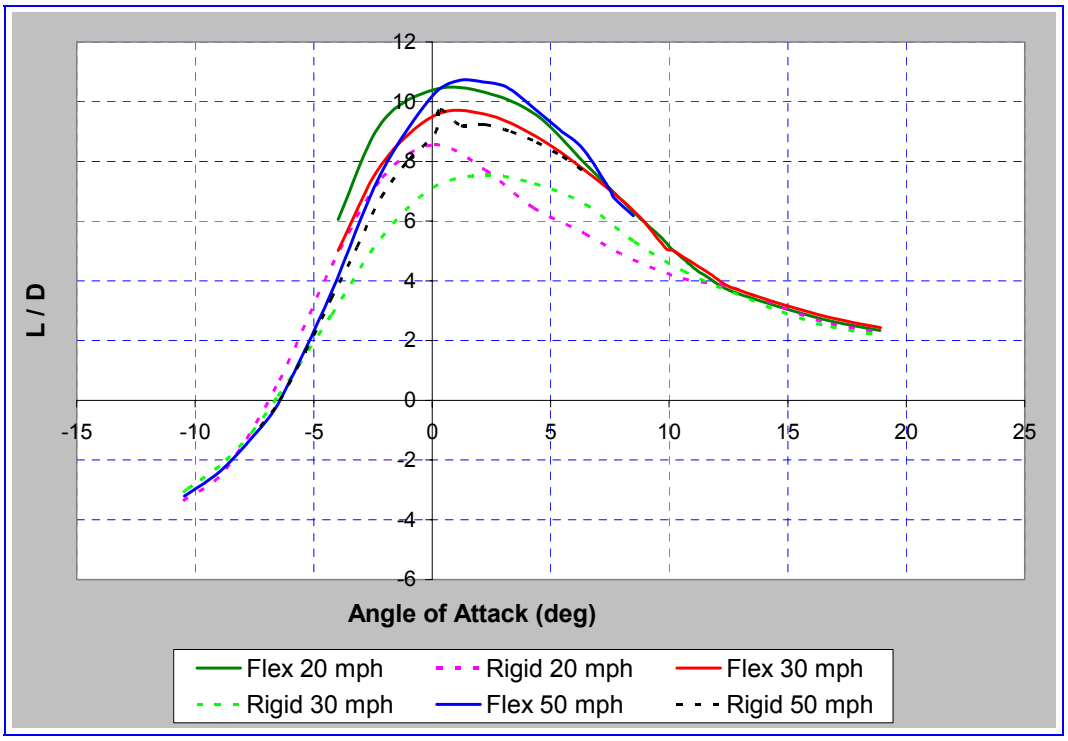

Figure 24. Flexible and Rigid Wing L/D vs. α

Lastly, a comparison of the experimentally generated lift curve slope (m) to the theoretical slope (m_o) is instructive to verify the change in lift as a function of angle of attack. The lift curve slope is given by:

$$m = \frac{m_o}{1 + \frac{m_o}{\pi * AR}} \tag{30}$$

A sample calculation of the experimental lift curve slope in Figure 18, for the flexible wing MAV at U∞ = 30 mph is (Keuthe and Chow, 1998:179):

$$m = \frac{\Delta C_L}{\Delta \alpha} = \frac{(1.1537 - 0.6189)}{\left(6.5098° - 0.099515°\right) * \frac{\pi}{180°}} = 4.78 \tag{31}$$

The lift curve slope for the theoretical elliptical circulation distribution is:

$$\frac{2 * \pi}{1 + \frac{\pi}{\pi * 6.16}} = 4.743 \tag{32}$$

Table 15 summarizes the lift curve slopes for both the flexible and rigid wing MAVs.

Table 15. Flex and Rigid Lift Slopes Compared to Elliptical Lift Distribution

	10 mph	20 mph	30 mph	50 mph	*Average*	%Δ RHS
Flex	5.317	5.338	4.77	4.19	*4.907*	**3.45%**
Rigid	3.709	4.44	5.075	5.354	*4.645*	**2.06%**

The difference between the experimental and predicted lift curve slopes is less than 5%. The slope of the C_L vs. α curve in Figure 18 is nearly identical to the predicted value. The flexible wing shows a slightly greater departure from the predicted value, likely a

factor of the wing's aeroelastic deformation under load. Equation 25 assumes a solid wing structure.

Beta Sweeps

The change in side force coefficient (C_Y) versus angle of attack for specific yaw angles is plotted for both MAVs. For reference system consistency, the yaw angle (ψ) is equal in magnitude but opposite in sign to the sideslip angle (β): $\psi = -\beta$. The flexible wing MAV's side force shows consistent growth with increasing yaw angle. The side force coefficient increases to a maximum at $\alpha = +5°$ for each β angle, then decreases rapidly. If the test angle of attack increased much past +20°, then all values of C_Y would become negative. The rigid wing values of C_Y also increase with increasing yaw angle. However, C_Y does not increase to a maximum value at $\alpha = +5°$ for each β angle like the flexible wing MAV, but rather falls sharply from the beginning of the test. A tractable explanation for the differences is flexible wing bending may cause changes in wing incidence resulting in an increase in C_Y. The values of C_L over the range of β are similar to the C_L values with no sideslip angle and therefore are not presented here. Figure 25 shows flexible and rigid wing C_Y vs. α plots for various β angles.

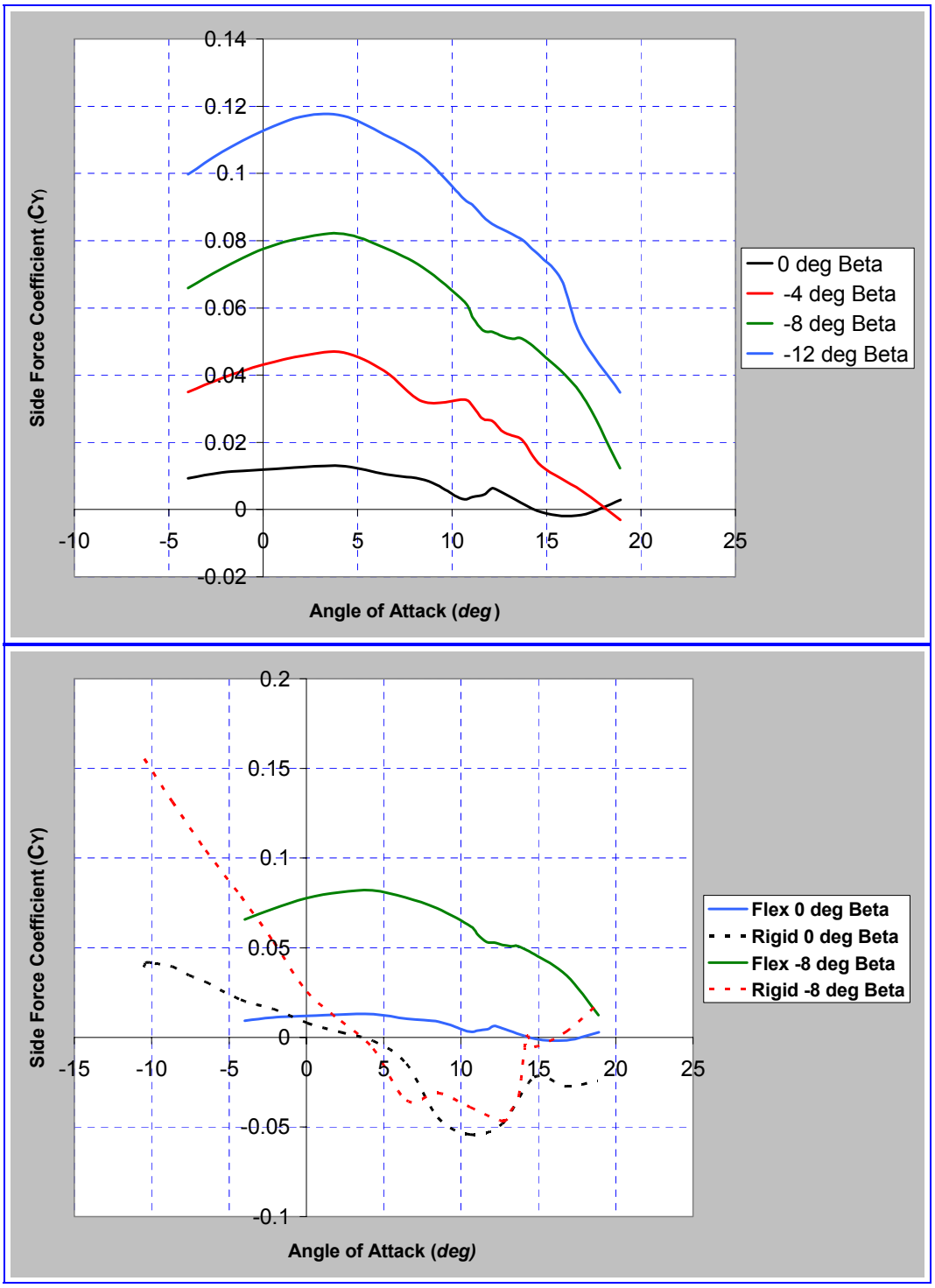

Figure 25. Flexible (left) and Rigid (right) Wing C_Y vs. α for Various Angles of β

Next, plots of the rolling and yawing moments versus angle of attack are shown. The rolling moment (C_ℓ) at the CG behaves consistently with increasing sideslip angle. Similar to the side force coefficient, the roll moment also increases with increasing yaw angle. The flexible and rigid wing roll moment falls sharply with increasing angle of attack. The rigid wing MAV shows more refined behavior than the flexible wing MAV over the entire range of alpha. The magnitude of the rigid wing MAV's roll moment is exceptionally higher than that of the flexible wing MAV. At $\alpha = -4°$, the rigid wing roll moment is 50% higher than the flexible wing roll moment. At $\alpha = 8°$, the rigid wing roll moment is 11 times greater than the flexible wing roll moment. Note; however, at $\alpha = +10°$, the flexible roll moments cease to decrease monotonically rendering further comparisons useless. The combination of tip flutter and wing stall at higher angles of attack probably caused the instabilities in the roll moment. See Figure 26 for C_ℓ vs. α for various β angles.

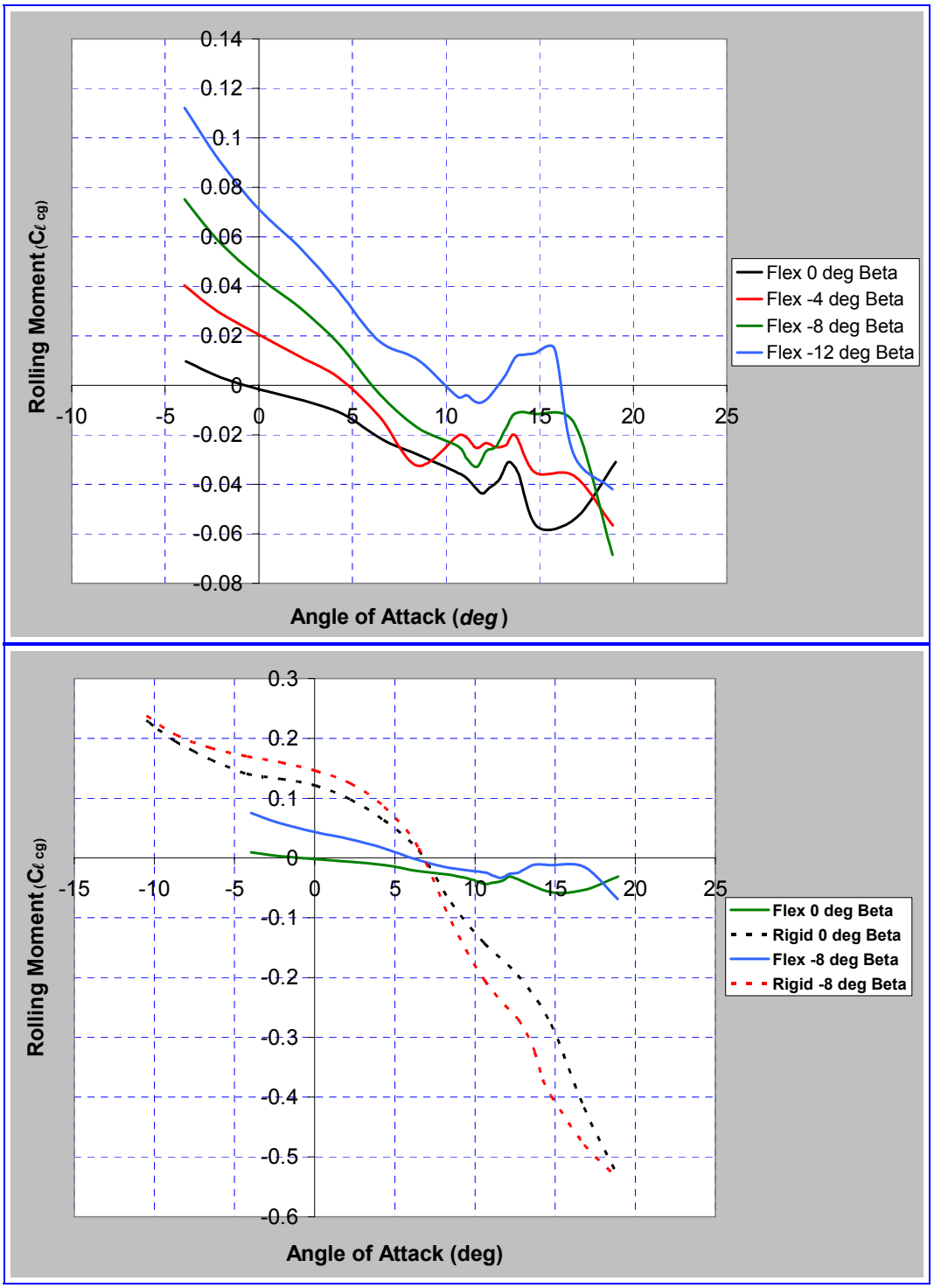

Figure 26. Flexible and Rigid Wing C_ℓ vs. α for Various Angles of β

The dependence of the yaw moment (C_n) at the CG on the angle of attack for various yaw angles is shown in Figure 27. The flexible wing MAV yaw moment responds predictably with increasing yaw angle. The flexible wing yaw moment decreases with angle of attack until $\alpha = 12°$, then begins to increase. It appears the yaw moment displays some oscillatory behavior. Although inconclusive, if the angle of attack was continually increased beyond $\alpha = 20°$, the trend indicates the yaw moment would begin to decrease again. The rigid wing yaw moment behavior is opposite that of the flexible wing MAV. At this point, aeroelastic effects due to wing deformation do not appear as a reasonable explanation for this phenomenon. The yaw moment is measured about the z-axis, and perturbations in wing shape should not effect the direction of the yaw moment. However, the possibility of the CG shifting due to battery placement produces considerable error margin in the flexible and rigid wing C_n moment curves. The flexible MAV x_{CG} can shift by approximately ± 0.066″, while the rigid x_{CG} can shift by ± 0.058″. The flexible MAV z_{CG} can shift by approximately ± 0.033″, while the rigid z_{CG} can shift by ± 0.029″. See Appendix E for a complete CG error analysis.

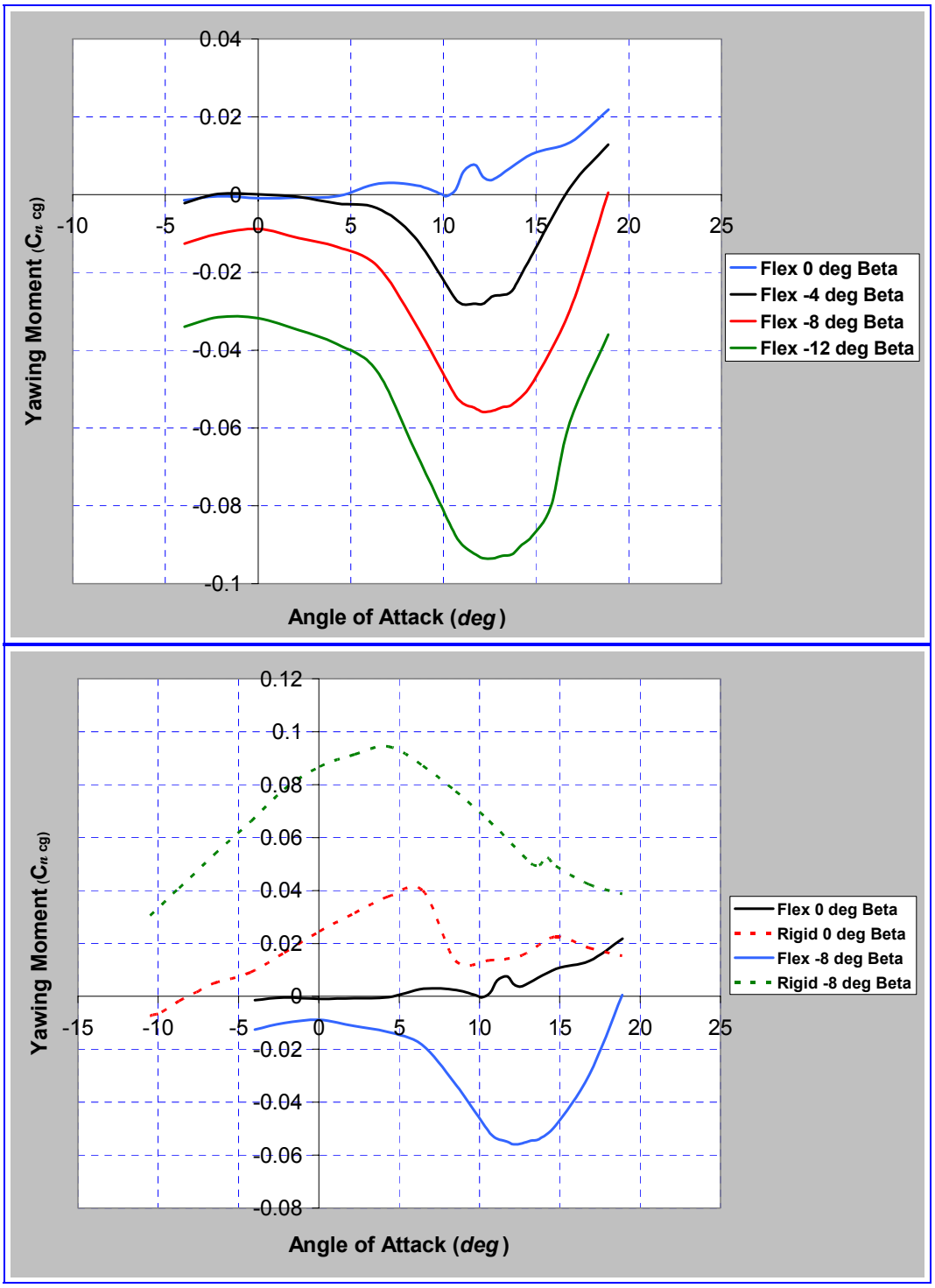

Figure 27. Flexible and Rigid Wing C_n vs. α for Various Angles of β

Static Stability and Control.

The three static stability derivatives are about the Roll, Pitch, and Yaw axes. Stability about the pitch axis is called longitudinal stability, defined as $C_{m\alpha}$. This is stability about the vehicle's y-axis. A vehicle is longitudinally stable if it returns to equilibrium when its flight path is perturbed with a disturbance in the angle of attack (±α). Formally, longitudinal stability is defined as a negative pitching moment curve: $\partial C_m / \partial \alpha < 0$ (Nelson, 1998:43). Figure 28 shows the pitching moment versus angle of attack for both flexible and rigid wing MAVs. It is clear that the flexible MAV is longitudinally stable while the rigid MAV is not longitudinally stable. There is no apparent relationship between $C_{m\alpha}$ and changes in angle of attack for the rigid wing MAV. Furthermore, another condition of flight control is the ability to maintain trim at a positive angle of attack. Thus, not only does a vehicle have to have $C_{m\alpha} < 0$, it must also have a positive intercept to trim at a positive angle of attack: $C_{m0} > 0$ (Nelson, 1998:43). Again, the flexible MAV can maintain trim at a positive angle of attack at all air speeds because each curve has $C_{m0} > 0$.

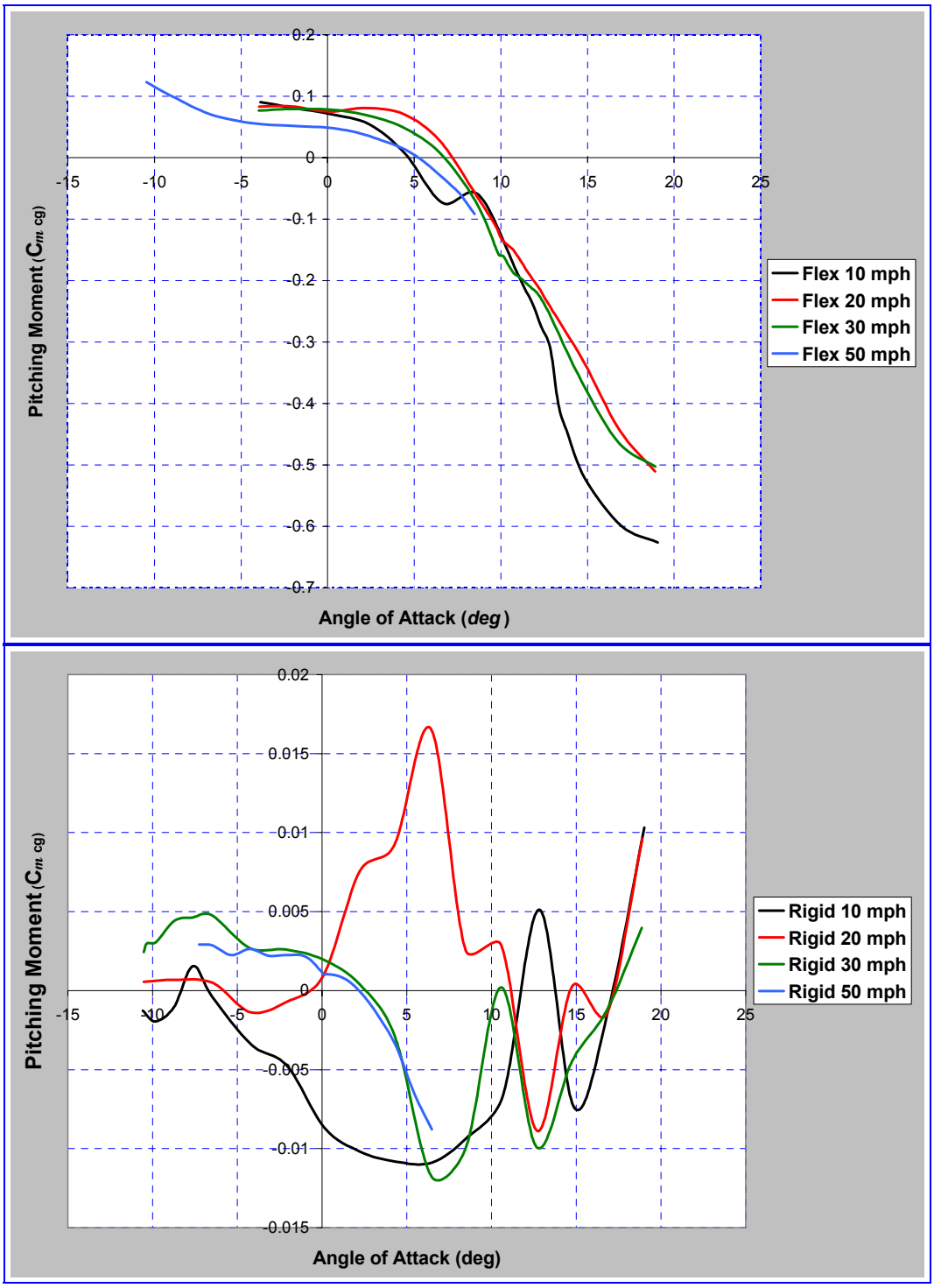

Figure 28. Flexible and Rigid Wing Longitudinal Stability, $C_{m\alpha}$

It appears the rigid wing MAV's pitching moment ranges widely and quickly diverges out of control. The heavier, solid wing construction coupled with the battery not being rigidly fixed inside the cargo compartment moved the location of the X_{CG} rearward, reducing longitudinal stability. See Appendix E for the $C_{m\alpha}$ CG error bar plots. However, a plot of the rigid MAV on the same scale as the flexible MAV reveals considerably less oscillation and a more statically neutral response. In this plot, $C_{m\alpha} = 0$ for the rigid wing MAV. Figure 29 shows a comparison of the flexible and rigid wing longitudinal stability at 20 and 30 mph.

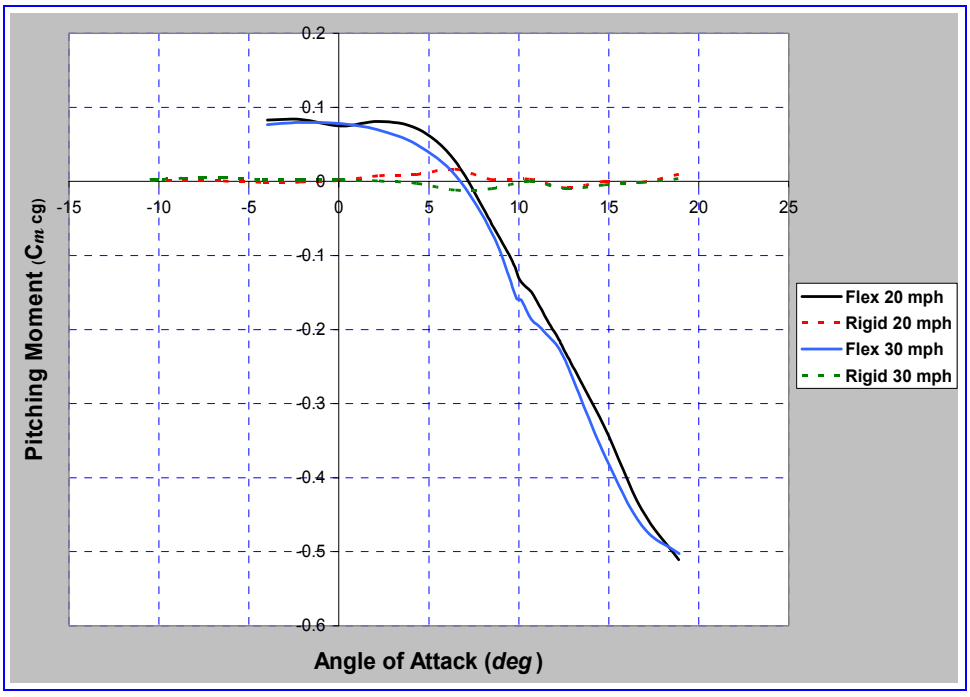

Figure 29. Comparison of Flexible and Rigid Wing $C_{m\alpha}$

Stability about the yaw axis is called directional or *weathercock* stability, defined as $C_{n\beta}$. This is stability about the vehicle's z-axis. A vehicle is directionally stable if it returns to equilibrium when provided with a yaw angle ($\pm\psi$) disturbance. Formally,

directional stability is defined as a positive yawing moment curve: $\partial C_n / \partial \beta > 0$ (Nelson, 1998:73). Figure 30 shows the yawing moment versus sideslip angle for both flexible and rigid wing MAVs. It is clear that the flexible wing MAV is directionally stable while the rigid wing MAV is not directionally stable. The value of $C_{n\beta}$ decreases as the angle of attack increases. Within each run, $C_{n\beta}$ also decreases with decreasing sideslip angle. A directionally stable vehicle will always, by default, point into the relative wind. Again, wing weight or a slight CG shift may be the explanation for the differences between the rigid and flexible wing MAVs. One notable caveat, the rigid wing MAV was only tested at two yaw angles, $\psi = 0° \ \& \ 8°$.

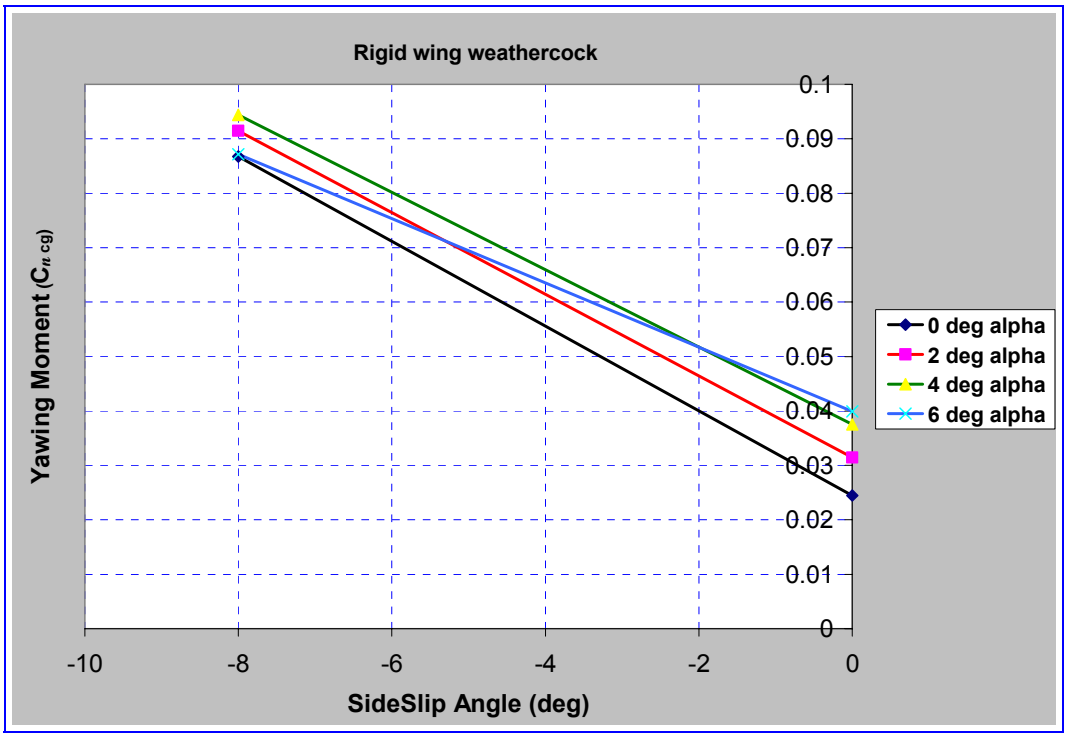

Figure 30. Flexible and Rigid Wing Directional Stability, $C_{n\beta}$

Stability about the roll axis is called roll stability, defined as $C_{\ell\beta}$. This is stability about the vehicle's x-axis. A vehicle is stable in roll if it returns to equilibrium when disturbed from *wings level*, which is in the form of ±φ. Formally, roll stability is defined as a negative rolling moment curve: $\partial C_{\ell} / \partial \beta < 0$ (Nelson, 1998:78). Figure 31 shows the rolling moment versus sideslip angle for both flexible and rigid wing MAVs. Both MAVs exhibit roll stability. The flexible wing MAV shows clear roll stability, while the rigid wing MAV's slope is only slightly negative and intimates at being neutrally stable in roll. The roll moment generated by vehicle sideslip depends on wing placement (high or low), dihedral, sweep, position on body, and tail geometry (Nelson, 1998:79). Wing

dihedral angle, Γ, is the primary factor contributing to the direction of $C_{\ell\beta}$ (Nelson, 1998:79). The MAV wings are high mounted, without sweep or dihedral.

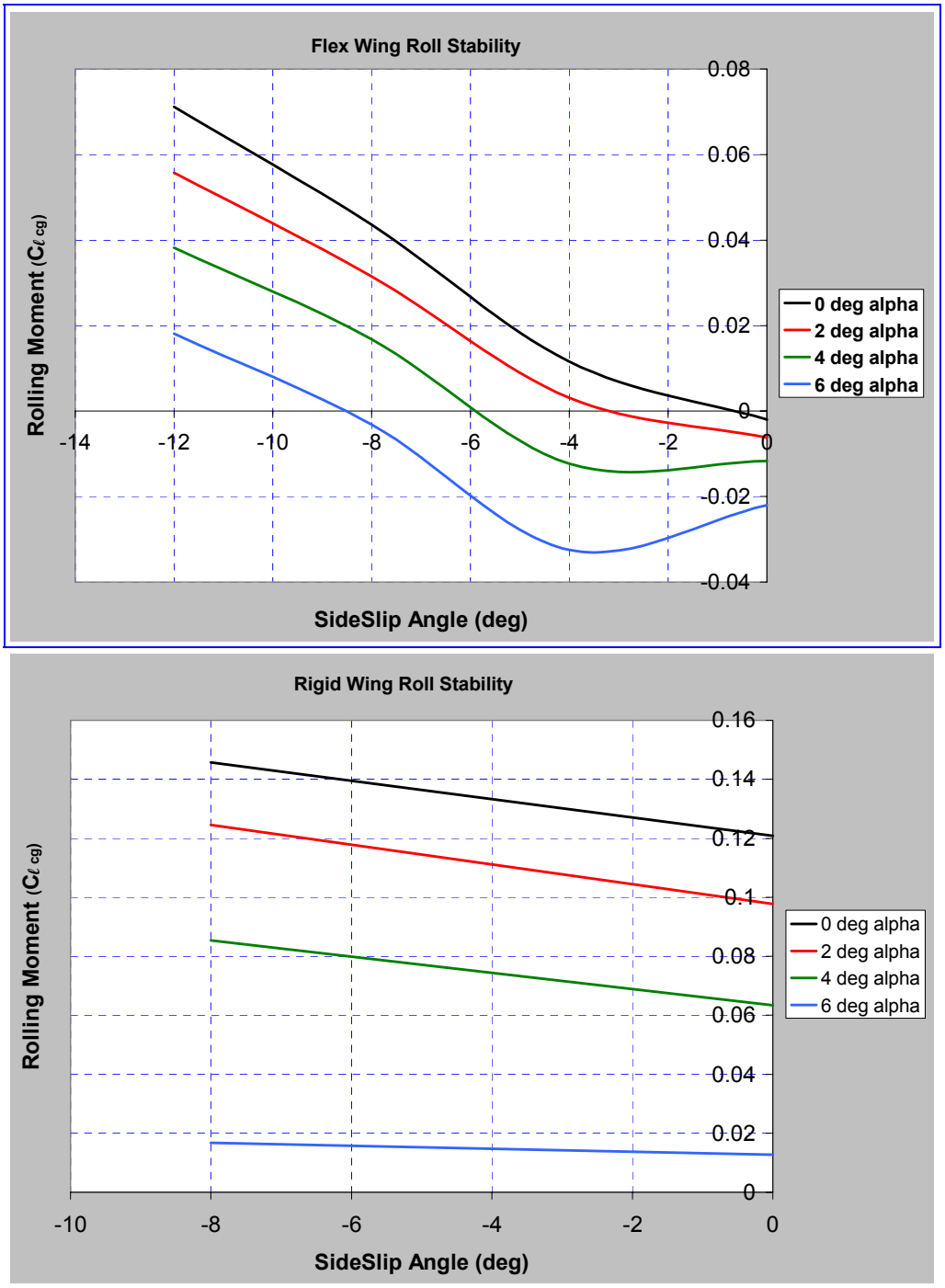

Figure 31. Flexible and Rigid Wing Roll Stability, $C_{\ell\beta}$

Table 16 summarizes the stability and control section of this document by presenting the average slopes for each of the flexible wing stability derivatives. Note, these are average values, which are strongly influenced by the particular α and β angles of each run.

Table 16. Slopes of the Stability Derivatives

$\partial C_m / \partial \alpha$	-0.0466
$\partial C_n / \partial \beta$	+0.0044
$\partial C_\ell / \partial \beta$	-0.0066

Elevon Deflected Runs

The elevon deflected lift and drag plots are presented in Appendix A. The area of concern when referencing control surface deflections is the vehicle's control response per increment of control surface movement. These vehicles do not possess traditional flight control surfaces such as ailerons, flaps, elevators, and a rudder. Instead, the MAVs use a pair of elevons oriented at 45° in a V-tail configuration to accomplish the functions of the aforementioned control surfaces. For all plots, positive elevon deflections are toward the center of the MAV and negative elevon deflections are down and away from the MAV center. See Appendix C for pictures of the MAV's tail in various elevon deflection configurations. The results are presented as the pitch, roll, and yaw moment responses to the various control surface input configurations.

Single Elevon Deflection

Minor angle of attack adjustments and slight direction changes are accomplished by deflecting a single elevon. Although not the typical use of the elevon control surfaces, the small flight forces encountered enable considerable MAV orientation changes with only a single elevon. Figure 32 presents the pitching moment versus the change in a single elevon ($\delta_{e,\,STARBOARD}$) only. The value of C_m increases as δ_e increases and shows consistent behavior throughout the entire range of elevon deflections. However, there is ≈ 7° of asymmetry in the C_m curves at $\alpha = 0°$, 2°, & 4°. This asymmetry, also present in the tandem elevon runs, is probably a result of unequal epoxy bonding of the wings to fuselage. If one wing tip deflects slightly more than the other, the effect would manifest itself as a nonzero moment at $\delta_e = 0°$. Unlike the $\alpha = 6°$ run, C_m becomes positive at negative elevon deflection angles. Repositioning of the battery pack could slightly change the CG so $C_{m_O} = 0$ at $\delta_e = 0°$. A slight bump occurs after ±10° δ_e, but is rather minor and should not influence flight performance.

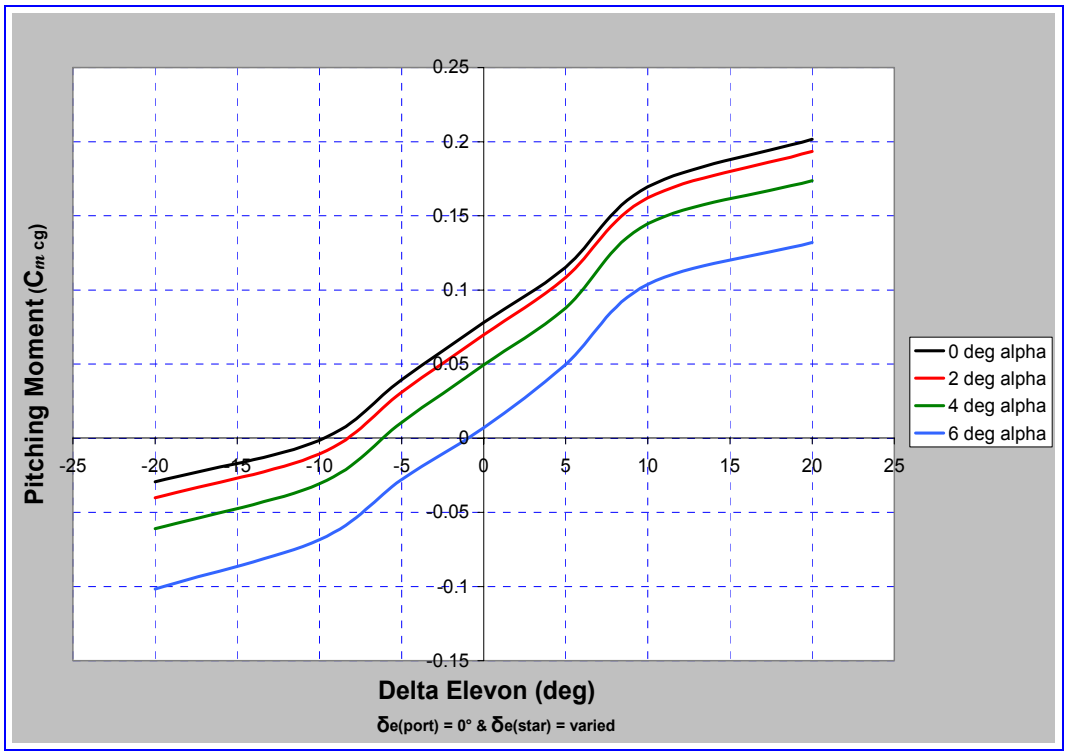

Figure 32. Flex Wing MAV C_m vs. δ_{Elevon} (Single)

Aside from altering the vehicle's attitude, the horizontally projected plane portion of a single deflected elevon, serves as an aileron and can roll the vehicle about its longitudinal axis. Figure 33 presents the roll moment versus the change in a single elevon. The roll moment behavior is similar to the pitching moment behavior; however, the pitching moment is approximately 14 times greater than the roll moment. Thus, it is readily apparent that C_ℓ is less impacted by a singularly deflected elevon than C_m. The C_ℓ curves are slightly more symmetric than the C_m curves, displaying only $\approx 5°$ of asymmetry at $\alpha = 2°$, 4°, & 6°. Unlike the $\alpha = 0°$ run, C_ℓ remains negative at positive elevon deflection angles up to $\delta_e = +5°$. Furthermore, a nearly equidistant spread between each alpha run strongly suggests a correlation between C_ℓ and the angle of

attack. Again, after $\delta_e = \pm 10°$, the same slight bump in C_m occurs in C_ℓ, which should also not affect flight performance.

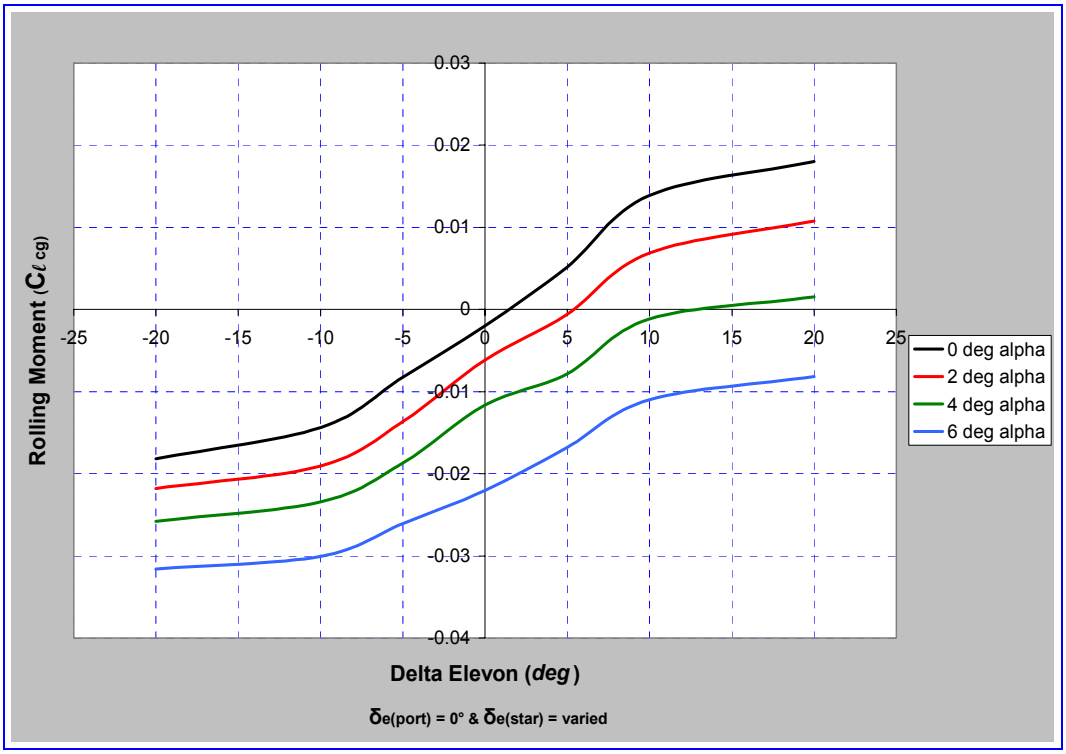

Figure 33. Flex Wing MAV C_ℓ vs. δ_{Elevon} (Single)

The yawing moment is also affected by a single elevon deflection. It is twice the magnitude of the rolling moment and five times smaller than the pitching moment. Figure 34 depicts the yaw moment versus the change in a single elevon. The clustering of all of the alpha runs into a nearly coincident line implies no correlation between C_n and a change in alpha. Excellent symmetry exists in all of the C_n curves. Equivalent positive and negative deflections produce identical yaw to both the port and starboard sides of the MAV. At $\delta_e = \pm 10°$, the bump in C_n becomes further pronounced and could potentially change the expected control response.

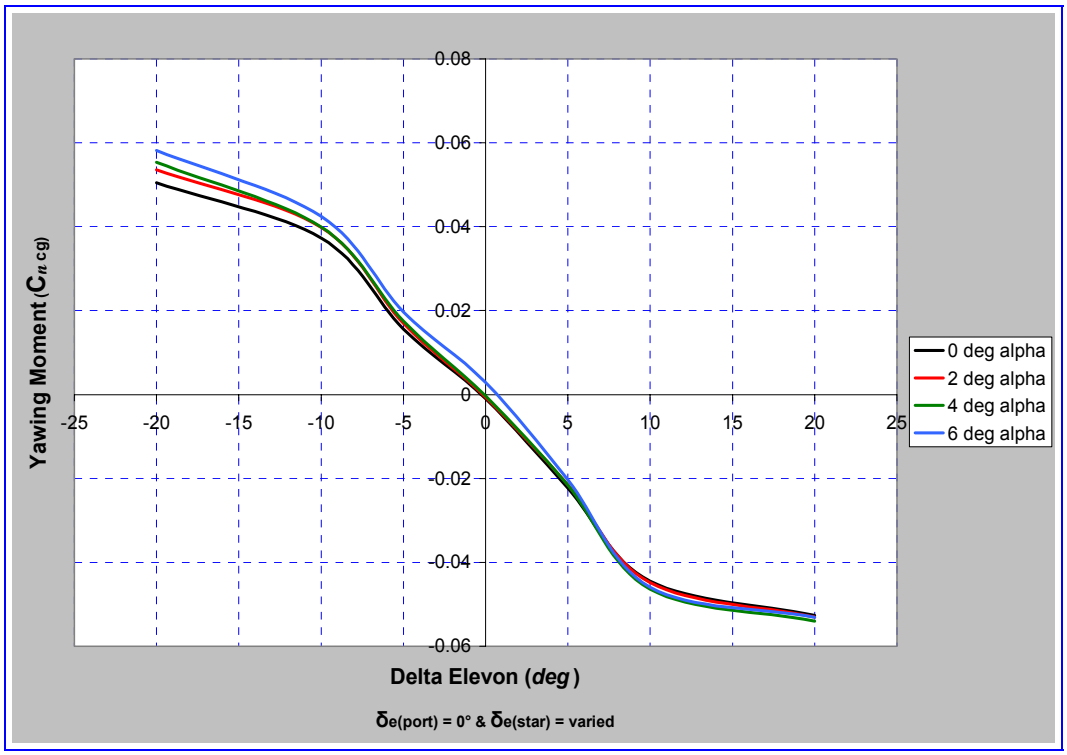

Figure 34. Flex Wing MAV C_n vs. δ_{Elevon} (Single)

Table 17 provides a summary for some of the single elevon moment parameters discussed in the preceding section.

Table 17. Summary of Single Elevon Deflection Runs

Single δ_e	C_m		C_ℓ		C_n	
Max Value $\delta_e = +20°$	$\alpha = 0°$	0.25	$\alpha = 0°$	0.018	$\alpha = 6°$	0.06
Min Value $\delta_e = -20°$	$\alpha = 6°$	-0.1	$\alpha = 6°$	-0.03	N/A	-0.05
Asymmetry	$\approx 7°$		$\approx 5°$		$\approx 0°$	
%Δ of Largest	Largest		Max: C_m is 93% > C_ℓ		Max: C_m is 76% > C_n	
			Min: C_m is 70% > C_ℓ		Min: C_m is 50% > C_n	

Tandem Elevon Deflection

Elevons deflected in tandem are a more standard method of vehicle control than using only single elevon deflections. Tandem elevon movement, also called symmetric elevon deflection, is primarily used for aircraft attitude and pitch control. According to Martin Waszak's N.A.S.A wind tunnel report on the UF 6″ MAV, tandem elevon deflections minimally affect the sideforce coefficient, rolling moment, and yawing moment (Waszak and Jenkins: 2001:5). Figure 35 presents the pitching moment versus the change in tandem elevon deflection ($\delta_{e,\,PORT} = \delta_{e,\,STARBOARD}$). This C_m curve exhibits the same trends as the single elevon pitching moment curves. The asymmetry at $\alpha = 0°$, 2°, & 4° is ≈ 3°, a 42% average reduction in the asymmetry over the single elevon C_m curves. The magnitude of the tandem elevon C_m curve is 2.0 times greater at the minimum negative deflection ($\delta_e = -20°$) and 1.3 times greater at the maximum positive deflection ($\delta_e = +20°$) than the magnitude of the single elevon C_m curve.

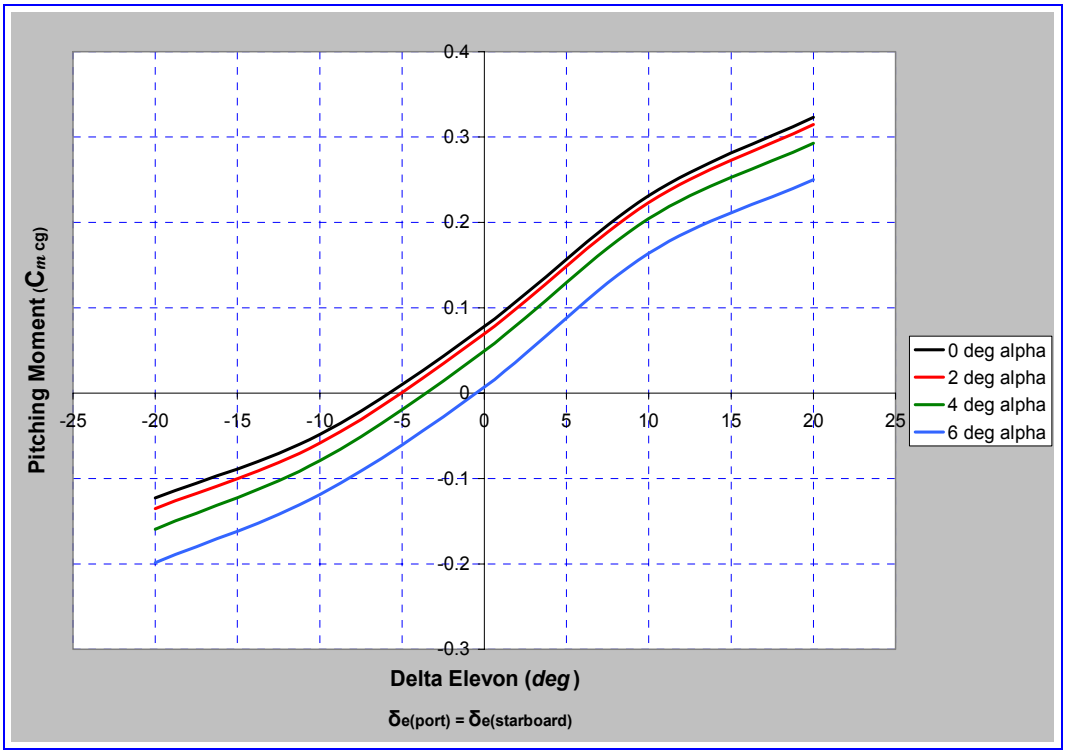

Figure 35. Flex Wing MAV C_m vs. δ_{Elevon} (Tandem)

The small magnitudes in the roll moment are evidence of the minor influence tandem elevon deflections have on C_ℓ. Figure 36 depicts the roll moment versus the change in tandem elevon deflection. The C_ℓ curves for the $\alpha = 2°, 4°, \& 6°$ runs are negative through the range of elevon deflections. Thus, any tandem elevon input at an angle of attack results in a negative rolling moment. Similar to the single elevon C_ℓ curves, the spread between runs suggests strong angle of attack dependence. One immediate difference between the single elevon and the tandem elevon C_ℓ curve is the flatness in the slopes as well as the sign reversal after $\delta_e = \pm 10$ °. Although their magnitudes are minor, these sign reversals implicate stability problems beyond $\delta_e = \pm 10°$. From the C_ℓ curves, a well-defined control regime is apparent in the elevon range of $-10° \leq \delta_e \leq +10°$. The magnitude of the tandem elevon C_ℓ curve is 1.2 times greater at the

minimum negative deflection (δ_e = -10°) and 3.6 times greater at the maximum positive deflection (δ_e = +10°) than the magnitude of the single elevon C_ℓ curve.

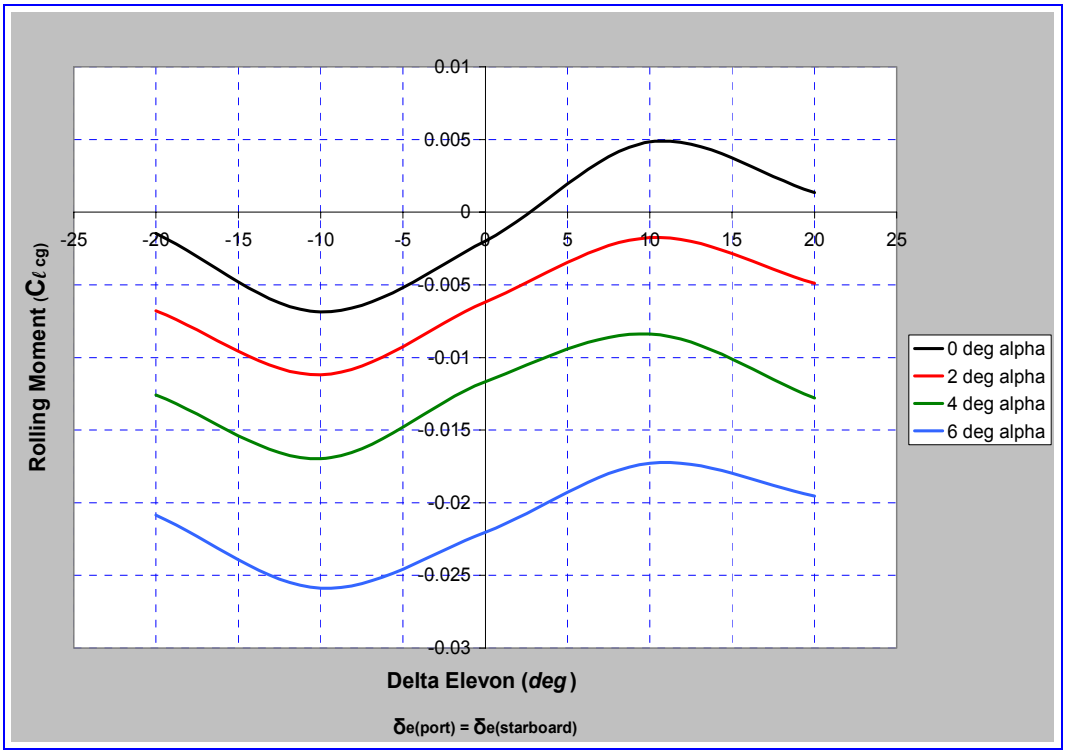

Figure 36. Flex Wing MAV C_ℓ vs. δ_{Elevon} (Tandem)

Lastly, the yaw moment is also small in comparison to the pitching moment. Figure 37 presents the roll moment versus the change in tandem elevon deflection. The yaw moment is nearly symmetrical and appears largely independent of the angle of attack, rendering smooth and predictable yaw reaction over the range of alpha. However, at $\delta_e = \pm 10°$, there is an even greater sign reversal in the tandem C_n curve than seen in the tandem C_ℓ curve. The same well-defined handling control regime occurs over the elevon range of $-10° \leq \delta_e \leq +10°$. Beyond $\delta_e = \pm 10°$, handling qualities will rapidly change, requiring a considerable control input restoring effort. The maximum magnitude of the

single elevon C_n curve is 2.9 times greater at the minimum negative deflection (δ_e = -10°) and 3.75 times greater at the maximum positive deflection (δ_e = +10°) than the maximum magnitude of the tandem elevon C_ℓ curve.

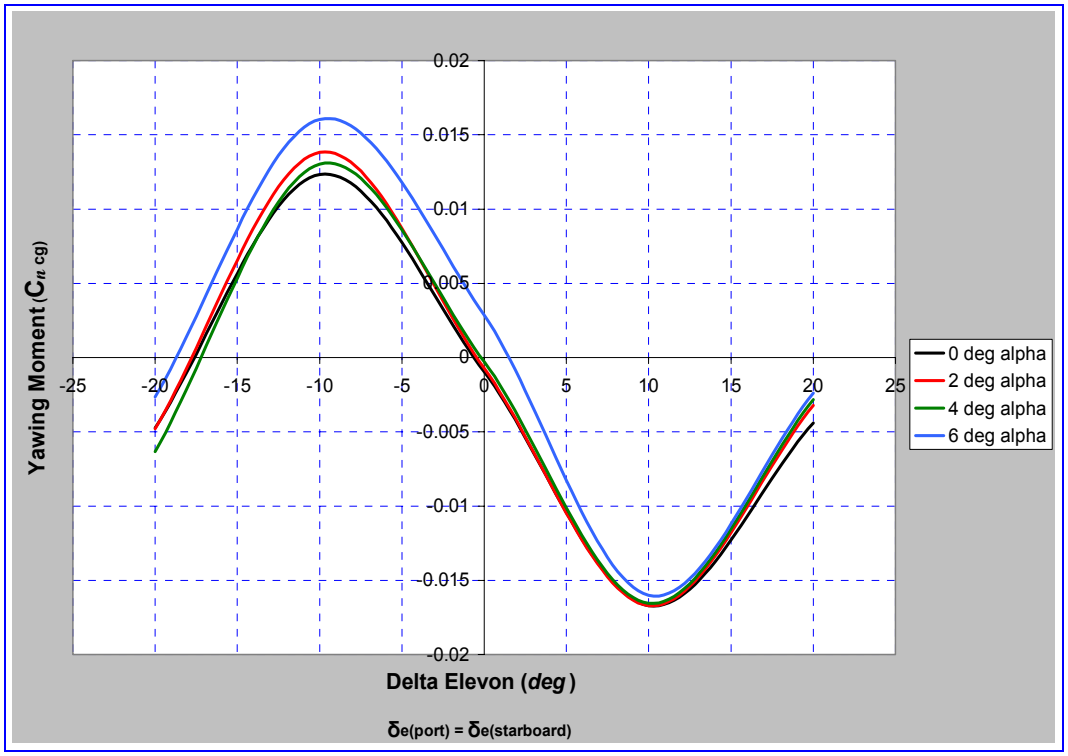

Figure 37. Flex Wing MAV C_n vs. δ_{Elevon} (Tandem)

Table 18 provides a summary for some of the tandem elevon moment parameters discussed in the preceding section.

Table 18. Summary of Tandem Elevon Deflection Runs

Tandem δ_e	C_m		C_ℓ		C_n	
Max Value $\delta_e = 10°$	$\alpha = 0°$	0.32	$\alpha = 0°$	0.005	$\alpha = 6°$	0.016
Min Value $\delta_e = -10°$	$\alpha = 6°$	-0.2	$\alpha = 6°$	-0.025	N/A	-0.017
Asymmetry	$\approx 5°$		All angles (-)		$\approx 0°$	
%Δ of Largest	Largest		Max: C_m is 98% > C_ℓ		Max: C_m is 95% > C_n	
			Min: C_m is 88% > C_ℓ		Min: C_m is 92% > C_n	

Opposed Elevon Deflections

Opposed elevon deflection, sometimes called antisymmetric elevon deflection, is used to alter the MAV's heading and direction by producing large changes in the rolling and yawing moments. In an ideal environment, opposed elevons should produce a negligible pitching moment because each elevon generates an equal but opposite moment, effectively canceling one another. Figure 38 presents the pitching moment versus the change in opposed elevon deflection ($\delta_{e,\,PORT} = -\delta_{e,\,STARBOARD}$). This C_m curve is vastly different from the single and tandem elevon pitching moment curves. The pitching moment experiences dramatic sign reversals for all angles of attack at $\delta_e = \pm 10°$, which can cause unpredictable handling challenges. The spread between each alpha run is inconsistent with the highest C_m values occurring at $\alpha = 0°$. Increasing the angle of attack exposed the control surfaces to lower dynamic pressures mitigating the response. The C_m value at $\alpha = 0°$ is about twice the value at $\alpha = 6°$. The maximum magnitude of the single elevon C_m curve is approximately 1.85 times greater at the maximum positive

deflection than the magnitude of the maximum moment of the opposed elevon C_m curve. The magnitude of the tandem elevon C_m curve is about 2.46 times greater at its maximum positive deflection than the magnitude of the maximum moment opposed elevon C_m curve. The maximum magnitude of the single elevon C_m curve is 10 times greater at the minimum positive deflection than the magnitude of the opposed elevon C_m curve, and the magnitude of the tandem elevon C_m curve is about 20 times greater than the magnitude of the opposed elevon C_m curve.

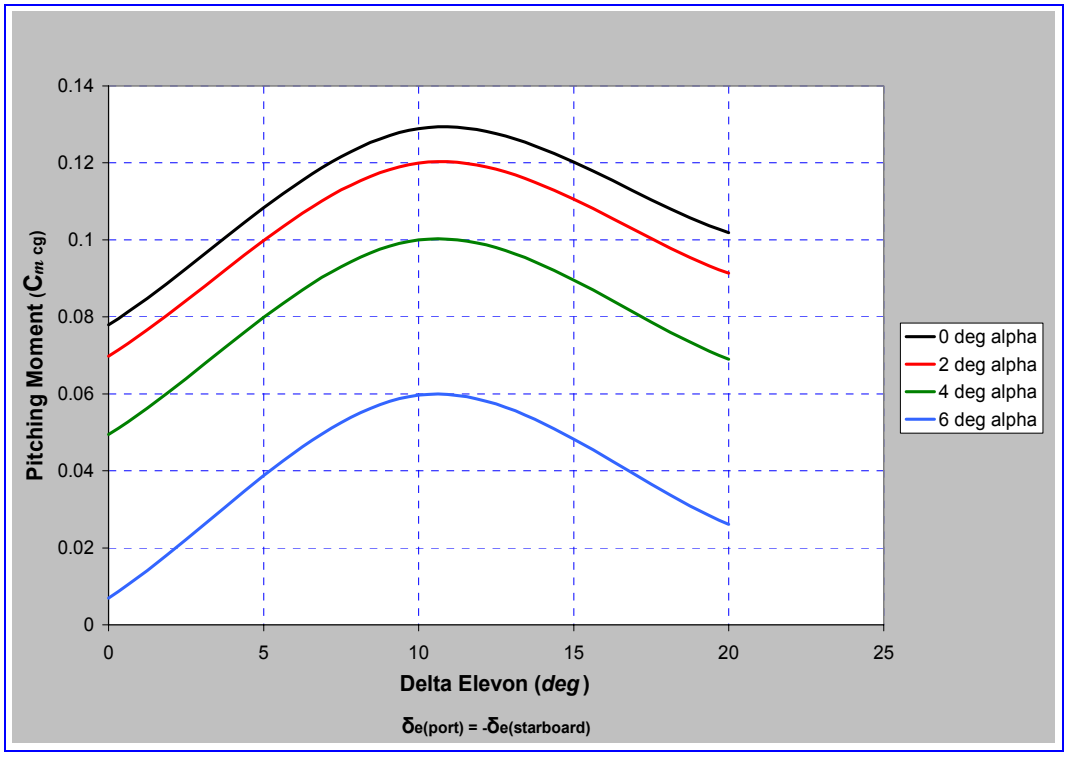

Figure 38. Flex Wing MAV C_m vs. δ_{Elevon} (Opposed)

The rolling moment curve, as expected, is considerably more influenced by the elevons deflected in opposition than any other configuration. Figure 39 depicts the roll moment versus the change in opposed elevon deflection. The C_ℓ curves are nearly

equidistant from one run to the next, decreasing in C_ℓ as the angle of attack increases. Notice, with $\delta_e = 0°$, a small amount of C_ℓ develops as the alpha increases. The opposed elevon deflection C_ℓ curves do not exhibit any dramatic changes in the direction of the slope, although there is a slight elbow in all of the curves at $\delta_e = \pm 10°$, which should result in benign handling characteristics. The maximum magnitude of the opposed elevon C_ℓ curve is 2.1 times greater at the maximum positive deflection ($\delta_e = \pm 20°$) than the magnitude of the maximum moment of the single elevon C_ℓ curve, and 7.5 times greater than the magnitude of the maximum moment of the tandem elevon C_ℓ curve. MAV direction control should be predictable and well behaved using opposing elevon deflection.

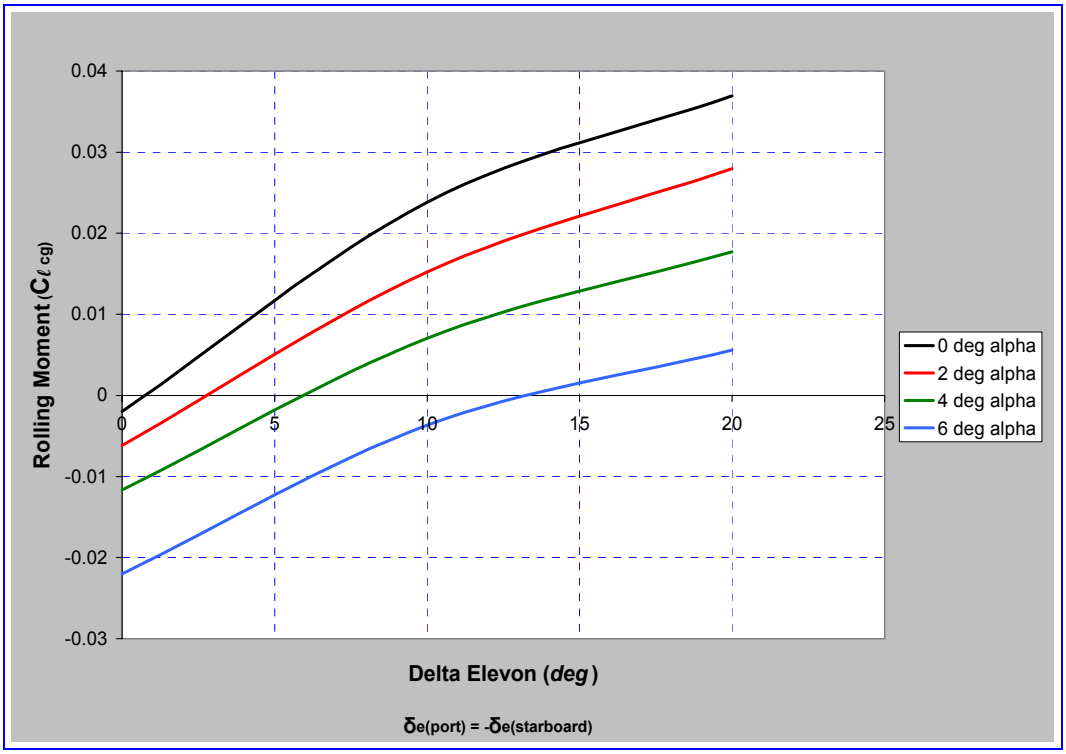

Figure 39. Flex Wing MAV C_ℓ vs. δ_{Elevon} (Opposed)

The last of the control surface analysis is the opposed elevon induced yawing moment. Recall, since the MAV does not have ailerons, elevators, or a rudder, the elevons are responsible for executing all of their functions. On a traditional aircraft with classic control surfaces, a well-coordinated turn is accomplished through a combination of aileron and rudder inputs – aerodynamically, it is a blending of both roll and yaw moments respectively. This effect is accomplished simultaneously with the MAV's elevons. The second component of the direction and heading control is the yaw moment. Figure 40 depicts the roll moment versus the change in opposed elevon deflection. All of the runs are coincident indicating the yawing moment is unaffected by changes in the angle of attack. The slope is steep, implying a fast rate of response to antisymmetric deflection. Comparing the C_{ℓ} and C_{n} curves at each δ_e setting, it is apparent the rate of change of C_{n} with δ_e is higher than that of C_{ℓ}; therefore, the MAV's turns will resemble more of a pivot than a roll. Similar to the C_{ℓ}; curves, the C_{n} curves do not show any sign reversals. Flight response should be crisp and predictable. The maximum magnitude of the C_{n} curve is 3.6 times greater at the maximum negative deflection ($\delta_e = \pm 20°$) than the magnitude of the maximum moment of the single elevon C_{ℓ} curve, and 10.6 times greater than the magnitude of the maximum moment of the tandem elevon C_{n} curve.

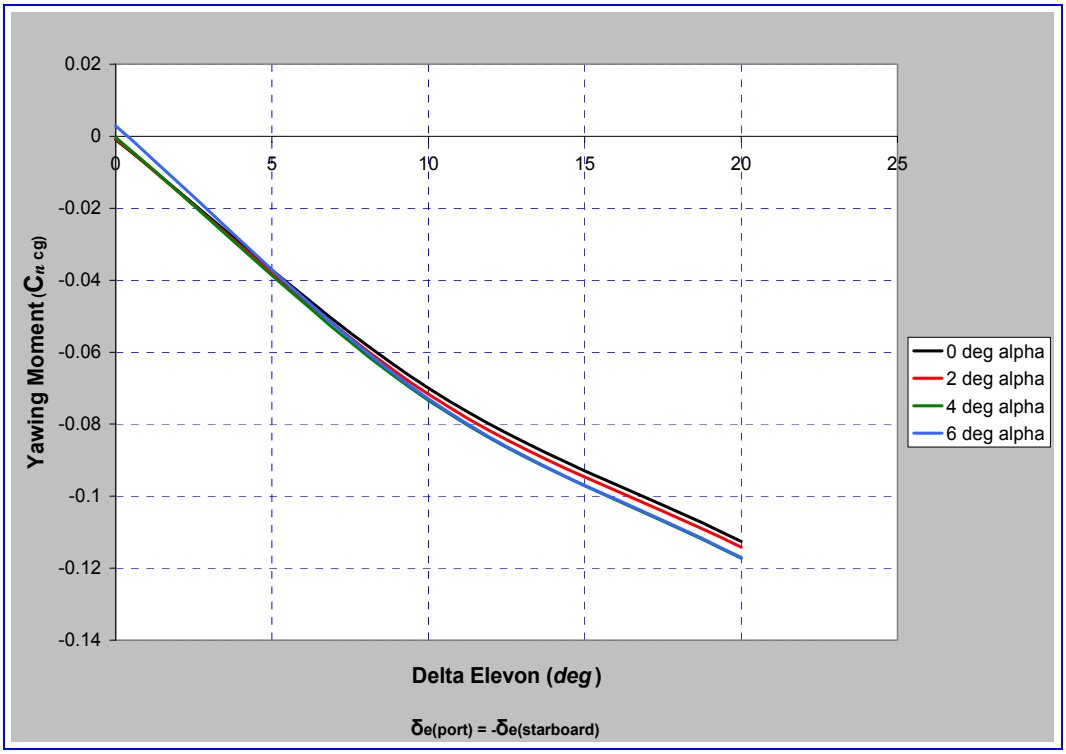

Figure 40. Flex Wing MAV C_n vs. δ_{Elevon} (Opposed)

Table 19 provides a summary for some of the opposed elevon moment parameters discussed in the preceding section.

Table 19. Summary of Opposed Elevon Deflection Runs

Opposed δ_e	C_m		C_ℓ		C_n	
Max Value	$\alpha = 0°$	0.13	$\alpha = 0°$	0.038	N/A	0.0
Min Value	$\alpha = 6°$	0.01	$\alpha = 6°$	0.005	N/A	-0.181
%Δ of Largest	|Max|: C_n is 38% > C_m		|Max|: C_n is 380% > C_ℓ		Largest	

Table 20 summarizes the elevon deflected runs section of this chapter by presenting the average slopes for all of the flexible wing elevon-deflected runs.

Table 20. Slopes of the Elevon Deflected Runs

U_∞ = 30 mph	Single $\delta_{e,P} = 0$	Tandem $\delta_{e,P} = \delta_{e,S}$	Opposed $\delta_{e,P} = -\delta_{e,S}$
$\partial C_m / \partial \delta_e$	0.0087	0.0133	0.0020
$\partial C_\ell / \partial \delta_e$	0.0012	0.0005	0.0021
$\partial C_n / \partial \delta_e$	-0.0043	-0.0015	-0.0072

Powered Runs

The power runs provide a rough glimpse of the motor/propeller combination's performance over a range of RPM settings. The power coefficient, C_P, and the thrust coefficient, C_T, are the parameters used to quantify this performance. These coefficients are dependent on the advance ratio, the Reynolds number, and the Mach number. Since the flow conditions are well below compressible Mach numbers, the advance ratio becomes the predominant nondimensional parameter. Figure 41 presents C_P and C_T versus changes in the advance ratio at U_∞ = 10 mph. As the RPMs increase, *J* decreases, as does C_P. Recall from equation **(28),** that C_P is a $\mathcal{F}(P / RPM^3)$, so as the throttle is increased, the denominator has a larger influence on C_P. As the RPMs increase, so does

the thrust generated by the propeller, giving way for a corresponding increase in C_T. From equation **(29),** C_T is a $\mathcal{F}(T / RPM^2)$, since the increases in RPM are squared not cubed, the thrust is not dominated by the motor speed. At approximately ⅜ throttle (7500 RPM) the MAV will overcome the 10 mph headwind.

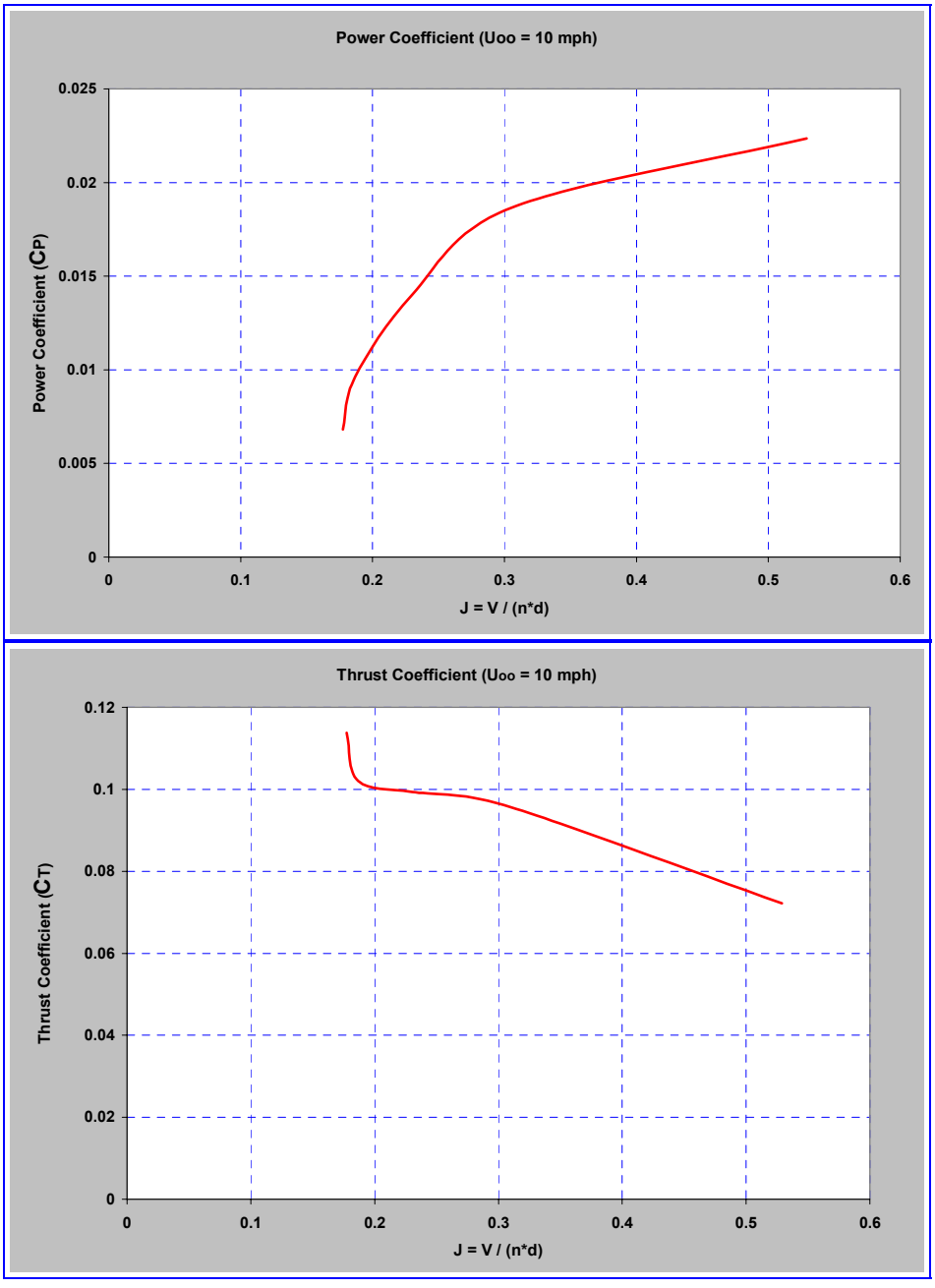

Figure 41. C_P & C_T for U_∞ = 10 mph

Figure 42 shows C_P and C_T versus J for $U_\infty = 20$ mph. The $\alpha = 8°$ C_P data is somewhat skewed due to excessive *windmilling* of the propeller with motor *off*. This problem was most prevalent at the highest alpha setting, probably due to a small tangential force developed by the blades at higher angles of attack. The magnitude of C_P is increasing with a corresponding increase in tunnel speed. The C_T curves demonstrate a well-defined, linear thrust development with increasing throttle. The curves are nearly coincident implying little correlation between the angle of attack and the amount of thrust generated by the propeller. At 0° alpha, the MAV will overcome the 20 mph headwind at approximately ⅜ throttle (10,300 RPM). At alpha = 4° & 8°, the MAV will overcome the 20 mph headwind at approximately ½ throttle (8000 RPM).

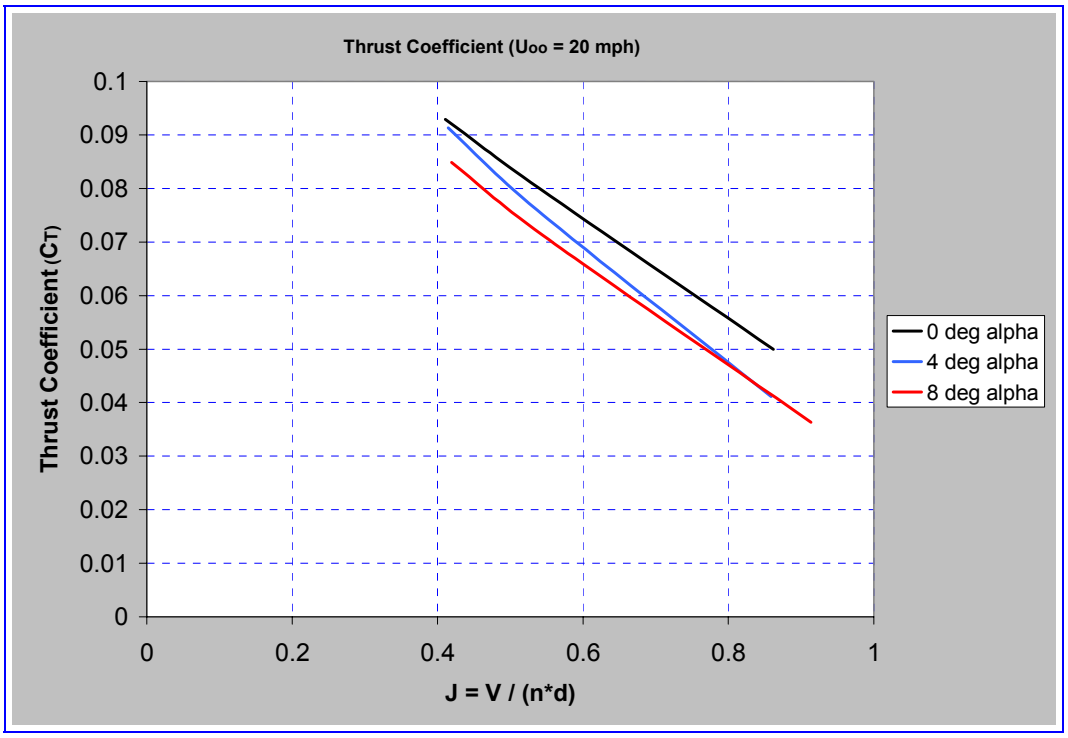

Figure 42. C_P & C_T for U_∞ = 20 mph

Figure 43 shows C_P and C_T versus *J* for U_∞ = 30 mph. The magnitude of C_p continues to increase as the tunnel speed increases. The 30 mph C_p curves show considerable spread from one run to the next. On the surface, this indicates a correlation between the power coefficient and the angle of attack; however, the fidelity of the power coefficients are suspect because the line-to-line variation in the roll moment, ℓ, is on the order of hundredths of in-lb_f, which is near the balance sensitivity of 0.25%. The C_T curves are very consistent and well behaved. At alpha = 0° & 4°, the MAV will overcome the 30 mph headwind at approximately ½ throttle (10,600 RPM). At 8° alpha, the MAV will overcome the 30 mph headwind at approximately ⅝ throttle (12,700 RPM).

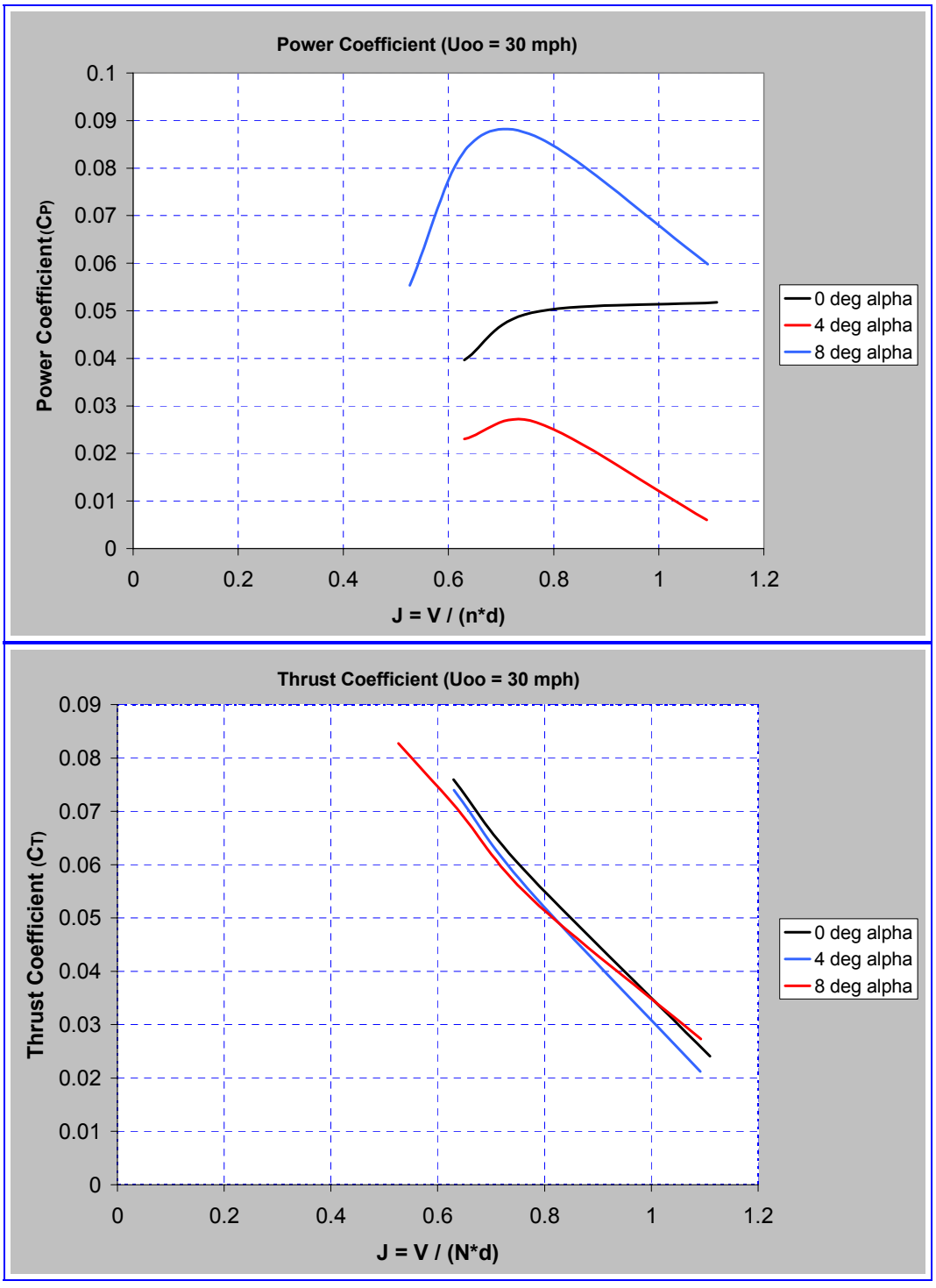

Figure 43. C_P & C_T for $U\infty = 30$ mph

The power runs showed considerable inconsistency in the motor RPM values at each throttle setting. The battery did not supply consistent power to the motor, cutting-out intermittently at different throttle settings, which caused widespread variability in the test conditions. The power coefficients mostly exhibited similar trends, but due to the inability to achieve RPM repeatability at the test throttle conditions, C_P values are inconsistent. This is exacerbated by the dependence of C_P on its cubic RPM relationship. Thrust values, a function of the axial force, tracked predictably with the RPM and throttle settings and showed no dependence on the angle of attack. Table 21 summarizes the maximum and minimum power and thrust coefficient values.

Table 21. Summary of Powered Runs

	C_P				C_T			
U_∞ = 10 mph	Max	%Δ of Max	Min	%Δ of Min	Max	%Δ of Max	Min	%Δ of Min
	0.022	*291%*	0.007	*16.7%*	0.114	*0.0*	0.072	*243%*
U_∞ = 20 mph	Max	%Δ of Max	Min	%Δ of Min	Max	%Δ of Max	Min	%Δ of Min
	0.079	*8.9%*	0.02	*233%*	0.093	*22.6%*	0.036	*71%*
U_∞ = 30 mph	Max	%Δ of Max	Min	%Δ of Min	Max	%Δ of Max	Min	%Δ of Min
	0.086	*0.0*	0.006	*0.0*	0.083	*42.5%*	0.021	*0.0*

The data in graphical format was presented for each group of tests performed on the MAVs. Please refer to Appendix D for the complete numerical data output for all of the

test runs. The tabulated data is presented in the same order as the graphical data for ease of comparison.

Hot-Wire Anemometry

The results of the hot-wire tests revealed the tunnel maintained uniform flow throughout each test run. The open slots used to insert the hot-wire probe into the test section resulted in fluid entrainment, decreasing the flow quality and velocity near the top of the test section. Figure 44 presents mean velocity (U_{mean}) contour plots for the data collected at slot $^{\#}1$. The average turbulent intensity for slot $^{\#}1$ is 2.0%. The recommended operating turbulent intensity is less than 1% (Barlow et al, 1999:126). The tunnel technician, Mr. Gehring, performed a Laser Doppler Velocimetry (LDV) test with theater smoke to verify the turbulent intensity of the tunnel with the solid Plexiglas top plate. These tests reported a turbulent intensity ≈ 0.85%, a 58% reduction over the hot-wire anemometry tests with an open exposure in the top panel. LDV was not used in this test because the theater smoke created a fire code hazard and the local Fire Marshal prohibited further use until a sufficient ventilation system is installed.

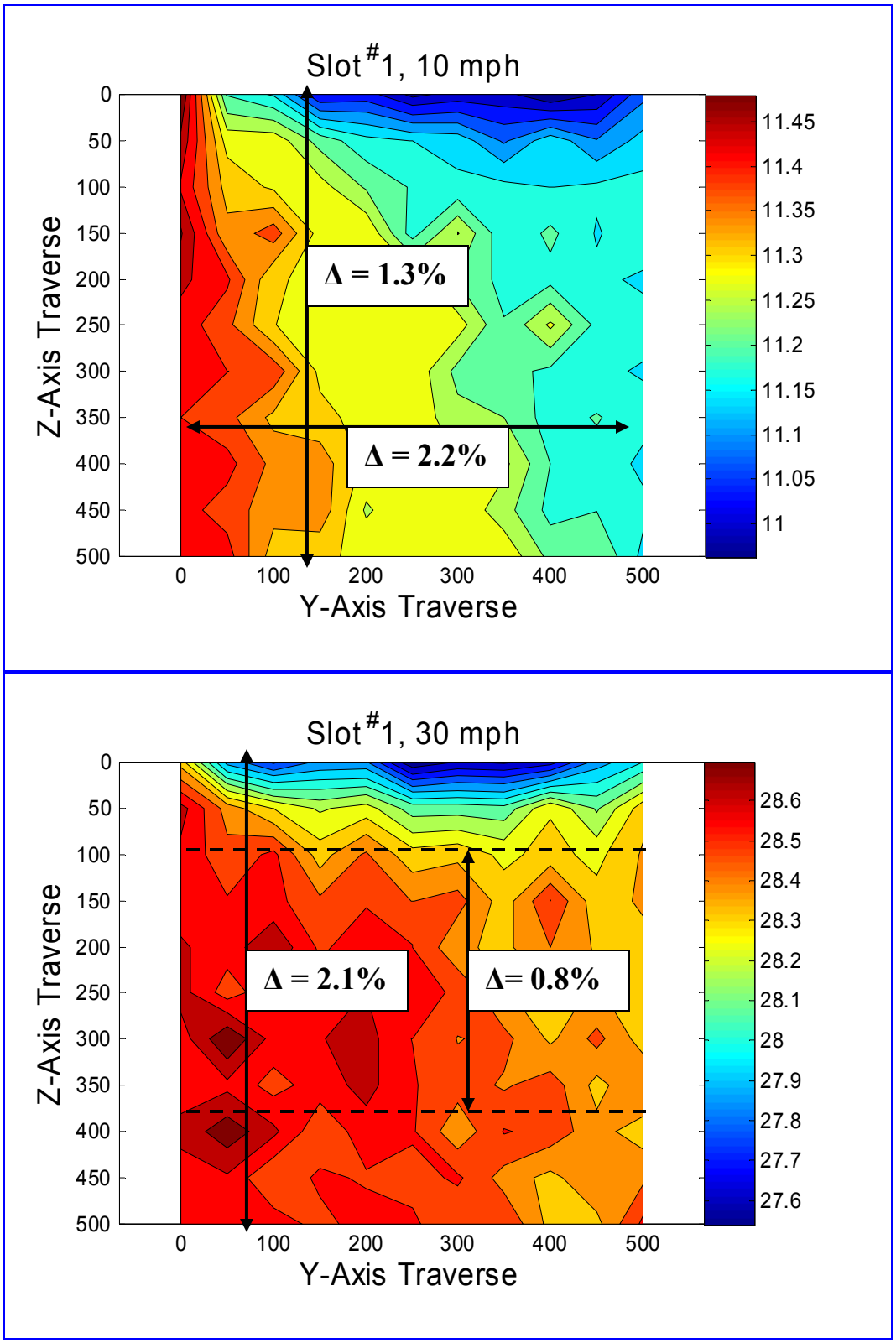
Slot#1, 10 mph
Z-Axis Traverse
Y-Axis Traverse
Δ = 1.3%
Δ = 2.2%
0
50
100
150
200
250
300
350
400
450
500
11.45
11.4
11.35
11.3
11.25
11.2
11.15
11.1
11.05
11
Slot#1, 30 mph
Z-Axis Traverse
Y-Axis Traverse
Δ = 2.1%
Δ= 0.8%
28.6
28.5
28.4
28.3
28.2
28.1
28
27.9
27.8
27.7
27.6

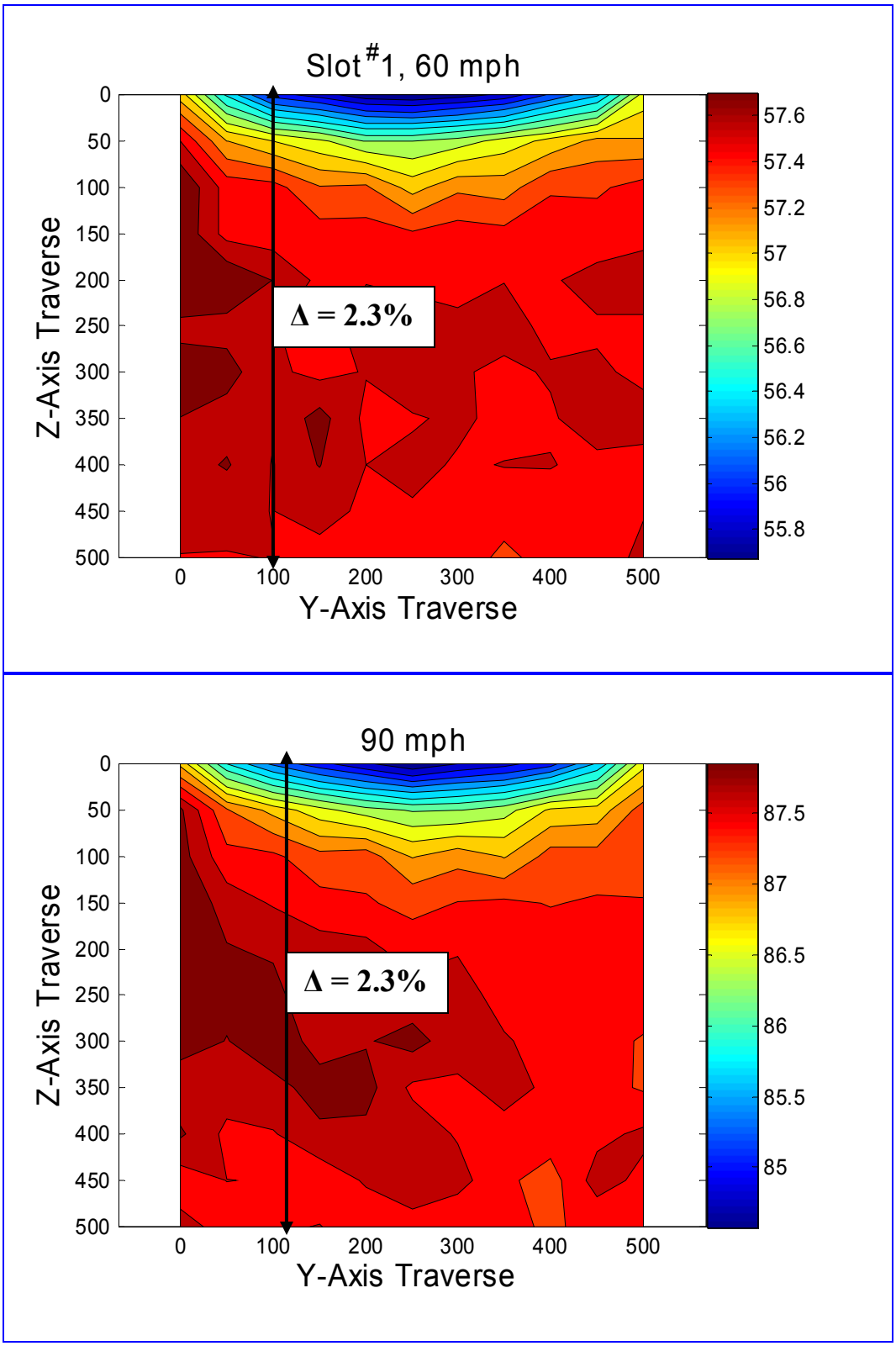

Figure 44. Slot #1 U_{Mean} Velocity Contour Plots

Also note, in the 10 mph case, a distinctive wall-to-wall asymmetry in the velocity is present – a difference of 2.2%. This effect is also present to varying degrees in the other runs as well. Please refer to Appendix B for the contour plots for slots #4 & #6. The cause of this phenomenon is most likely a result of the positioning of the wind tunnel within the lab walls. There is considerable more space on the right side of the tunnel than on the left side of the tunnel. Therefore, since the tunnel is an *open circuit* configuration, the fan sucks the room ambient air through the tunnel. The off-center position of the tunnel creates a velocity gradient where the wind coming from the right side of the tunnel is moving slower than the wind originating from the left side of the tunnel. Table 22 summarizes the percent turbulence for each hot-wire test run.

Table 22. Turbulence % For Each Slot and Velocity

SLOT #	U∞ = 10 mph	U∞ = 30 mph	U∞ = 60 mph	U∞ = 90 mph	Average
One	1.357%	2.154%	2.317%	2.344%	***2.0%***
Four	2.586%	2.73%	2.285%	1.969%	***2.375%***
Six	2.62%	2.127%	2.664%	2.199%	***2.375%***

Limitations of Experimental Effort

The ABLE corporation balance used to collect raw force and moment data has a resolution of 0.25%. The normal force sensors have a maximum load capacity of 8 lb_f; therefore, they can accurately measure load variations as small as 0.02 lb_f. The axial and

side force sensors have a maximum load capacity of 5 lb_f; therefore, they can accurately measure load variations as small as 0.0125 lb_f. In certain test runs, specifically at the lowest tunnel speeds, the raw data showed point-to-point variations on order of the balance precision; therefore, some of the data contains equipment induced determinate experimental error. Quantization error of the 16-bit data acquisition card, the uncertainty due to the standard deviation of a given strain gauge mean voltage measurement, and the accuracy of the tare polynomials also represent sources of uncertainty leading to errors in the data output. See Appendix E for a more definitive error analysis.

The placement of the battery inside the electronics bay of each MAV is not exact. There is no specific battery compartment; therefore, duplicating the placement on each subsequent removal and replacement of the battery cannot be ensured. The battery comprises 26% of the flexible MAV's mass and 23% of the rigid MAV's mass. A measurement of the possible range of battery movement inside the MAV revealed approximately ± ¼ ″ in the x-axis and approximately ± ⅛″ in the z-axis. See Appendix E for the quantification of the errors associated with varying the battery placement inside each MAV.

At a tunnel speed of 50 mph, the registered normal force on sensor N_1 approached its maximum load capacity of 8 lb_f. As the angle of attack was increased, the N_1 sensor neared 8 lb_f, limiting the 50 mph test to an angle of attack no greater than 7.5°. Inaccuracies in the measurement of right and left elevon deflections compounded by correlating them to actual radio controller click movements create a source of indeterminate experimental error and uncertainty in the control surface data runs. Determining the RPM speed of the motor propeller were limited by the strobe to an

accuracy of ± 100 RPM. Inconsistent battery power delivered between each run caused hystereisis in the RPM settings. The problems achieving repeatability in the motor power experiments were further exacerbated by trying to correlate controller stick clicks to a specific throttle setting. Careful scrutiny of the raw data and removing spurious data points before processing mitigated some of the data uncertainty.

Variability in the production of the carbon fiber body and attachment of the parachute membrane to the wing introduce slight vehicle-to-vehicle variations in the aerodynamic response of the control surfaces and the aeroelastic effects of the flexible wings. The mounting block used to attach the MAV to the measurement block was constructed to represent the surveillance camera pod. The dimensions, geometry, and weight are not exactly replicated; therefore, the center of gravity and moments of inertia will differ slightly from the actual MAV, which will result in slight differences in aerodynamic properties from the tested model to the operational model.

V. Conclusions and Recommendations

Conclusions

The intended research goals for this thesis were successfully accomplished. The two top-level goals setout at the beginning of this study were:

- Characterize the flow quality of AFIT's new nominal 3′ x 3′ wind tunnel.
- Measure the performance characteristics of AFRL/MNAV's flexible wing Micro-Air-Vehicle (MAV) and compare them to a geometrically identical rigid wing MAV.

The wind tunnel parameters and flow quality have been measured, analyzed, and reported. The presence of turbulence was used as an indicator of flow quality in the tunnel as a precursor to the MAV flight characterization. The tunnel had an average turbulence intensity of 2.25%. This result is higher than the desired standard; however, there is sufficient evidence suggesting this is inflated attributable to the slotted Plexiglas panel at the top of the tunnel entraining fluid, which was replaced by a solid plate during testing.

The primary benefit of the aeroelastic or deformable flexible wing is its flexibility, which allows the wing to change its shape along the span in reaction to instantaneous local flow perturbations. As discussed in Chapter II, this category of small flight machines operate in a troublesome aerodynamic environment. Flexible wing vehicles readily lend themselves to more stable and responsive flight. The first set of tests on each MAV varied the angle of attack at various tunnel velocities to determine the vehicle's lift and drag characteristics. The primary findings are listed below:

- Flexible wings delay the onset of α_{stall}. They exhibit a higher stall angle than the rigid wing MAV. At 30 mph, the flexible wing α_{stall} is nearly two times higher than the rigid wing MAV. This is the same trend reported in the University of Florida's (UF) findings on their 6″ MAV (Waszak and Jenkins, 2001:4).

- The peak L/D for the flexible wing MAV was higher than the rigid wing MAV at every tunnel velocity.

- At 10 mph, the flex wing lift line is above the rigid wing lift line and decreases with increasing velocity. At 30 mph, the trend reverses, and the rigid wing lift line is above the flex wing lift line. Figure 45 is a notional plot from a UF briefing of the changes in lift against increasing velocity for geometrically similar flexible and rigid wing MAVs. The plot portrays a general agreement with the results discussed above. At the velocity where the flexible MAV's lift line dips below the rigid wing lift line, aeroelastic effects dominate performance over Reynolds number effects.

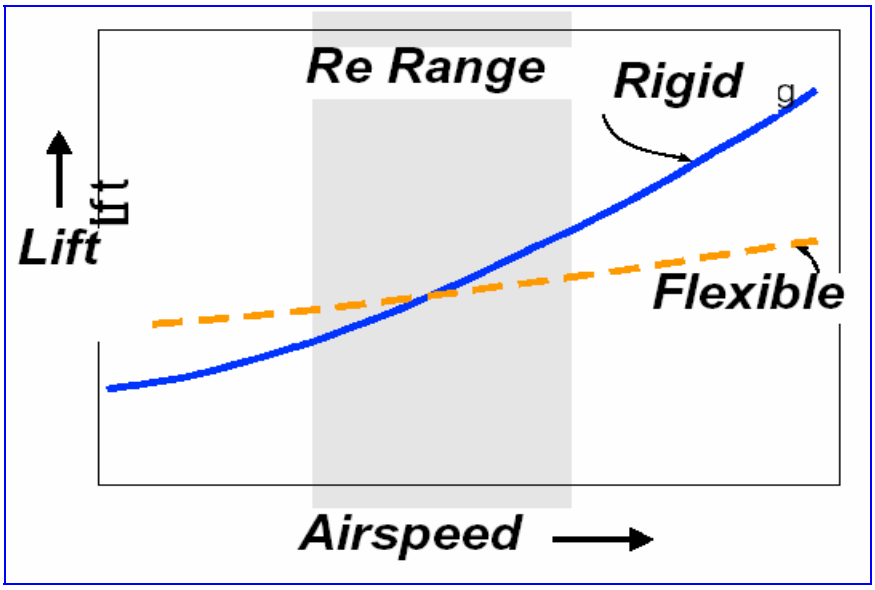

Figure 45. Lift vs. U_∞ for Flex and Rigid Wing MAVs (Nechyba & Ifju, 2002:11)

- At low alpha angles, flex wings behave like rigid wings with similar values of C_L.
- The lift curve slope of the rigid wing is within 2% of the predicted value. The flexible wing lift slope is within 3.5% of the predicted value; wing deformation causes the flexible wing MAV to vary slightly more. The close proximity to the predicted value is a true indicator of the validity of the lift data.

- The zero lift angles are consistent for both MAVs, $\alpha_{LO} \approx 6.7°$, which generally agrees with UF value for α_{LO} (Waszak and Jenkins, 2001:4).

- As the tunnel velocity increases, the rigid wing MAV has higher drag than the flexible wing MAV. The ability of the flexible wing MAV to deform under load may lead to a decrease in the profile drag caused by the shape of the wing in the airflow.

The static stability in the pitch, roll, and yaw axes of each MAV was calculated from the sideslip test runs. Longitudinal stability, $C_{m\alpha}$, is defined as a negative pitching moment slope around the y-axis: $\partial C_m / \partial \alpha < 0$. Directional stability, $C_{n\beta}$, is defined as a positive yaw moment around the z-axis: $\partial C_n / \partial \beta > 0$. Finally, roll stability, $C_{\ell\beta}$, is defined as a negative roll moment about the x-axis: $\partial C_\ell / \partial \beta < 0$. There was considerable variation in the static stability properties of the two MAVs. Their results are listed below:

- The flexible wing MAV is statically stable in all three axes.
- The flexible wing MAV can be trimmed at positive angles of attack.
- The flexible wing MAV will always point into the relative wind.
- In the flexible wing MAV, $C_{m\alpha}$ is about an order of magnitude higher than $C_{\ell\beta}$ and $C_{n\beta}$.

- The rigid wing MAV is not longitudinally stable and exhibited oscillatory behavior. This is potentially an affect of the CG shifting rearward.

- The rigid wing MAV is not directionally stable.
- The rigid wing MAV is marginally stable in roll.
- A definitive relationship exists between the magnitude of the roll and yaw moment coefficients and the angle of attack.

The flexible wing stability derivatives showed good agreement with the stability derivatives from the UF study on their 6″ flexible wing MAV (Waszak and Jenkins, 2001:5). The combination of battery placement and the added weight of the solid carbon fiber wings over the leaner membrane wings could be the cause of stability derivative differences between the flexible and rigid wing MAVs.

The MAVs have only two control surfaces, a right and left elevon, angled |45°| when measured from a vertical plane cut through the center of the tail boom. The elevons assume all control responsibility for the MAVs in each of the three orthogonal axes. A single deflected elevon primarily resulted in changes to the vehicle's pitch and to a lesser degree, the vehicle's nose orientation. The following summary categorizes the effect of a single elevon deflection:

- A single deflected elevon resulted in much higher changes in the pitch moment than in the roll and yaw moments.
    - C_{m} is 86% greater than C_{ℓ} with a single deflected elevon
    - C_{m} is 50% greater than C_{n} with a single deflected elevon
- The pitch and roll moments showed dependency on the angle of attack and were slightly asymmetric in their distribution.
- The single elevon roll moment slope is 2.4 times greater than the tandem elevon roll moment slope.
- The single elevon yaw moment slope is 2.9 times greater than the tandem elevon yaw moment slope.
- The yaw moment showed good symmetry and independence from the angle of attack.
- All three moment plots displayed a slight *bump* after $\delta_{Elevon} = \pm 10°$.

Elevons deflected in tandem result in a large attitude displacement about the pitch axis. Tandem elevon deflections resulted in changes to the vehicle's angle of attack as well as its altitude. Ideally, tandem elevon deflections would only change the vehicle's pitch, while the roll and yaw moments would show negligible affects. The following summary categorizes the effect of tandem elevon deflections:

- The tandem elevon pitching moment slope is 1.5 times greater than the single elevon pitching moment slope (or an increase of 52%) due to the doubling of the surface area deflected in the flow field.
- The roll and yaw moments experienced sign reversals in their slope after $\delta_{Elevon} = \pm 10°$. This resulted in a well-defined control region at $-10° \leq \delta_e \leq +10°$. AFRL/MNAV engineers also confirmed the presence of this behavior in autopilot flight tests at Eglin Air Force Base, Florida.
- Tandem deflected elevons resulted in much higher changes in the pitch moment than in the roll and yaw moments.
    - C_m is 96% greater than C_ℓ with tandem deflected elevons
    - C_m is 89% greater than C_n with tandem deflected elevons
- The pitch and roll moments showed dependency on the angle of attack and were slightly asymmetric in their distribution.

Elevons deflected in opposition serve as a combined aileron and rudder control surface input. Opposed elevon deflection results in heading and direction changes, the primary method used to turn the MAV. In perfectly constructed elevons, opposed deflection would only change the roll and yaw moments while the positive and negative pitching moments should ostensibly cancel one another. The following summary categorizes the effect of opposing elevon deflections:

- At $\delta_e = 10º$, the opposed elevon pitching moment is 25% less than the single elevon pitching moment.

- The pitching moment experienced a sign reversal in its slope after $\delta_{Elevon} = \pm 10°$.

- Opposed deflected elevons resulted in much higher changes in the yaw moment than in the pitch and roll moments.

    - C_n is 72% greater than C_m with opposed deflected elevons
    - C_n is 71% greater than C_ℓ with opposed deflected elevons

- The magnitude of the pitch and roll moments were dependent on the angle of attack, while the yaw moment was independent of the angle of attack.

- The rate of change of the yaw moment was 73% greater than the rate of change of the roll moment (0.007 per $°\delta_e$ vs. 0.0019 per $°\delta_e$) resulting in turns dominated by the yawing rate.

- Opposed elevon roll moment slope is 1.75 times greater than the single elevon roll moment slope.

- Opposed elevon yaw moment slope is 1.7 times greater than the single elevon yaw moment slope.

The motor-on power runs were the last tests performed in this experiment. The motor generated consistent and predictable thrust. The thrust increased commensurately with increasing RPM. The power numbers are somewhat less reliable attributable to torque changes that were on order of the balance resolution and excessive *windmilling* of the prop, creating a component of torque, which did not result from the motor action.

- At $\alpha = 4°$, the MAV will overcome a 10 mph headwind at ⅜ throttle (7500 RPM).
- At $\alpha = 0°$, the MAV will overcome a 20 mph headwind at ⅜ throttle (8000 RPM).
- At $\alpha = 4°$ & 8°, the MAV will overcome a 20 mph headwind at ½ throttle (10,500 RPM).

- At $\alpha = 0°$ & 4°, the MAV will overcome a 30 mph headwind at ½ throttle (10,500 RPM).

- At $\alpha = 8°$, the MAV will overcome a 30 mph headwind at ⅝ throttle (12,700 RPM).

Recommendations

A good first approach to the quantitative assessment of the flight performance of a flexible Micro-Air-Vehicle was accomplished using AFIT's new low-speed wind tunnel. Although, not an exhaustive analysis, this study should provide future research candidates a comparative basis for what is certain to be expanded investigation into this highly visible and promising area of aerodynamic research. Further research funded by AFRL/MNAV or AFRL/VA should keep the following recommendations in focus when defining future projects:

- Explore the 10 mph flight region with an appropriately ranged balance.
- Examine the aeroelastic phenomenon, flutter, and vibration of the flexible wings as a separate thesis.
- With future MAVs using a preprogrammed auto-pilot function instead of an RC control device to navigate the MAV, more emphasis should be placed on flight stability and control as an area of separate research.
- Experiments varying the thickness of the mesh material and the percent it comprises of the mean chord should be investigated to develop an optimal combination of endurance, loiter time, and max lifting weight.
- Basic research into the phenomenon of flexible low Reynolds number airfoils should be dedicated to aid in understanding the laminar separation bubble encountered in the MAV's operating regime.
- A comprehensive full six degree-of-freedom dynamic Computational Fluid Dynamics (CFD) model should be developed to accompany any future wind tunnel testing of flexible wing MAVs.
- Design a fixed battery compartment to prevent arbitrary movement of the CG.

Appendix A: Additional C_L and C_D Data Plots

Figure 46 is the flexible and rigid wing MAV polar plots (C_L vs. C_D).

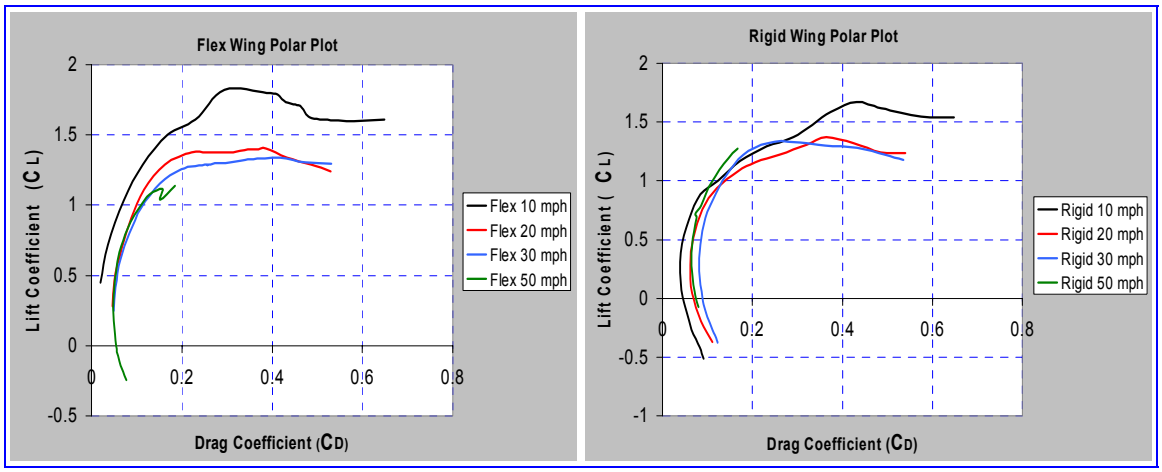

Figure 46. Flexible and Rigid C_L vs. C_D

Figure 47 presents the flexible wing single elevon deflection polar plot.

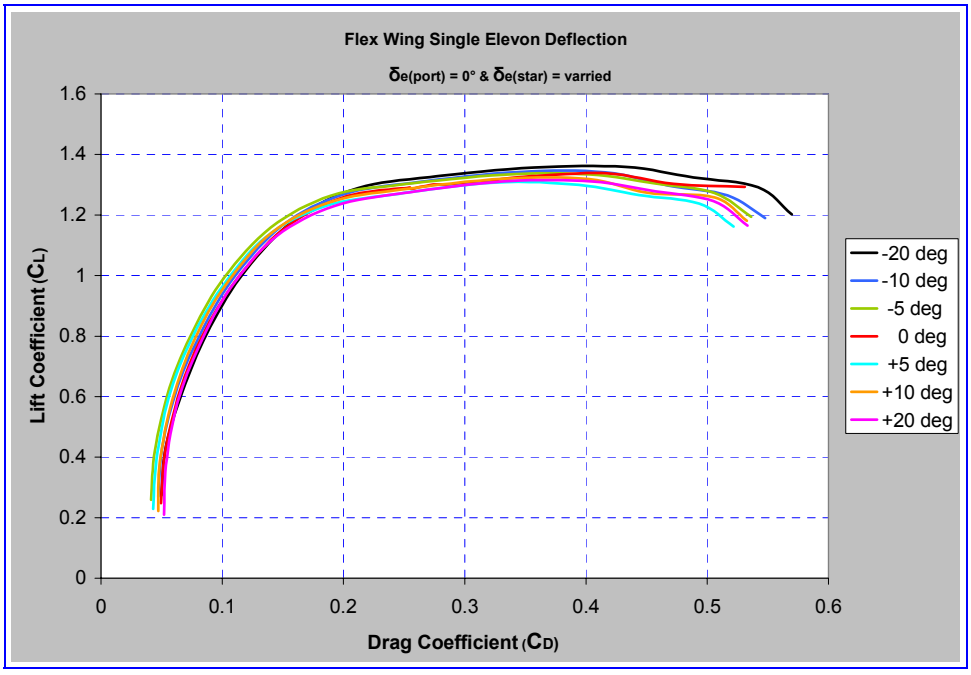

Figure 47. Flexible Wing Single Elevon C_L vs. C_D

Figure 48 presents the flexible wing tandem elevon deflection polar plot.

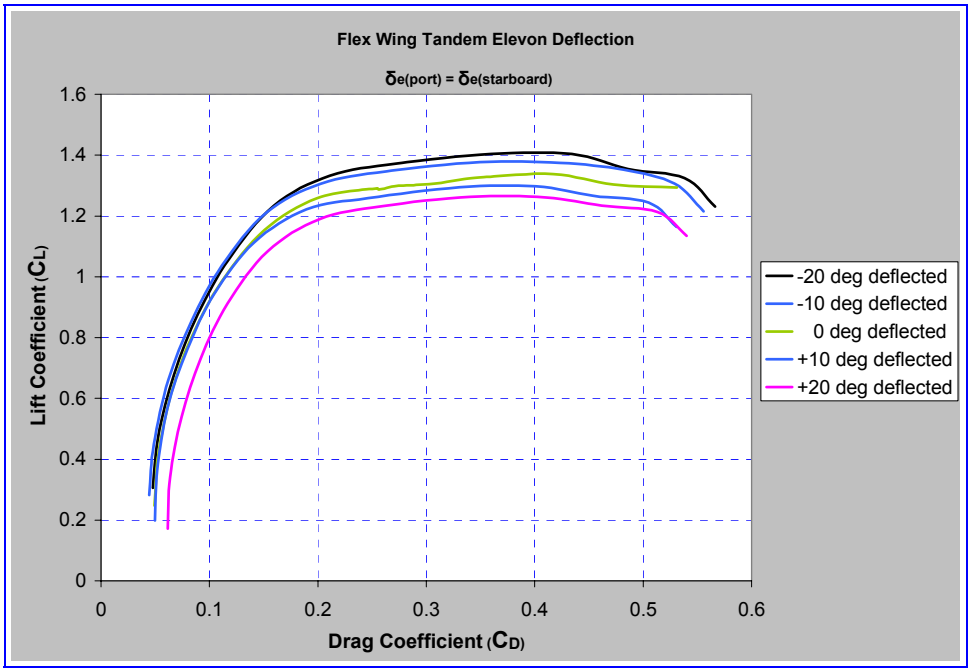

Figure 48. Flexible Wing Tandem Elevon C_L vs. C_D

Figure 49 show both lift and drag versus angle of attack for both MAVs.

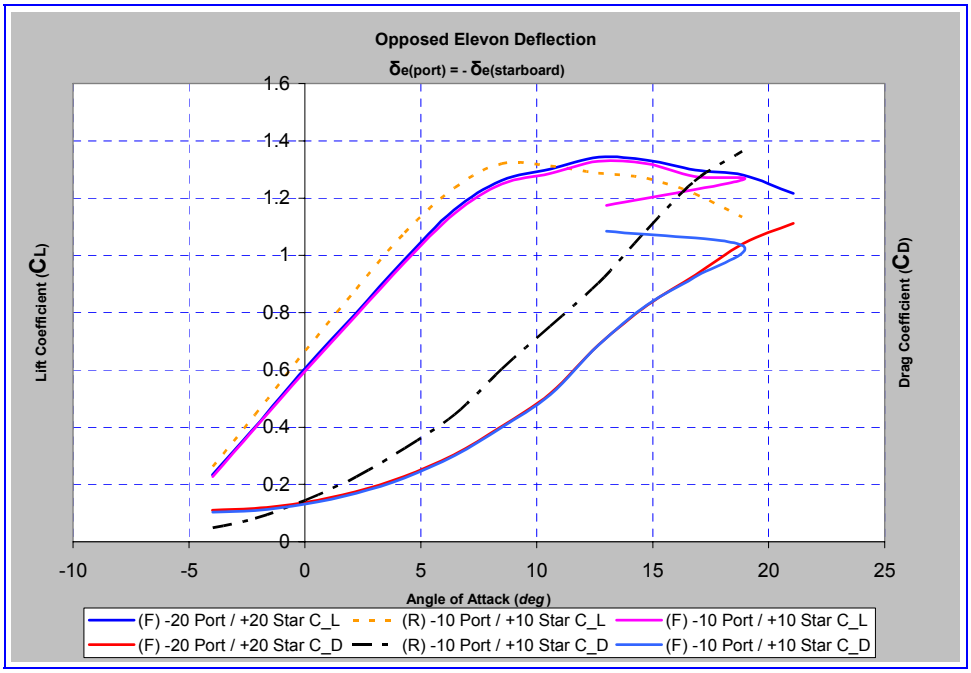

Figure 49. Flexible and Rigid C_L & C_D vs. α

Appendix B: Hot Wire Plots

Figure 50 shows the velocity Contour plots for slot #4.

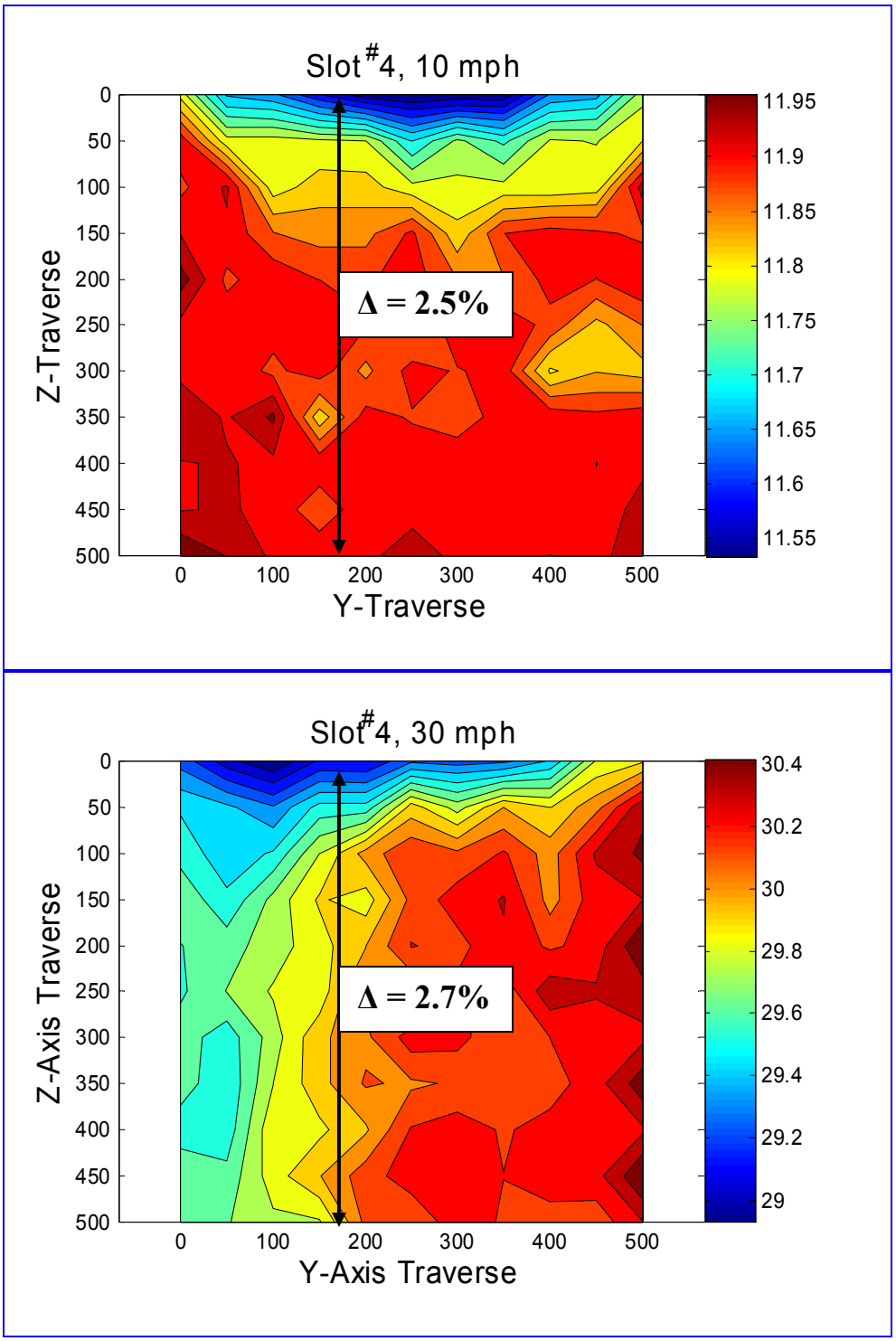

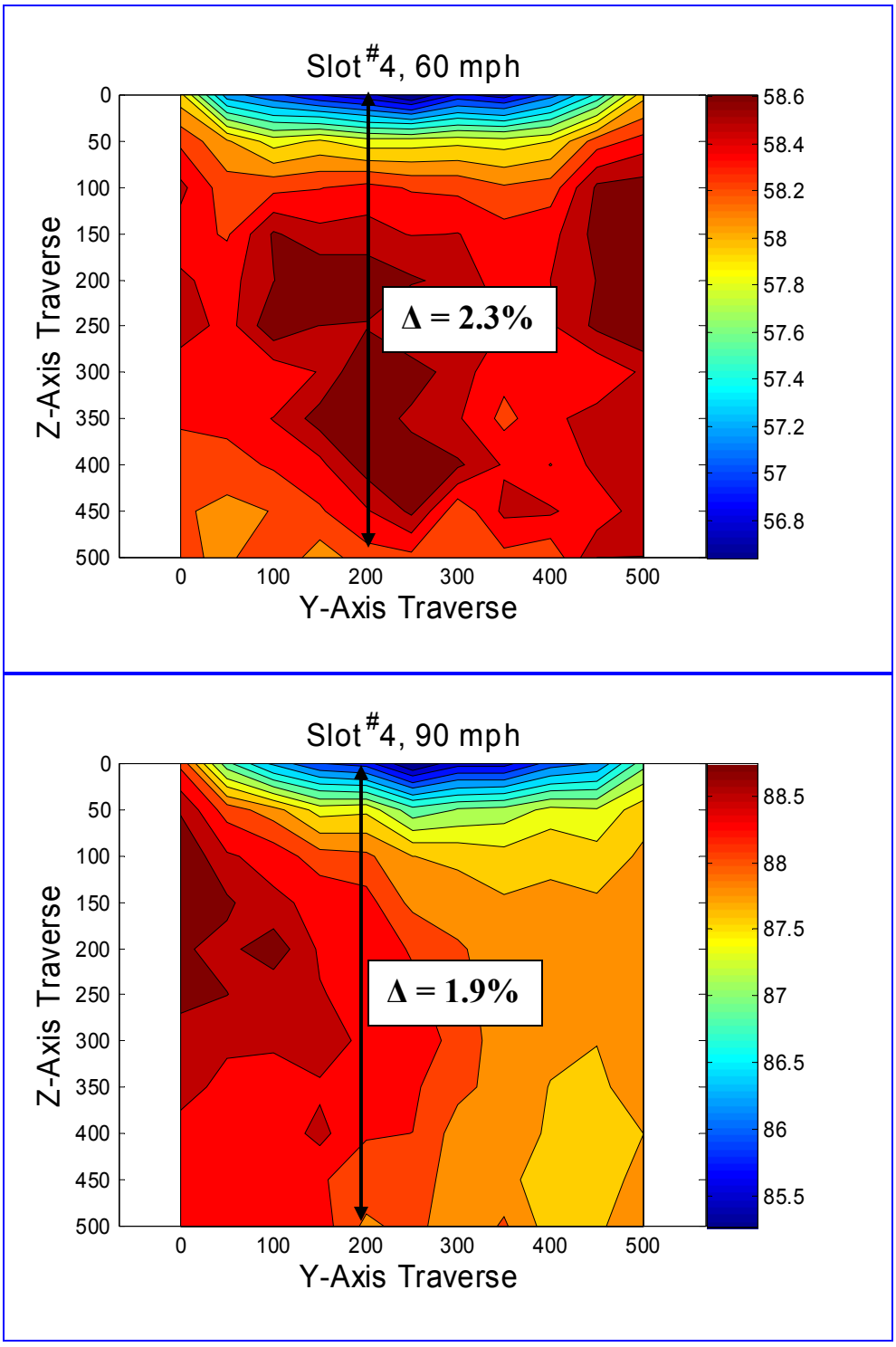

Figure 50. Slot #4 U_{Mean} Velocity Contour Plot

Figure 51 shows the velocity Contour plots for slot #6.

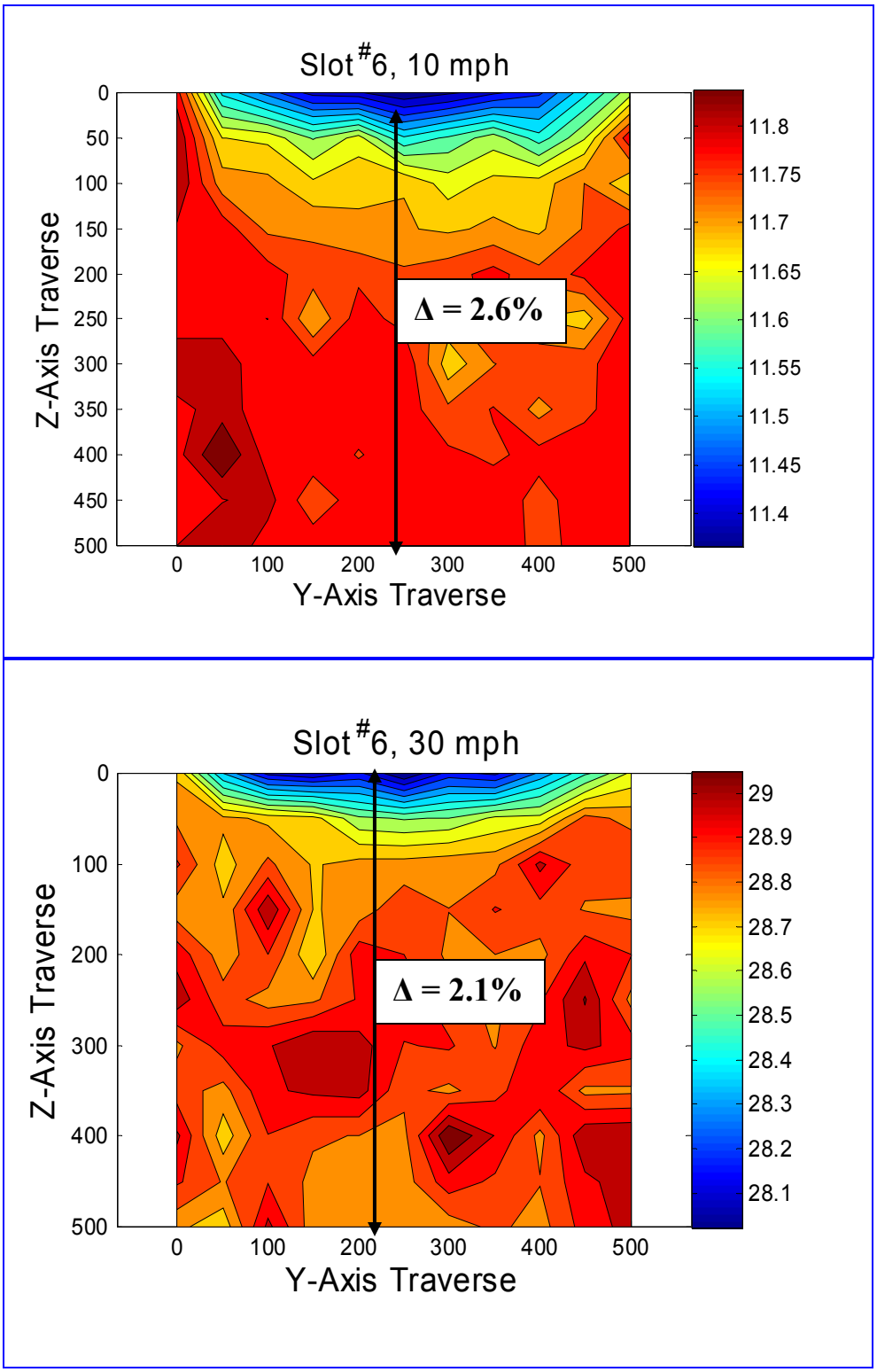

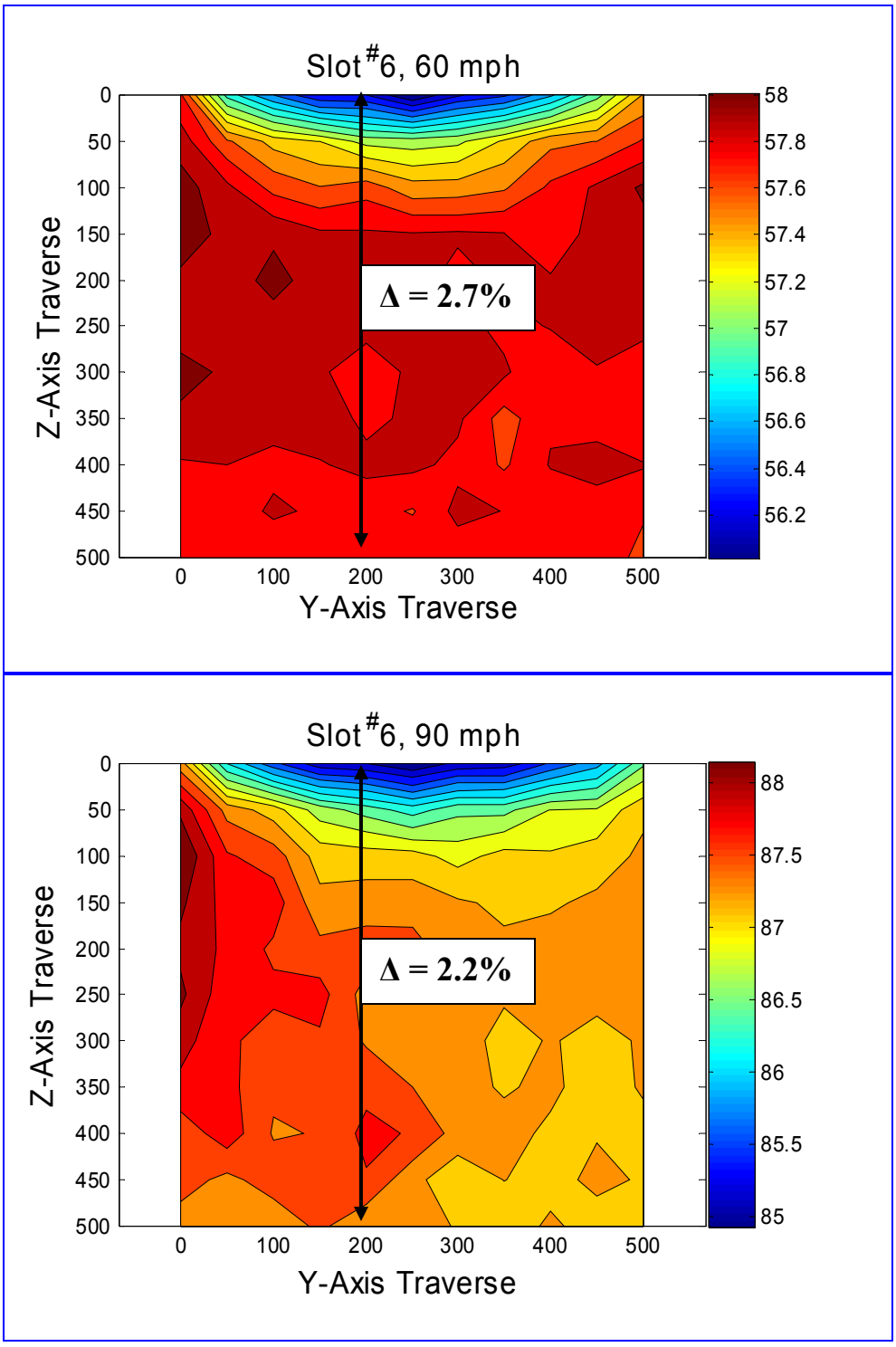

Figure 51. Slot #6 U_{Mean} Velocity Contour Plots

Appendix C: MAV Pictures

Figure 52 and Figure 53 depict the rigid and flexible wing MAV in the tunnel with the propeller off.

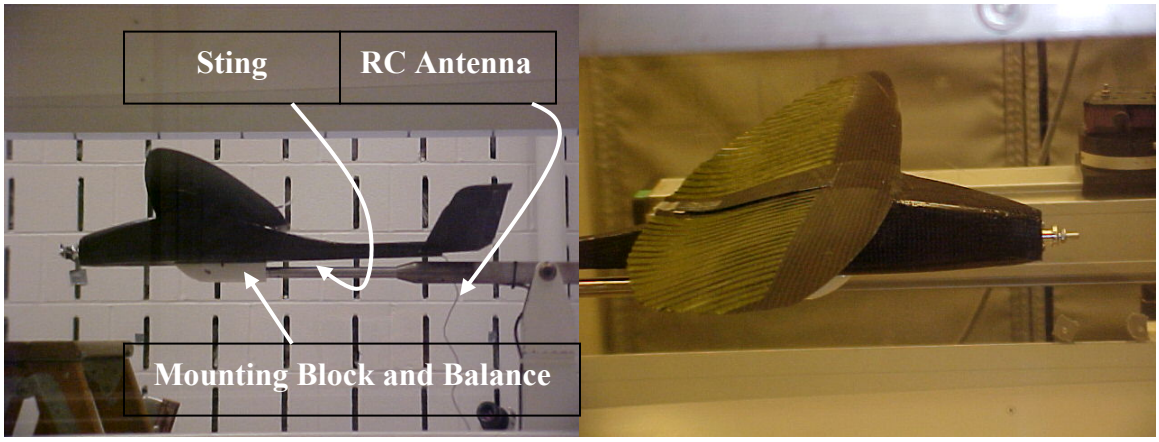

Figure 52. Rigid and Flexible Wing MAV Mounted in the Tunnel

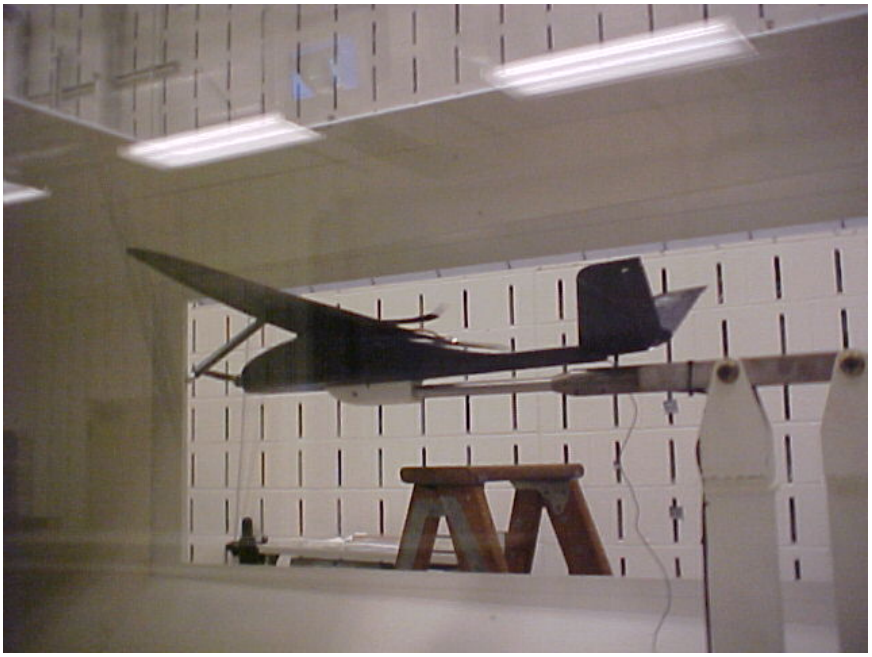

Figure 53. Rigid Wing MAV in Tunnel

Figure 54 shows close-ups of the MAV tail in and out of the tunnel.

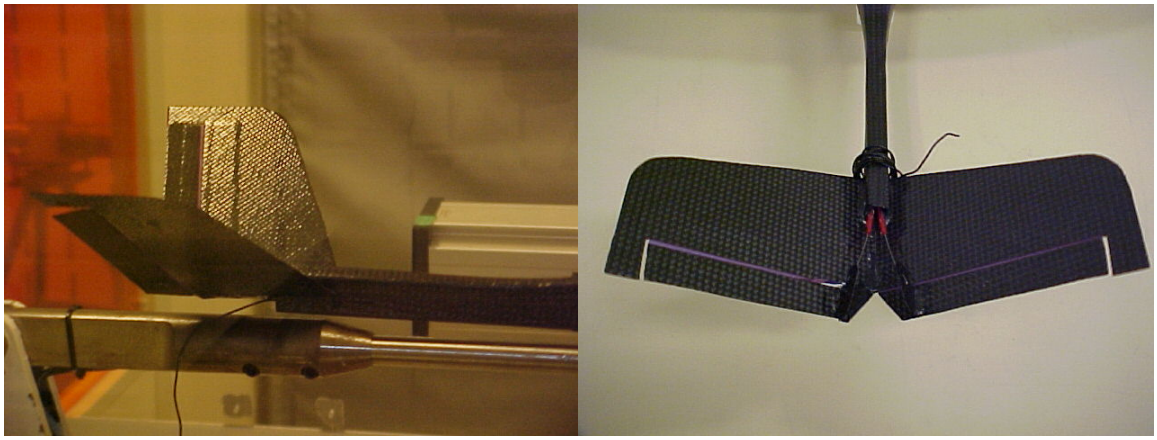

Figure 54. Pictures of the MAV Tail

Figure 55 shows a single elevon deflected in the negative direction.

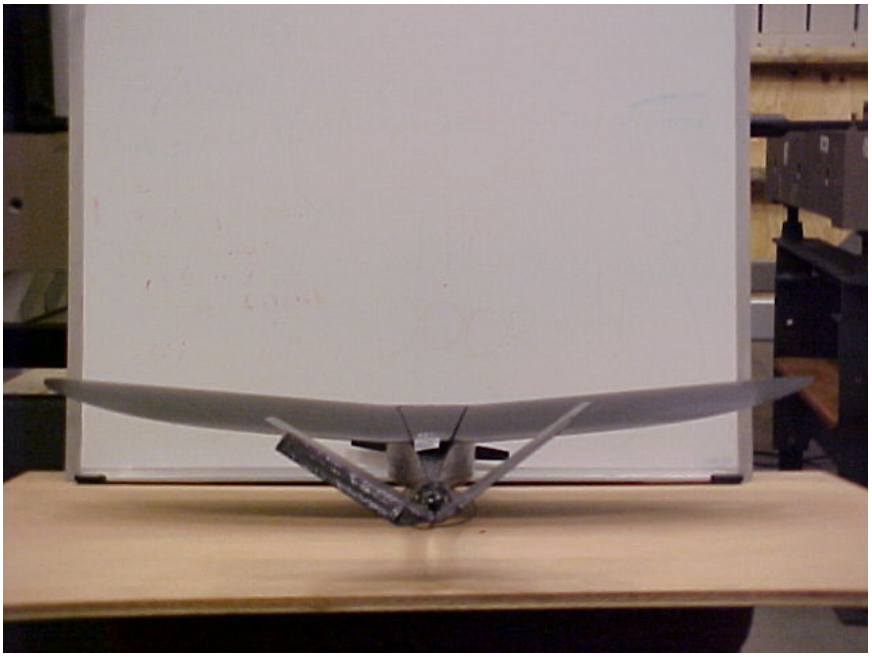

Figure 55. Negative Single Elevon Deflection

Figure 56 presents both elevons deflected in the negative direction.

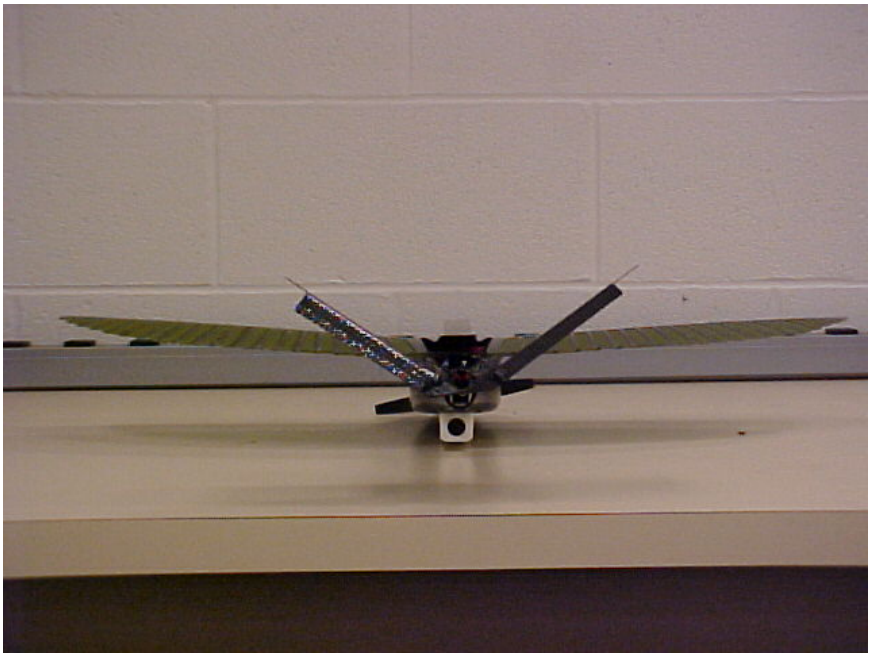

Figure 56. Negative Tandem Tail Deflection

Figure 57 presents both elevons deflected in the positive direction.

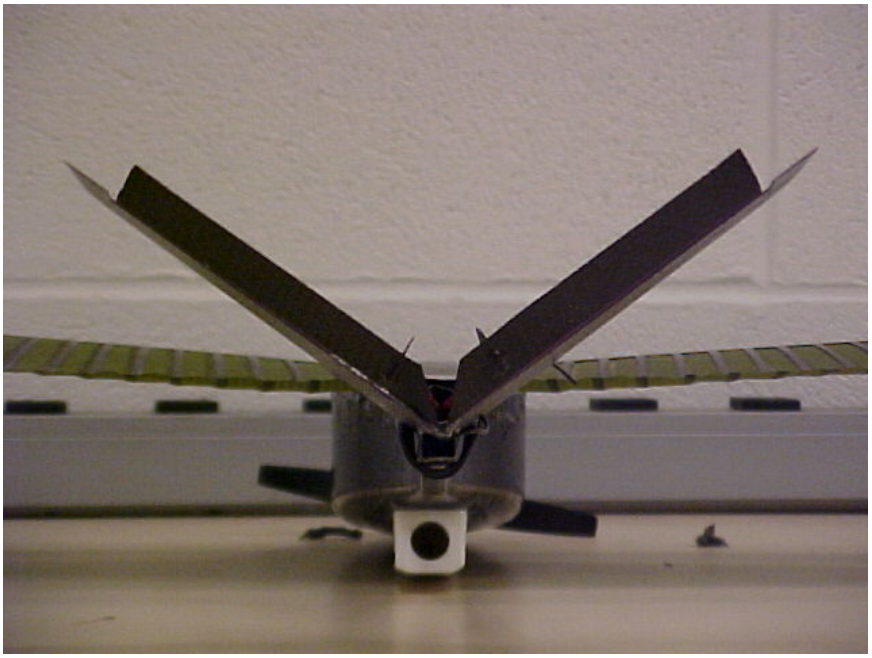

Figure 57. Positive Tandem Tail Deflection

Finally, Figure 58 shows the elevons deflected in opposition.

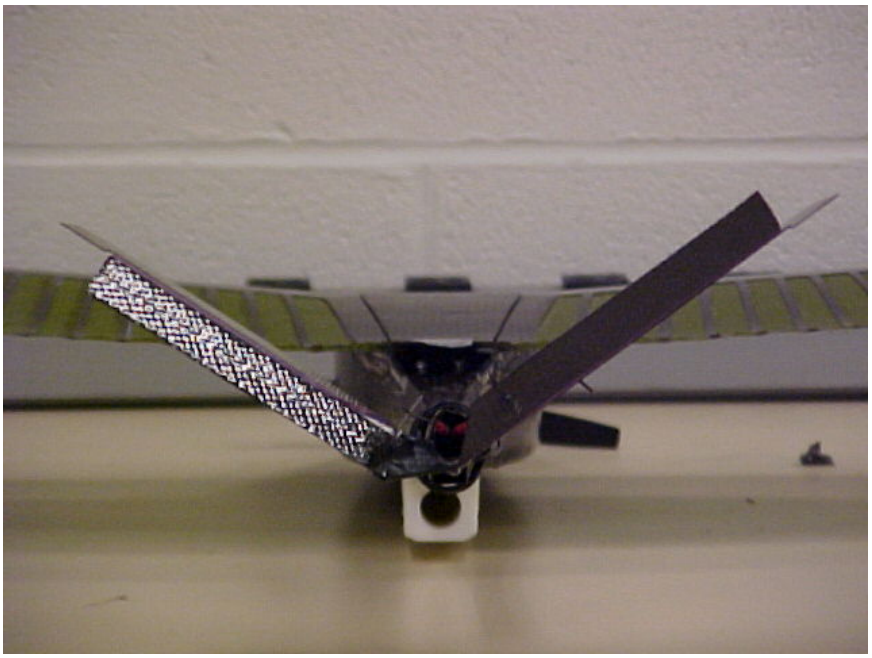

Figure 58. Opposed Elevon Tail Deflection

Appendix D: Data Tables

Alpha Sweeps

Table 23. Flex Wing 10 mph Alpha Sweeps (β = 0°)

Mach #	Rex	qcorrected	U∞	αcorrected	CL	CD_correct	CY	L/D	Cℓ_cg_w	Cm_cg_c_w	Cn_cg_w
0.013186	44854.000	0.24768	10.121	-3.8881	0.45005	0.020068	0.02185	22.426251	0.024943	0.090396	-0.0083552
0.013253	45082.000	0.2502	10.172	-2.0294	0.72087	0.036812	0.02577	19.582473	0.011037	0.081553	-0.0097429
0.013234	45017.000	0.24948	10.157	0.1953	1.0326	0.071617	0.034835	14.418364	-0.00052774	0.070502	-0.01172
0.01321	44938.000	0.2486	10.14	2.3947	1.2869	0.11315	0.041245	11.373398	-0.0020294	0.054156	-0.0098387
0.013254	45088.000	0.25026	10.173	4.4899	1.5024	0.16746	0.043683	8.9716947	-0.013051	0.005613	-0.011803
0.013254	45084.000	0.25023	10.173	6.6252	1.6118	0.22967	0.059486	7.0178952	0.044974	-0.073362	-0.0018047
0.013245	45054.000	0.24989	10.166	8.7189	1.8237	0.29363	0.045472	6.2108776	-0.0493	-0.060685	-0.0081839
0.013192	44876.000	0.24792	10.126	10.882	1.7988	0.38811	0.037944	4.6347685	-0.079048	-0.18416	-0.0079385
0.013214	44950.000	0.24874	10.142	11.313	1.789	0.41125	0.041364	4.350152	-0.068605	-0.2096	-0.0081718
0.013257	45095.000	0.25034	10.175	11.902	1.7473	0.42593	0.042166	4.1023173	-0.06524	-0.24275	-0.0045351
0.013256	45093.000	0.25032	10.175	12.325	1.7201	0.44676	0.046827	3.8501656	-0.036435	-0.27442	-0.012446
0.013272	45147.000	0.25092	10.187	12.841	1.7069	0.46297	0.048338	3.686848	-0.038575	-0.30936	-0.0095038
0.013229	45001.000	0.2493	10.154	13.338	1.6487	0.47525	0.036446	3.4691215	-0.093921	-0.40296	-0.00059823
0.013269	45138.000	0.25082	10.185	13.846	1.6192	0.48755	0.038417	3.3210953	-0.085282	-0.44813	-0.0037151
0.013241	45043.000	0.24977	10.163	14.884	1.6076	0.51552	0.039953	3.1184047	-0.07275	-0.52331	-0.0050168
0.013228	44998.000	0.24927	10.153	16.968	1.5992	0.58107	0.039732	2.7521641	-0.054031	-0.59949	-0.00040207
0.013236	45026.000	0.24958	10.16	19.06	1.6122	0.64882	0.040797	2.4848186	-0.057199	-0.62618	0.0094021

Table 24. Flex Wing 20 mph Alpha Sweeps (β = 0°)

Mach #	Rex	qcorrected	U∞	αcorrected	CL	CD_correct	CY	L/D	Cℓ_cg_w	Cm_cg_c_w	Cn_cg_w
0.02517	85621.000	0.9025	19.319	-3.9639	0.27858	0.046059	0.012481	6.0483293	0.016999	0.082909	-0.0035152
0.025182	85663.000	0.90337	19.329	-2.1415	0.4673	0.050307	0.01564	9.2889658	0.010002	0.083635	-0.0035694
0.025188	85683.000	0.90379	19.333	0.13414	0.6973	0.066991	0.019606	10.408861	0.00254	0.074778	-0.0032097
0.025158	85580.000	0.90162	19.31	2.2271	0.90767	0.088037	0.024389	10.310097	-0.0012845	0.080861	-0.0034634
0.025139	85515.000	0.90025	19.295	4.403	1.1089	0.11613	0.025105	9.5487815	-0.0093073	0.070722	-0.0056396
0.025161	85590.000	0.90184	19.312	6.4825	1.2888	0.16287	0.024299	7.9130595	-0.019929	0.027098	-0.0065607
0.025148	85548.000	0.90094	19.303	8.6088	1.3777	0.22173	0.019911	6.2134127	-0.040651	-0.062561	-0.0085796
0.02512	85452.000	0.89894	19.281	9.6509	1.3758	0.25191	0.01782	5.4614743	-0.045526	-0.10827	-0.0071208
0.025128	85478.000	0.89947	19.287	10.085	1.3744	0.2708	0.018437	5.0753323	-0.041944	-0.13413	-0.0071213
0.025135	85503.000	0.90001	19.293	10.695	1.3748	0.29421	0.020315	4.6728527	-0.036039	-0.14935	-0.0091653
0.025139	85516.000	0.90028	19.295	11.131	1.3771	0.31441	0.022719	4.3799497	-0.028388	-0.16743	-0.0099616
0.025115	85435.000	0.89856	19.277	11.748	1.3995	0.34537	0.021796	4.0521759	-0.030434	-0.19454	-0.0086504
0.025142	85527.000	0.9005	19.298	12.183	1.3989	0.36556	0.020306	3.8267316	-0.039032	-0.21175	-0.0043749
0.025114	85429.000	0.89844	19.276	12.707	1.403	0.38634	0.021842	3.6315163	-0.026583	-0.23646	-0.0056351
0.025125	85469.000	0.89929	19.285	14.767	1.3411	0.43316	0.032758	3.0960846	0.017593	-0.33145	-0.012087
0.025094	85362.000	0.89705	19.261	16.832	1.2911	0.48684	0.030237	2.6520007	0.0048507	-0.44263	-0.0061224
0.025036	85165.000	0.8929	19.216	18.895	1.2381	0.53028	0.015627	2.3348043	-0.03768	-0.5107	0.013979

Table 25. Flex Wing 30 mph Alpha Sweeps (β = 0°)

Mach #	Rex	qcorrected	U∞	αcorrected	CL	CD_correct	CY	L/D	Cℓ_cg_w	Cm_cg_c_w	Cn_cg_w
0.038857	132180.000	2.15	29.824	-3.9774	0.24803	0.049396	0.0092787	5.0212568	0.0096253	0.076799	-0.0014086
0.038917	132380.000	2.16	29.871	-2.1648	0.41446	0.052706	0.011026	7.8636208	0.0031446	0.07947	-0.00045549
0.038923	132410.000	2.16	29.875	0.099515	0.61895	0.064917	0.01189	9.5344825	-0.0019842	0.07796	-0.00095429
0.038892	132300.000	2.15	29.851	2.1805	0.80218	0.083647	0.012652	9.590063	-0.0061773	0.06979	-0.00071625
0.038891	132290.000	2.15	29.85	4.3482	0.9848	0.11136	0.012884	8.8433908	-0.011658	0.049414	-0.0002956
0.038909	132360.000	2.16	29.864	6.5098	1.1537	0.15063	0.010411	7.6591648	-0.022023	0.0069824	0.0028559
0.038897	132320.000	2.16	29.855	8.556	1.2582	0.19957	0.0087488	6.3045548	-0.028793	-0.072012	0.0023365
0.038832	132090.000	2.15	29.805	9.8743	1.2905	0.25434	0.0050456	5.0739168	-0.036313	-0.15752	0.00016005
0.038916	132380.000	2.16	29.87	10.133	1.2862	0.25583	0.0041095	5.0275574	-0.039133	-0.1603	-0.00040937
0.038834	132100.000	2.15	29.807	10.661	1.2991	0.27251	0.0030575	4.7671645	-0.043714	-0.18488	0.001224
0.038898	132320.000	2.16	29.856	11.097	1.3006	0.2856	0.0036902	4.5539216	-0.041444	-0.19519	0.0060237
0.038884	132270.000	2.15	29.845	11.707	1.306	0.30825	0.0045063	4.2368208	-0.038117	-0.21013	0.0076439
0.038913	132370.000	2.16	29.867	12.148	1.3191	0.3303	0.0063363	3.9936421	-0.03104	-0.22254	0.0045032
0.038917	132380.000	2.16	29.871	12.674	1.3272	0.35291	0.0049621	3.7607322	-0.035422	-0.2472	0.0038298
0.038862	132200.000	2.15	29.829	14.765	1.3375	0.41704	-0.000799	3.2071264	-0.057166	-0.36961	0.010455
0.038867	132210.000	2.15	29.832	16.837	1.3034	0.4725	-0.001616	2.7585185	-0.053419	-0.46487	0.013424
0.038771	131890.000	2.14	29.758	18.919	1.2928	0.53096	0.0028985	2.434835	-0.030962	-0.50272	0.021821

Table 26. Flex Wing 50 mph Alpha Sweeps (β = 0°)

Mach #	Rex	$q_{corrected}$	U_∞	$\alpha_{corrected}$	C_L	$C_{D\_correct}$	C_Y	L/D	$C_{\ell\_cg\_w}$	$C_{m\_cg\_c\_w}$	$C_{n\_cg\_w}$
0.065724	223570.000	6.1534	50.446	-10.457	-0.24722	0.07692	0.0021465	-3.213989	0.012878	0.12299	0.0054658
0.065742	223630.000	6.1569	50.46	-9.385	-0.18329	0.069405	0.002835	-2.640876	0.01257	0.106	0.0043969
0.065699	223490.000	6.1489	50.427	-8.6715	-0.14147	0.065129	0.0030101	-2.172151	0.012436	0.095973	0.0039383
0.065692	223460.000	6.1475	50.422	-7.5974	-0.073416	0.059309	0.0024618	-1.237856	0.010625	0.080265	0.001964
0.065693	223470.000	6.1477	50.422	-6.4415	-0.000595	0.054618	0.0031117	-0.010899	0.010689	0.067473	0.0019468
0.065673	223400.000	6.1439	50.407	-4.2704	0.17553	0.048891	0.0068645	3.5902313	0.0071684	0.055586	0.002339
0.065676	223410.000	6.1445	50.409	-2.185	0.36875	0.048729	0.0086671	7.5673624	-4.92E-05	0.052215	0.0028503
0.065704	223500.000	6.1497	50.431	-0.010014	0.56797	0.055837	0.0088191	10.171929	-0.010209	0.049091	0.0027509
0.065656	223340.000	6.1408	50.394	1.0763	0.66366	0.062067	0.0082462	10.692639	-0.016101	0.044783	0.0027473
0.065661	223360.000	6.1418	50.398	2.1574	0.74985	0.070318	0.0077439	10.663699	-0.021172	0.037352	0.00286
0.065652	223330.000	6.1401	50.391	3.1517	0.83443	0.079618	0.0071312	10.480419	-0.026259	0.027445	0.0033958
0.065608	223180.000	6.1319	50.357	4.2375	0.93126	0.094858	0.023704	9.8174113	-0.0087961	0.016493	-0.0001745
0.065576	223070.000	6.1257	50.332	5.3632	1.0111	0.11154	0.030651	9.0649094	-0.010347	-0.0023326	-0.0010331
0.065598	223150.000	6.13	50.35	6.3895	1.0784	0.12841	0.035462	8.3980998	-0.016219	-0.0264	-0.0023856
0.0656	223150.000	6.1303	50.351	7.4492	1.1138	0.15665	0.069127	7.1101181	-0.024761	-0.053252	-0.020173
0.064938	220900.000	6.0072	49.843	7.6755	1.0376	0.15293	0.060999	6.7848035	-0.025498	-0.060099	-0.021706
0.065589	223110.000	6.1282	50.342	8.4863	1.1397	0.18459	0.068911	6.174224	-0.051986	-0.091324	-0.025161

Table 27. Rigid Wing 10 mph Alpha Sweeps (β = 0°)

Mach #	Rex	$q_{corrected}$	U_∞	$\alpha_{corrected}$	C_L	$C_{D\_correct}$	C_Y	L/D	$C_{\ell\_cg\_w}$	$C_{m\_cg\_c\_w}$	$C_{n\_cg\_w}$
0.01344	45720.000	0.25731	10.315	-10.574	-0.51225	0.09186	0.063396	-5.576421	0.31301	-0.0012714	0.0037796
0.013516	45981.000	0.26026	10.374	-9.8356	-0.41553	0.082722	0.064491	-5.02321	0.28913	-0.0019374	0.0084231
0.013485	45874.000	0.25904	10.35	-8.7262	-0.2653	0.064774	0.057069	-4.095779	0.26085	-0.0010356	0.010317
0.013467	45813.000	0.25835	10.336	-7.6135	-0.10979	0.053989	0.055929	-2.033562	0.2365	0.0015399	0.011962
0.013492	45897.000	0.2593	10.355	-6.492	0.067939	0.042066	0.044444	1.6150573	0.21108	-0.00035287	0.018918
0.013489	45888.000	0.2592	10.353	-4.1762	0.38887	0.040174	0.029403	9.6796436	0.16703	-0.0034124	0.023914
0.013491	45896.000	0.25929	10.355	-2.0516	0.67084	0.058534	0.023788	11.46069	0.13786	-0.0047682	0.030932
0.013517	45981.000	0.26026	10.374	0.12899	0.88251	0.085038	0.030292	10.377831	0.08116	-0.008664	0.037581
0.013521	45996.000	0.26042	10.377	2.2685	1.0013	0.12408	0.035707	8.0697937	-0.045177	-0.010198	0.040027
0.013524	46007.000	0.26054	10.38	4.3438	1.1718	0.1728	0.037731	6.78125	-0.099266	-0.010813	0.042448
0.013479	45853.000	0.25881	10.345	6.4848	1.294	0.23147	0.018588	5.5903573	-0.18362	-0.010885	0.040991
0.013483	45867.000	0.25896	10.348	8.5187	1.3707	0.29046	-0.0077	4.7190663	-0.24967	-0.0093351	0.037888
0.013516	45979.000	0.26023	10.374	10.7	1.5843	0.3739	0.076987	4.2372292	-0.24334	-0.0065822	0.067356
0.013535	46046.000	0.26099	10.389	12.824	1.6682	0.43188	-0.043938	3.862647	-0.26194	0.0051183	0.042293
0.013567	46153.000	0.26221	10.413	14.89	1.62	0.48626	0.0054412	3.331551	-0.31913	-0.0074021	0.046816
0.0135	45925.000	0.25962	10.361	16.945	1.5484	0.57484	-0.022467	2.6936191	-0.57352	-0.00097986	0.031761
0.013508	45951.000	0.25992	10.367	19.028	1.5392	0.64856	-0.024313	2.3732577	-0.68159	0.010309	0.025469

Table 28. Rigid Wing 20 mph Alpha Sweeps (β = 0°)

Mach #	Rex	$q_{corrected}$	U_∞	$\alpha_{corrected}$	C_L	$C_{D\_correct}$	C_Y	L/D	$C_{\ell\_cg\_w}$	$C_{m\_cg\_c\_w}$	$C_{n\_cg\_w}$
0.025202	85733.000	0.90476	19.343	-10.513	-0.37444	0.11108	0.043843	-3.370904	0.23022	0.00055723	-0.00098777
0.025222	85801.000	0.90619	19.358	-8.6959	-0.19658	0.085359	0.03435	-2.302979	0.19742	0.00067767	0.0039627
0.025268	85957.000	0.9095	19.393	-6.4387	0.044087	0.065638	0.025855	0.6716689	0.16512	0.00049842	0.01245
0.025203	85738.000	0.90488	19.344	-4.2237	0.28131	0.062373	0.01521	4.5101246	0.14067	-0.0013607	0.016523
0.025207	85752.000	0.90517	19.347	-2.121	0.51368	0.069044	0.011396	7.4398934	0.12905	-0.00073273	0.02377
0.025205	85745.000	0.90501	19.345	0.072313	0.75427	0.088182	0.0077198	8.5535597	1.09E-01	0.00095645	0.033437
0.025223	85806.000	0.9063	19.359	2.2392	0.93509	0.12143	0.028922	7.7006506	0.068263	0.0075594	0.044006
0.025231	85831.000	0.90683	19.365	4.2683	1.0795	0.16759	0.046722	6.4413151	-0.0064993	0.0091919	0.051132
0.025196	85715.000	0.90438	19.338	6.4244	1.1572	0.20736	0.11076	5.5806327	-0.058263	0.016575	0.063522
0.025173	85634.000	0.90267	19.32	8.4528	1.2215	0.25963	0.09173	4.7047722	-0.12602	0.0025753	0.064683
0.025181	85663.000	0.90328	19.327	10.578	1.3081	0.32093	0.025887	4.0759667	-0.17319	0.0028754	0.052659
0.02519	85693.000	0.90392	19.333	12.692	1.3702	0.36453	-0.052079	3.7588127	-0.17731	-0.0088841	0.02695
0.025218	85789.000	0.90594	19.355	14.757	1.3198	0.42482	-0.018429	3.1067276	-0.27745	0.00027263	0.032345
0.025189	85690.000	0.90386	19.333	16.81	1.2434	0.48477	-0.017416	2.5649277	-0.44449	-0.0014506	0.025635
0.025087	85343.000	0.89655	19.254	18.895	1.2373	0.54017	-0.026875	2.2905752	-0.55223	0.0096118	0.019662

Table 29. Rigid Wing 30 mph Alpha Sweeps (β = 0°)

Mach #	Rex	$q_{corrected}$	U_∞	$\alpha_{corrected}$	C_L	$C_{D\_correct}$	C_Y	L/D	$C_{\ell\_cg\_w}$	$C_{m\_cg\_c\_w}$	$C_{n\_cg\_w}$
0.038907	132360.000	2.1564	29.861	-10.514	-0.37655	0.12221	0.03907	-3.081172	0.22946	0.002434	-0.0073901
0.038898	132330.000	2.1554	29.855	-10.333	-0.36085	0.1215	0.041726	-2.969959	0.2267	0.0029937	-0.0069664
0.038929	132430.000	2.1588	29.878	-9.7897	-0.31167	0.11611	0.041246	-2.684265	0.21517	0.0030739	-0.0060627
0.038929	132430.000	2.1588	29.878	-8.7021	-0.21076	0.10483	0.039594	-2.010493	0.19496	0.004417	-0.0018234
0.038917	132390.000	2.1575	29.869	-7.6105	-0.10291	0.095314	0.034656	-1.079694	0.17895	0.0046241	0.0014948
0.038912	132370.000	2.157	29.865	-6.5052	0.012283	0.08831	0.030739	0.1390896	0.16411	0.0047774	0.0049632
0.038903	132340.000	2.156	29.859	-4.2456	0.23182	0.081018	0.020841	2.8613395	0.14073	0.0026946	0.0090311
0.038907	132360.000	2.1564	29.861	-2.146	0.45718	0.083986	0.015774	5.4435263	0.13209	0.0025963	0.016534
0.03892	132400.000	2.1578	29.871	0.041012	0.68344	0.096003	0.0080474	7.1189442	0.12086	0.0019885	0.024467
0.038885	132280.000	2.1539	29.844	2.2223	0.89687	0.11908	0.002902	7.5316594	0.097724	0.00040008	0.031422
0.038868	132220.000	2.1521	29.832	4.3089	1.0927	0.15066	-0.001978	7.2527545	0.063352	-0.0029148	0.037556
0.03889	132300.000	2.1545	29.848	6.4665	1.2525	0.19093	-0.014748	6.5599958	0.012674	-0.011769	0.039928
0.038873	132240.000	2.1526	29.835	8.5026	1.3341	0.25069	-0.044807	5.3217121	-0.074516	-0.009917	0.013555
0.038864	132210.000	2.1517	29.829	10.585	1.3239	0.30613	-0.054151	4.3246333	-0.14248	0.00019668	0.013578
0.038894	132310.000	2.1549	29.851	12.663	1.3028	0.36162	-0.048238	3.6026768	-0.19611	-0.009901	0.015516
0.038866	132220.000	2.1519	29.83	14.741	1.2822	0.43358	-0.022345	2.9572397	-0.27828	-0.0044711	0.022531
0.038795	131980.000	2.144	29.776	16.801	1.2221	0.49531	-0.027441	2.4673437	-0.41716	-0.0012361	0.018321
0.038772	131900.000	2.1415	29.758	18.867	1.174	0.5358	-0.024135	2.1911161	-0.52929	0.0039708	0.015328

Table 30. Rigid Wing 50 mph Alpha Sweeps (β = 0°)

Mach #	Rex	$q_{corrected}$	U_∞	$\alpha_{corrected}$	C_L	$C_{D\_correct}$	C_Y	L/D	$C_{\ell\_cg\_w}$	$C_{m\_cg\_c\_w}$	$C_{n\_cg\_w}$
0.06569	223470.000	6.1471	50.417	-7.2489	-0.072213	0.080524	0.026355	-0.896789	0.15681	0.0029114	0.0052468
0.065702	223510.000	6.1493	50.426	-6.4354	-0.000858	0.075036	0.023693	-0.011437	0.14778	0.0028462	0.0058092
0.065713	223550.000	6.1514	50.435	-5.3415	0.112	0.068807	0.020333	1.6277414	0.13412	0.0022613	0.0069773
0.065705	223520.000	6.1499	50.429	-4.2492	0.22351	0.065712	0.019024	3.4013574	0.12437	0.0026418	0.0097869
0.065692	223480.000	6.1476	50.419	-3.1636	0.33123	0.064789	0.017232	5.1124419	0.11682	0.0022121	0.011655
0.065661	223370.000	6.1418	50.395	-2.1503	0.44727	0.065843	0.015527	6.7929772	0.10909	0.0022557	0.013743
0.065677	223420.000	6.1446	50.407	-0.96614	0.56767	0.070489	0.01111	8.0533133	0.10292	0.0021473	0.015519
0.06568	223430.000	6.1452	50.409	0.12751	0.6823	0.076396	0.0084474	8.9310959	0.091059	0.0010304	0.017758
0.065663	223380.000	6.1421	50.397	0.31651	0.71624	0.073542	0.0081076	9.7391966	0.087757	0.0010471	1.89E-02
0.065647	223320.000	6.1391	50.385	1.2194	0.79057	0.085955	0.0072658	9.1974871	0.075705	0.0008215	0.019677
0.065587	223120.000	6.1279	50.339	2.22	0.89161	0.096621	0.0062082	9.2279111	0.061106	-3.27E-05	0.020711
0.065572	223070.000	6.125	50.327	3.3082	0.99168	0.11018	0.0048938	9.0005446	0.042509	-0.0015821	0.022234
0.065522	222900.000	6.1157	50.288	4.3963	1.0937	0.12673	0.0035055	8.6301586	0.021666	-0.0035988	0.023776
0.065533	222930.000	6.1177	50.297	5.4828	1.1898	0.14569	0.0007916	8.1666552	-0.0029498	-0.006595	0.024876
0.065493	222800.000	6.1102	50.266	6.4767	1.2756	0.16746	-0.004525	7.6173415	-0.035126	-0.0087778	0.025198

Beta Sweeps

Table 31. Flex Wing 30 mph Alpha Sweeps (β = -4°)

Mach #	Rex	$q_{corrected}$	U_∞	$\alpha_{corrected}$	C_L	$C_{D\_correct}$	C_Y	$C_{\ell\_cg\_w}$	$C_{m\_cg\_c\_w}$	$C_{n\_cg\_w}$
0.038871	132230.000	2.1524	29.835	-3.9733	0.2572	0.060076	0.035001	0.040435	0.082164	-0.0021626
0.03888	132260.000	2.1535	29.842	-2.1628	0.41915	0.06405	0.039121	0.029643	0.084517	0.00016717
0.038848	132150.000	2.1499	29.818	0.009708	0.6126	0.076598	0.043086	0.020457	0.082218	0.00012128
0.038847	132140.000	2.1497	29.817	2.1794	0.79974	0.096834	0.045814	0.01161	0.071946	-0.00058707
0.038807	132010.000	2.1454	29.786	4.2569	0.9751	0.12482	0.04677	0.003079	0.046974	-0.0022273
0.038845	132140.000	2.1495	29.815	6.4138	1.1332	0.16326	0.041279	-0.012326	-0.0011468	-0.0034155
0.038874	132240.000	2.1527	29.837	8.4574	1.232	0.21493	0.0321	-0.032429	-0.087321	-0.010908
0.038919	132390.000	2.1577	29.872	10.657	1.2908	0.28258	0.032752	-0.020276	-0.15554	-0.026775
0.038912	132370.000	2.157	29.867	11.095	1.2971	0.30211	0.030741	-0.021168	-0.18343	-0.028251
0.038904	132340.000	2.1561	29.861	11.615	1.2934	0.32238	0.02704	-0.025376	-0.22719	-0.028056
0.038874	132240.000	2.1527	29.837	12.141	1.3041	0.3419	0.026258	-0.023313	-0.25215	-0.028057
0.03886	132190.000	2.1511	29.826	12.662	1.3012	0.35952	0.02332	-0.024932	-0.29078	-0.026171
0.038839	132120.000	2.1489	29.811	13.185	1.3023	0.377	0.022043	-0.024262	-0.3229	-0.025825
0.038853	132170.000	2.1505	29.822	13.705	1.3011	0.39314	0.020611	-0.020307	-0.35125	-0.024692
0.038859	132190.000	2.1511	29.826	14.751	1.3049	0.42607	0.012835	-0.035201	-0.39873	-0.01577
0.038847	132140.000	2.1497	29.816	16.834	1.2958	0.48568	0.0056417	-0.036617	-0.45848	0.0018506
0.038776	131900.000	2.1419	29.762	18.905	1.2606	0.53647	-0.0030634	-0.056623	-0.49721	0.012862

Table 32. Flex Wing 30 mph Alpha Sweeps (β = -8°)

Mach #	Rex	$q_{corrected}$	U_∞	$\alpha_{corrected}$	C_L	$C_{D\_correct}$	C_Y	$C_{\ell\_cg\_w}$	$C_{m\_cg\_c\_w}$	$C_{n\_cg\_w}$
0.038735	131760.000	2.1373	29.731	-3.9704	0.2638	0.058903	0.06585	0.075108	0.092289	-0.012585
0.03878	131920.000	2.1423	29.765	-2.1599	0.42574	0.063547	0.071673	0.05824	0.092435	-0.010106
0.038789	131950.000	2.1434	29.773	0.012511	0.61894	0.075884	0.077585	0.043604	0.087881	-0.0088448
0.038774	131900.000	2.1416	29.761	2.1802	0.80146	0.09442	0.080934	0.031516	0.074403	-0.011216
0.038794	131960.000	2.1438	29.776	4.2567	0.97465	0.12125	0.082055	0.016827	0.045816	-0.013471
0.038838	132110.000	2.1487	29.81	6.4032	1.1093	0.16045	0.077978	-0.0031028	-0.013288	-0.018208
0.038789	131950.000	2.1433	29.772	8.4529	1.2218	0.21855	0.072014	-0.017046	-0.085422	-0.032821
0.038778	131910.000	2.1421	29.764	10.651	1.2838	0.28966	0.061817	-0.024628	-0.20044	-0.051705
0.038787	131940.000	2.1432	29.771	11.091	1.2874	0.30375	0.057153	-0.029382	-0.2295	-0.053765
0.038762	131860.000	2.1404	29.752	11.663	1.2912	0.32064	0.053228	-0.032975	-0.26699	-0.054815
0.038738	131770.000	2.1377	29.733	12.14	1.3004	0.33595	0.052848	-0.026706	-0.28823	-0.055923
0.038738	131770.000	2.1377	29.733	12.665	1.3086	0.35207	0.051549	-0.024788	-0.31359	-0.055584
0.038775	131900.000	2.1418	29.762	13.188	1.3103	0.36749	0.050843	-0.017547	-0.33305	-0.054602
0.038718	131710.000	2.1355	29.718	13.712	1.3169	0.38359	0.050806	-0.011316	-0.35115	-0.053911
0.03872	131710.000	2.1357	29.719	14.757	1.319	0.41198	0.046288	-0.011609	-0.38891	-0.048754
0.038702	131650.000	2.1337	29.705	16.837	1.3027	0.46517	0.034391	-0.015195	-0.44026	-0.029556
0.038636	131430.000	2.1264	29.655	18.898	1.2453	0.50162	0.012302	-0.068574	-0.47905	0.00050466

Table 33. Flex Wing 30 mph Alpha Sweeps (β = -12°)

Mach #	Rex	$q_{corrected}$	U_∞	$\alpha_{corrected}$	C_L	$C_{D\_correct}$	C_Y	$C_{\ell\_cg\_w}$	$C_{m\_cg\_c\_w}$	$C_{n\_cg\_w}$
0.038645	131460.000	2.1275	29.662	-3.9707	0.26321	0.070189	0.099736	0.11216	0.11273	-0.033958
0.03866	131510.000	2.1291	29.673	-2.1627	0.41931	0.075031	0.10641	0.091315	0.11136	-0.031541
0.038655	131490.000	2.1286	29.67	0.006059	0.60434	0.086609	0.11279	0.071183	0.1061	-0.031754
0.038675	131560.000	2.1307	29.685	2.1723	0.78365	0.10535	0.11707	0.055778	0.091029	-0.034819
0.038673	131550.000	2.1305	29.683	4.2437	0.94513	0.13282	0.1171	0.038239	0.055482	-0.038415
0.038678	131570.000	2.1311	29.687	6.3888	1.0767	0.17424	0.11163	0.018123	-0.0020979	-0.045202
0.03865	131480.000	2.128	29.666	8.499	1.1767	0.23961	0.10465	0.010311	-0.095006	-0.066151
0.038665	131530.000	2.1296	29.677	10.629	1.2407	0.30071	0.092485	-0.0047582	-0.20908	-0.087356
0.038634	131420.000	2.1262	29.653	11.079	1.2614	0.31593	0.090729	-0.0039196	-0.2261	-0.090276
0.038634	131420.000	2.1263	29.654	11.656	1.2694	0.33193	0.087106	-0.0070036	-0.2552	-0.092249
0.038643	131450.000	2.1273	29.66	12.13	1.2777	0.34522	0.084959	-0.005854	-0.27515	-0.093457
0.038647	131470.000	2.1277	29.664	12.657	1.2902	0.36044	0.083355	-0.0013922	-0.29513	-0.093557
0.038645	131460.000	2.1275	29.662	13.185	1.3037	0.37664	0.081951	0.0042161	-0.31293	-0.092885
0.03865	131480.000	2.1281	29.666	13.707	1.3061	0.39055	0.080268	0.01141	-0.33105	-0.092434
0.038655	131490.000	2.1286	29.67	14.231	1.3098	0.40557	0.077511	0.012488	-0.3475	-0.089973
0.038626	131390.000	2.1253	29.647	14.754	1.312	0.41907	0.074922	0.012913	-0.36205	-0.087996
0.038585	131250.000	2.1208	29.616	15.794	1.3053	0.44534	0.068228	0.014618	-0.39699	-0.08019
0.038559	131170.000	2.118	29.596	16.815	1.2529	0.45316	0.051539	-0.02769	-0.42651	-0.058543
0.038523	131040.000	2.1141	29.568	18.895	1.2375	0.49955	0.034849	-0.042009	-0.45754	-0.035997

Table 34. Rigid Wing 30 mph Alpha Sweeps (β = -8°)

Mach #	Rex	$q_{corrected}$	U_∞	$\alpha_{corrected}$	C_L	$C_{D\_correct}$	C_Y	$C_{\ell\_cg\_w}$	$C_{m\_cg\_c\_w}$	$C_{n\_cg\_w}$
0.038735	131770.000	2.1373	29.729	-10.492	-0.32611	0.12026	0.15531	0.23772	-0.004103	0.030533
0.03876	131860.000	2.1402	29.749	-8.6838	-0.16926	0.097698	0.1315	0.20586	-0.0076655	0.040897
0.038731	131760.000	2.137	29.726	-6.5009	0.047844	0.082047	0.10428	0.18419	-0.0093564	0.053719
0.038758	131850.000	2.1399	29.747	-4.2251	0.27801	0.075778	0.07849	0.16997	-0.0085046	0.066108
0.038797	131980.000	2.1442	29.777	-2.1291	0.49543	0.080618	0.053237	0.15984	-0.0056536	0.078366
0.0388	131990.000	2.1446	29.779	0.052532	0.7095	0.093002	0.025377	0.14572	-0.0051018	0.086729
0.038791	131960.000	2.1436	29.772	2.2302	0.91473	0.11347	0.0090338	0.12447	-0.010083	0.09143
0.038746	131810.000	2.1386	29.738	4.3164	1.1097	0.1457	-0.0064948	0.085406	-0.01372	0.094396
0.038695	131640.000	2.133	29.699	6.468	1.2559	0.19446	-0.035244	0.016696	-0.024643	0.087116
0.038749	131820.000	2.1389	29.74	8.4943	1.3155	0.25849	-0.03103	-0.10604	-0.040683	0.077444
0.038761	131860.000	2.1403	29.749	10.592	1.3396	0.32288	-0.039053	-0.20509	-0.052014	0.066379
0.038784	131940.000	2.1428	29.767	12.683	1.3476	0.39032	-0.046775	-0.27034	-0.056697	0.053403
0.038764	131870.000	2.1406	29.752	13.202	1.3409	0.40846	-0.041261	-0.29275	-0.055969	0.050133
0.038724	131730.000	2.1362	29.721	13.721	1.3365	0.4259	-0.032811	-0.32418	-0.059542	0.049447
0.038689	131620.000	2.1323	29.694	14.231	1.3097	0.44529	0.00026122	-0.37091	-0.064864	0.052375
0.038715	131700.000	2.1351	29.714	14.746	1.2953	0.45365	-0.0053833	-0.39745	-0.065219	0.049199
0.038704	131670.000	2.134	29.706	16.803	1.2266	0.49231	0.0030983	-0.47982	-0.058555	0.042347
0.038651	131490.000	2.1282	29.665	18.887	1.2208	0.54472	0.018939	-0.53423	-0.05649	0.038768

Elevon Deflected Runs

Table 35. Single Elevon ($\delta_{e,PORT}$ = 0 ° & $\delta_{e,STAR}$ = -20 °)

Mach #	Rex	$q_{corrected}$	U∞	$\alpha_{corrected}$	C_L	$C_{D\_correct}$	$C_{\ell\_cg\_w}$	$C_{m\_cg\_c\_w}$	$C_{n\_cg\_w}$
0.039425	134110.00	2.21	30.26	-3.9661	0.27366	0.04981	-0.0092348	-0.026453	0.043283
0.039516	134420.00	2.22	30.33	-2.153	0.44138	0.053823	-0.014439	-0.026829	0.047785
0.039542	134510.00	2.23	30.35	0.022837	0.6423	0.069649	-0.018164	-0.029546	0.050432
0.039503	134380.00	2.22	30.32	2.1933	0.83122	0.090214	-0.021811	-0.040212	0.053526
0.039347	133850.00	2.21	30.2	4.2754	1.0171	0.11908	-0.025802	-0.061143	0.055392
0.039373	133930.00	2.21	30.22	6.4372	1.1863	0.1603	-0.031585	-0.10156	0.05823
0.039347	133850.00	2.21	30.2	8.4823	1.2884	0.21145	-0.036509	-0.17784	0.056295
0.039334	133800.00	2.20	30.19	10.586	1.3252	0.27127	-0.04491	-0.27575	0.055309
0.039347	133850.00	2.21	30.2	12.69	1.3568	0.3571	-0.0301	-0.34695	0.054351
0.039242	133490.00	2.19	30.12	14.771	1.3589	0.43245	-0.044213	-0.46092	0.05997
0.039151	133180.00	2.18	30.05	16.845	1.324	0.48872	-0.038305	-0.54922	0.068067
0.039125	133090.00	2.18	30.03	18.921	1.2913	0.54193	-0.034211	-0.58097	0.077204
0.039021	132740.00	2.17	29.95	21.051	1.2024	0.56974	-0.024777	-0.59703	0.082499

Table 36. Single Elevon ($\delta_{e,PORT}$ = 0 ° & $\delta_{e,STAR}$ = +20 °)

Mach #	Rex	$q_{corrected}$	U∞	$\alpha_{corrected}$	C_L	$C_{D\_correct}$	$C_{\ell\_cg\_w}$	$C_{m\_cg\_c\_w}$	$C_{n\_cg\_w}$
0.039086	132960.00	2.18	30	-3.9943	0.20988	0.052021	0.032916	0.20024	-0.05174
0.039073	132910.00	2.17	29.99	-2.1826	0.37438	0.053685	0.025873	0.20383	-0.051783
0.039086	132960.00	2.18	30	-0.004466	0.58052	0.063214	0.018032	0.20174	-0.052597
0.03906	132870.00	2.17	29.98	2.0806	0.77302	0.081394	0.010772	0.19356	-0.053009
0.039021	132740.00	2.17	29.95	4.2499	0.95925	0.10703	0.0015578	0.17377	-0.053979
0.039034	132780.00	2.17	29.96	6.4121	1.1293	0.1444	-0.0081514	0.13213	-0.053067
0.039021	132740.00	2.17	29.95	8.4565	1.23	0.19254	-0.017848	0.047332	-0.054405
0.039008	132690.00	2.17	29.94	10.562	1.2725	0.25	-0.030355	-0.056552	-0.05402
0.038982	132600.00	2.16	29.92	12.67	1.3117	0.33617	-0.017559	-0.12769	-0.054066
0.038982	132600.00	2.16	29.92	14.749	1.311	0.4047	-0.043628	-0.26096	-0.04308
0.038942	132470.00	2.16	29.89	16.825	1.2785	0.45737	-0.033342	-0.37424	-0.038041
0.038929	132430.00	2.16	29.88	18.901	1.2458	0.5054	-0.025899	-0.39208	-0.038422
0.038916	132380.00	2.16	29.87	20.955	1.1655	0.53326	-0.05312	-0.42033	-0.031648

Table 37. Single Elevon ($\delta_{e,PORT}$ = 0 ° & $\delta_{e,STAR}$ = +10 °)

Mach #	Rex	$q_{corrected}$	U∞	$\alpha_{corrected}$	C_L	$C_{D\_correct}$	$C_{\ell\_cg\_w}$	$C_{m\_cg\_c\_w}$	$C_{n\_cg\_w}$
0.039065	132890.00	2.17	29.984	-3.9889	0.22205	0.047081	0.026941	0.1629	-0.040845
0.039098	133000.00	2.18	30.01	-2.1777	0.38534	0.048655	0.021104	0.16867	-0.042613
0.03906	132870.00	2.17	29.98	0.002255	0.59573	0.059131	0.01387	0.16951	-0.044447
0.039034	132780.00	2.17	29.96	2.0872	0.78797	0.077112	0.0068929	0.16214	-0.044793
0.039008	132690.00	2.17	29.94	4.2542	0.96903	0.10288	-0.0011544	0.14449	-0.046415
0.039034	132780.00	2.17	29.96	6.4174	1.1415	0.14078	-0.010998	0.10369	-0.045905
0.039047	132830.00	2.17	29.97	8.4622	1.2428	0.18878	-0.02002	0.019032	-0.046449
0.039008	132690.00	2.17	29.94	10.568	1.2843	0.24709	-0.033335	-0.08274	-0.047048
0.038982	132600.00	2.16	29.92	12.673	1.3202	0.33219	-0.020565	-0.15625	-0.048113
0.038956	132510.00	2.16	29.9	14.753	1.3185	0.40221	-0.04196	-0.28385	-0.041097
0.038916	132380.00	2.16	29.87	16.823	1.2733	0.45035	-0.044193	-0.37769	-0.036053
0.03889	132290.00	2.15	29.85	18.906	1.2579	0.5063	-0.017169	-0.41944	-0.035681
0.038851	132160.00	2.15	29.82	21.032	1.1806	0.53263	-0.036827	-0.44735	-0.015591

Table 38. Single Elevon ($\delta_{e,PORT}$ = 0 ° & $\delta_{e,STAR}$ = -10 °)

Mach #	Rex	$q_{corrected}$	U_∞	$\alpha_{corrected}$	C_L	$C_{D\_correct}$	$C_{\ell\_cg\_w}$	$C_{m\_cg\_c\_w}$	$C_{n\_cg\_w}$
0.039438	134160.00	2.22	30.27	-3.9678	0.2697	0.047056	-0.0054287	-0.0015641	0.032586
0.039451	134200.00	2.22	30.28	-2.1561	0.43428	0.050657	-0.0095021	-0.0008959	0.035875
0.03949	134330.00	2.22	30.31	0.019889	0.63563	0.063256	-0.014388	-0.0013678	0.037322
0.039555	134550.00	2.23	30.36	2.1894	0.82231	0.083778	-0.019071	-0.010727	0.039848
0.039555	134550.00	2.23	30.36	4.2673	0.99855	0.11049	-0.023408	-0.030648	0.039901
0.039516	134420.00	2.22	30.33	6.4292	1.1682	0.15052	-0.030051	-0.068539	0.042475
0.039516	134420.00	2.22	30.33	8.4734	1.2682	0.20003	-0.034721	-0.14632	0.040093
0.03949	134330.00	2.22	30.31	10.578	1.3073	0.25874	-0.044238	-0.24309	0.039931
0.039425	134110.00	2.21	30.26	12.683	1.3422	0.34516	-0.03243	-0.31505	0.038687
0.039438	134160.00	2.22	30.27	14.762	1.3408	0.41574	-0.038596	-0.4214	0.042132
0.039399	134020.00	2.21	30.24	16.834	1.2978	0.4679	-0.030459	-0.51941	0.047234
0.03936	133890.00	2.21	30.21	18.909	1.2652	0.51677	-0.012096	-0.53922	0.05243
0.039294	133670.00	2.20	30.16	21.046	1.1894	0.54771	-0.030154	-0.56106	0.069637

Table 39. Single Elevon ($\delta_{e,PORT}$ = 0 ° & $\delta_{e,STAR}$ = -5 °)

Mach #	Rex	$q_{corrected}$	U_∞	$\alpha_{corrected}$	C_L	$C_{D\_correct}$	$C_{\ell\_cg\_w}$	$C_{m\_cg\_c\_w}$	$C_{n\_cg\_w}$
0.039338	133820.00	2.20	30.194	-3.9727	0.25868	0.041306	0.0024674	0.037558	0.0133
0.039386	133980.00	2.21	30.231	-2.1615	0.42208	0.044344	-0.0028985	0.03915	0.015305
0.039417	134080.00	2.21	30.254	0.016456	0.62787	0.056372	-0.0082484	0.039533	0.015619
0.039349	133860.00	2.21	30.202	2.1883	0.81985	0.076124	-0.013612	0.031067	0.01697
0.039398	134020.00	2.21	30.24	4.2657	0.99506	0.10192	-0.018677	0.010577	0.017476
0.039465	134250.00	2.22	30.292	6.4252	1.159	0.14003	-0.026054	-0.027902	0.019696
0.03943	134130.00	2.21	30.264	8.4711	1.2631	0.18962	-0.031803	-0.10777	0.018709
0.039438	134160.00	2.22	30.27	10.575	1.3002	0.24771	-0.043498	-0.20509	0.019287
0.039452	134210.00	2.22	30.282	12.676	1.333	0.33245	-0.034757	-0.27599	0.018906
0.039394	134010.00	2.21	30.236	14.764	1.3344	0.40281	-0.045355	-0.39731	0.024644
0.039288	133650.00	2.20	30.155	16.837	1.3041	0.45748	-0.051826	-0.4887	0.033775
0.03929	133650.00	2.20	30.157	18.91	1.2721	0.50578	-0.014424	-0.51069	0.035381
0.039296	133670.00	2.20	30.161	21.05	1.1938	0.53637	-0.037071	-0.53901	0.05233

Table 40. Single Elevon ($\delta_{e,PORT}$ = 0 ° & $\delta_{e,STAR}$ = +5 °)

Mach #	Rex	$q_{corrected}$	U_∞	$\alpha_{corrected}$	C_L	$C_{D\_correct}$	$C_{\ell\_cg\_w}$	$C_{m\_cg\_c\_w}$	$C_{n\_cg\_w}$
0.039712	135090.00	2.25	30.48	-3.986	0.22866	0.042881	0.018235	0.11009	-0.020835
0.039699	135040.00	2.25	30.47	-2.174	0.39383	0.045693	0.011829	0.1136	-0.020827
0.039581	134640.00	2.23	30.38	0.002507	0.5963	0.055729	0.0051665	0.11517	-0.022263
0.039529	134470.00	2.23	30.34	2.0842	0.78109	0.07383	-0.0006119	0.10827	-0.02152
0.039568	134600.00	2.23	30.37	4.2509	0.96143	0.099601	-0.0078313	0.087912	-0.021588
0.039516	134420.00	2.22	30.33	6.4118	1.1287	0.13652	-0.016795	0.049647	-0.020334
0.039555	134550.00	2.23	30.36	8.456	1.2287	0.18465	-0.02468	-0.032179	-0.020875
0.039503	134380.00	2.22	30.32	10.56	1.2678	0.24184	-0.037102	-0.13155	-0.022225
0.039464	134240.00	2.22	30.29	12.668	1.3073	0.32547	-0.028632	-0.1988	-0.020996
0.039464	134240.00	2.22	30.29	14.744	1.2995	0.39382	-0.043676	-0.3294	-0.015403
0.039464	134240.00	2.22	30.29	16.819	1.2659	0.44369	-0.041196	-0.41924	-0.010261
0.039451	134200.00	2.22	30.28	18.897	1.2375	0.49334	-0.0086981	-0.44174	-0.0075337
0.039399	134020.00	2.21	30.24	21.033	1.1614	0.52186	-0.039113	-0.4774	0.015501

Table 41. Tandem Elevon (δ_e = -20°)

Mach #	Rex	$q_{corrected}$	U_∞	$\alpha_{corrected}$	C_L	$C_{D\_correct}$	$C_{\ell\_cg\_w}$	$C_{m\_cg\_c\_w}$	$C_{n\_cg\_w}$
0.039112	133050.00	2.18	30.02	-3.952	0.30554	0.047639	0.010048	-0.11249	-0.0083389
0.039164	133220.00	2.19	30.06	-2.1376	0.47617	0.052868	0.0045736	-0.11783	-0.0060005
0.039177	133270.00	2.19	30.07	0.039385	0.67975	0.067348	-0.0014567	-0.12291	-0.0047449
0.039177	133270.00	2.19	30.07	2.2136	0.87717	0.089227	-0.0067759	-0.1351	-0.0047798
0.039164	133220.00	2.19	30.06	4.2942	1.0596	0.11819	-0.012572	-0.15921	-0.0063376
0.039177	133270.00	2.19	30.07	6.4581	1.2335	0.15941	-0.020858	-0.19859	-0.0026588
0.03919	133310.00	2.19	30.08	8.5016	1.3321	0.21095	-0.027469	-0.27706	-0.0052623
0.039138	133140.00	2.18	30.04	10.607	1.3728	0.27247	-0.038664	-0.3756	-0.0069302
0.039099	133000.00	2.18	30.01	12.71	1.4038	0.35976	-0.020978	-0.43976	-0.0089234
0.039034	132780.00	2.17	29.96	14.79	1.4031	0.43436	-0.048038	-0.56061	-0.0005011
0.038982	132600.00	2.16	29.92	16.859	1.3544	0.48581	-0.033819	-0.63349	0.00012654
0.038942	132470.00	2.16	29.89	18.935	1.3245	0.53824	-0.024063	-0.65525	0.01804
0.038877	132250.00	2.15	29.84	21.064	1.2306	0.56617	-0.048116	-0.65621	0.045208

Table 42. Tandem Elevon (δ_e = +20°)

Mach #	Rex	$q_{corrected}$	U_∞	$\alpha_{corrected}$	C_L	$C_{D\_correct}$	$C_{\ell\_cg\_w}$	$C_{m\_cg\_c\_w}$	$C_{n\_cg\_w}$
0.039168	133240.00	2.19	30.063	-4.0108	0.17233	0.06138	0.010237	0.31512	-0.0053255
0.039165	133230.00	2.19	30.061	-2.1972	0.34125	0.063602	0.0055051	0.31997	-0.0054939
0.039109	133040.00	2.18	30.018	-0.022303	0.54016	0.07434	0.0013539	0.32304	-0.0044004
0.039124	133090.00	2.18	30.029	2.0615	0.72974	0.091788	-0.0049077	0.31481	-0.0032047
0.039112	133050.00	2.18	30.021	4.2295	0.91314	0.11679	-0.012805	0.29264	-0.0028407
0.039081	132940.00	2.18	29.997	6.3916	1.083	0.15347	-0.019539	0.25012	-0.0023861
0.039058	132860.00	2.17	29.979	8.4384	1.1889	0.20125	-0.027853	0.16214	-0.0040419
0.039028	132760.00	2.17	29.956	10.544	1.2321	0.2588	-0.039738	0.057041	-0.0049756
0.039044	132820.00	2.17	29.968	12.645	1.2627	0.34073	-0.024515	-0.02305	-0.0050177
0.039064	132880.00	2.17	29.984	14.731	1.2609	0.41015	-0.042611	-0.15961	0.0062623
0.039055	132850.00	2.17	29.976	16.807	1.2345	0.46176	-0.040687	-0.28636	0.01331
0.039047	132830.00	2.17	29.97	18.884	1.2132	0.51314	-0.020771	-0.31411	0.0038825
0.039017	132730.00	2.17	29.948	20.936	1.1347	0.5401	-0.042929	-0.32176	0.03356

Table 43. Tandem Elevon (δ_e = +10°)

Mach #	Rex	$q_{corrected}$	U_∞	$\alpha_{corrected}$	C_L	$C_{D\_correct}$	$C_{\ell\_cg\_w}$	$C_{m\_cg\_c\_w}$	$C_{n\_cg\_w}$
0.039191	133320.00	2.19	30.081	-3.9993	0.19837	0.049774	0.015712	0.22326	-0.014566
0.039168	133240.00	2.19	30.063	-2.1871	0.36418	0.051673	0.010274	0.23108	-0.015523
0.039169	133240.00	2.19	30.064	-0.010004	0.56799	0.061275	0.0048386	0.2311	-0.016702
0.039164	133220.00	2.18	30.06	2.163	0.76251	0.079484	-0.0017484	0.22321	-0.0167
0.039118	133070.00	2.18	30.025	4.2437	0.94529	0.10456	-0.0083923	0.20457	-0.016563
0.039116	133060.00	2.18	30.023	6.4047	1.1126	0.14107	-0.017281	0.16399	-0.016015
0.039094	132980.00	2.18	30.006	8.4531	1.2223	0.18935	-0.025695	0.067007	-0.012713
0.03908	132940.00	2.18	29.996	10.556	1.2589	0.24641	-0.037237	-0.026133	-0.017727
0.039057	132860.00	2.17	29.978	12.659	1.2943	0.33063	-0.027366	-0.09686	-0.018208
0.039068	132900.00	2.17	29.987	14.747	1.2973	0.4007	-0.045846	-0.22147	-0.010677
0.039033	132780.00	2.17	29.96	16.821	1.2668	0.45349	-0.045756	-0.33205	-0.0041566
0.039015	132720.00	2.17	29.946	18.898	1.2438	0.50511	-0.018267	-0.36656	-0.006489
0.039009	132700.00	2.17	29.941	21.008	1.1635	0.53057	-0.040861	-0.40238	0.014411

Table 44. Tandem Elevon (δ_e = -10°)

Mach #	Rex	$q_{corrected}$	U_∞	$\alpha_{corrected}$	C_L	$C_{D\_correct}$	$C_{\ell\_cg\_w}$	$C_{m\_cg\_c\_w}$	$C_{n\_cg\_w}$
0.039167	133230.00	2.19	30.062	-3.9625	0.2818	0.044458	0.0023756	-0.045117	0.0099693
0.039178	133270.00	2.19	30.071	-2.1495	0.4493	0.04859	-0.0021213	-0.046252	0.012082
0.039166	133230.00	2.19	30.062	0.03162	0.66218	0.0621	-0.0068638	-0.048039	0.012331
0.039171	133250.00	2.19	30.066	2.2032	0.85352	0.083335	-0.0112	-0.05868	0.013829
0.039138	133140.00	2.18	30.04	4.2842	1.0369	0.11152	-0.016962	-0.079058	0.013024
0.039142	133150.00	2.18	30.044	6.448	1.2106	0.15236	-0.025881	-0.11894	0.016032
0.039202	133350.00	2.19	30.09	8.4901	1.3058	0.2024	-0.031002	-0.19468	0.013934
0.039142	133150.00	2.18	30.043	10.595	1.3471	0.26304	-0.046516	-0.29185	0.013611
0.039129	133110.00	2.18	30.033	12.695	1.3768	0.34933	-0.035509	-0.36527	0.013687
0.039068	132900.00	2.17	29.986	14.781	1.3747	0.42329	-0.049317	-0.48755	0.018434
0.039026	132760.00	2.17	29.955	16.859	1.3527	0.48168	0.00053032	-0.54784	0.020454
0.039016	132720.00	2.17	29.947	18.925	1.3065	0.52893	-0.021188	-0.58995	0.034563
0.038932	132440.00	2.16	29.882	21.059	1.2152	0.55561	-0.033422	-0.60183	0.050006

Table 45. Opposed Elevon ($\delta_{e,PORT}$ = -10 ° & $\delta_{e,STAR}$ = +10 °)

Mach #	Rex	$q_{corrected}$	U_∞	$\alpha_{corrected}$	C_L	$C_{D\_correct}$	$C_{\ell\_cg\_w}$	$C_{m\_cg\_c\_w}$	$C_{n\_cg\_w}$
0.039164	133220.00	2.19	30.06	-3.9867	0.22703	0.051473	0.036995	0.1235	-0.064843
0.039164	133220.00	2.19	30.06	-2.1728	0.39652	0.054648	0.031375	0.12944	-0.067692
0.039203	133360.00	2.19	30.09	0.002966	0.59734	0.065674	0.023841	0.12891	-0.070051
0.039203	133360.00	2.19	30.09	2.1756	0.79103	0.08478	0.01521	0.11995	-0.071721
0.039138	133140.00	2.18	30.04	4.2569	0.97509	0.11147	0.0070247	0.099982	-0.073356
0.039112	133050.00	2.18	30.02	6.4198	1.1469	0.15051	-0.0036667	0.059668	-0.072981
0.039112	133050.00	2.18	30.02	8.4649	1.249	0.19949	-0.01347	-0.023532	-0.074823
0.039086	132960.00	2.18	30	10.568	1.2856	0.25639	-0.029726	-0.12812	-0.076534
0.039073	132910.00	2.17	29.99	12.677	1.3284	0.34337	-0.02717	-0.19505	-0.073337
0.039086	132960.00	2.18	30	14.753	1.3199	0.41281	-0.042646	-0.32301	-0.067254
0.039008	132690.00	2.17	29.94	16.823	1.2749	0.46167	-0.037681	-0.41528	-0.064063
0.039021	132740.00	2.17	29.95	18.909	1.2639	0.51731	-0.018697	-0.45023	-0.058621
0.038956	132510.00	2.16	29.9	21.039	1.1743	0.542	-0.038817	-0.4813	-0.038032

Table 46. Opposed Elevon ($\delta_{e,PORT}$ = -20 ° & $\delta_{e,STAR}$ = +20 °)

Mach #	Rex	$q_{corrected}$	U_∞	$\alpha_{corrected}$	C_L	$C_{D\_correct}$	$C_{\ell\_cg\_w}$	$C_{m\_cg\_c\_w}$	$C_{n\_cg\_w}$
0.039133	133120.00	2.18	30.037	-3.9838	0.23357	0.054866	0.056431	0.10256	-0.10935
0.039139	133140.00	2.18	30.041	-2.1718	0.39866	0.057901	0.047718	0.10404	-0.11104
0.039146	133160.00	2.18	30.046	0.006466	0.60526	0.068534	0.03695	0.10184	-0.11262
0.039152	133180.00	2.18	30.051	2.1777	0.79578	0.087135	0.027974	0.091337	-0.11415
0.039163	133220.00	2.18	30.06	4.2602	0.98247	0.11353	0.017729	0.069003	-0.11724
0.039112	133050.00	2.18	30.02	6.4247	1.158	0.1519	0.0055972	0.026075	-0.11699
0.039099	133000.00	2.18	30.01	8.4704	1.2613	0.20074	-0.0057998	-0.056982	-0.12017
0.039078	132930.00	2.18	29.994	10.575	1.3012	0.25886	-0.02254	-0.16628	-0.12079
0.039093	132980.00	2.18	30.006	12.68	1.3425	0.3441	-0.016978	-0.23129	-0.11887
0.039069	132900.00	2.17	29.987	14.763	1.332	0.41319	-0.041175	-0.37001	-0.10841
0.039015	132720.00	2.17	29.946	16.835	1.2978	0.46562	-0.039819	-0.45364	-0.10336
0.038973	132570.00	2.16	29.913	18.914	1.2804	0.52087	-0.030953	-0.48597	-0.10906
0.038963	132540.00	2.16	29.906	21.059	1.2163	0.55592	-0.03962	-0.51381	-0.11065

Table 47. RIGID Tandem Elevon (δ_e = -10°)

Mach #	Rex	$q_{corrected}$	U_∞	$\alpha_{corrected}$	C_L	$C_{D\_correct}$	$C_{\ell\_cg\_w}$	$C_{m\_cg\_c\_w}$	$C_{n\_cg\_w}$
0.03909	132980.00	2.18	30.002	-3.9379	0.33742	0.015239	0.0017691	-0.045612	-0.027586
0.039111	133050.00	2.18	30.018	-2.1163	0.52442	0.03477	0.0019867	-0.06888	-0.016658
0.039144	133160.00	2.18	30.043	0.072251	0.75413	0.069284	0.001668	-0.092689	-0.0037423
0.039155	133200.00	2.18	30.052	2.2531	0.96641	0.11353	0.0062266	-0.11847	0.0077249
0.039178	133280.00	2.19	30.07	4.3384	1.1596	0.16561	0.01064	-0.15746	0.016882
0.039184	133300.00	2.19	30.074	6.4903	1.3065	0.22659	0.012152	-0.16928	-0.0011883
0.039153	133190.00	2.18	30.05	8.5229	1.3802	0.30569	-0.0098123	-0.25894	0.013674
0.039146	133170.00	2.18	30.045	10.602	1.3616	0.38164	-0.015236	-0.33248	0.037403
0.039111	133050.00	2.18	30.018	12.679	1.3388	0.46095	0.00080541	-0.40069	0.044142
0.039091	132980.00	2.18	30.003	14.762	1.3305	0.55749	0.020165	-0.47259	0.063169
0.039029	132770.00	2.17	29.955	16.814	1.2519	0.63995	0.036027	-0.59231	0.082845
0.038954	132520.00	2.16	29.898	18.865	1.1708	0.70004	0.058368	-0.69841	0.10447

Table 48. RIGID Tandem Elevon (δ_e = +10°)

Mach #	Rex	$q_{corrected}$	U_∞	$\alpha_{corrected}$	C_L	$C_{D\_correct}$	$C_{\ell\_cg\_w}$	$C_{m\_cg\_c\_w}$	$C_{n\_cg\_w}$
0.040441	137580.00	2.33	31.039	-3.9983	0.20074	0.028806	0.00878	0.35426	-0.038468
0.039765	135270.00	2.25	30.52	-2.1771	0.38671	0.045578	0.0097923	0.36242	-0.030258
0.039311	133730.00	2.20	30.171	0.011447	0.61653	0.076685	0.0091236	0.36128	-0.02071
0.039125	133100.00	2.18	30.029	2.1925	0.82941	0.11638	0.013237	0.33633	-0.010263
0.039068	132900.00	2.17	29.985	4.2817	1.0313	0.16449	0.016403	0.2918	0.001243
0.039085	132960.00	2.18	29.998	6.4404	1.1936	0.22358	0.012478	0.22455	0.0054809
0.039148	133180.00	2.18	30.047	8.4705	1.2616	0.29767	-0.0094309	0.11669	0.021928
0.039092	132990.00	2.18	30.003	10.554	1.2528	0.37197	-0.018316	0.038685	0.046047
0.039071	132920.00	2.17	29.987	12.63	1.2283	0.4443	0.0019845	-0.015544	0.049169
0.039135	133130.00	2.18	30.036	14.713	1.2189	0.53789	0.023556	-0.11342	0.071809
0.039099	133010.00	2.18	30.008	16.772	1.1559	0.61836	0.026102	-0.26163	0.09636
0.039097	133000.00	2.18	30.007	18.827	1.0839	0.66887	0.056809	-0.40633	0.11015

Table 49. RIGID Opposed Elevon ($\delta_{e,PORT}$ = -10 ° & $\delta_{e,STAR}$ = +10 °)

Mach #	Rex	$q_{corrected}$	U_∞	$\alpha_{corrected}$	C_L	$C_{D\_correct}$	$C_{\ell\_cg\_w}$	$C_{m\_cg\_c\_w}$	$C_{n\_cg\_w}$
0.039463	134250.00	2.22	30.288	-3.9713	0.26181	0.024119	0.04706	0.19284	-0.12377
0.039498	134370.00	2.22	30.315	-2.1522	0.44306	0.040644	0.045246	0.17584	-0.11915
0.039464	134250.00	2.22	30.289	0.034111	0.66782	0.072489	0.041435	0.15546	-0.1119
0.039319	133760.00	2.20	30.178	2.2154	0.88128	0.11312	0.04105	0.12891	-0.10294
0.039218	133420.00	2.19	30.1	4.3032	1.0799	0.1628	0.041151	0.086828	-0.09447
0.039326	133780.00	2.20	30.183	6.4591	1.2359	0.22212	0.033182	0.026921	-0.088436
0.039094	132990.00	2.18	30.005	8.4966	1.3206	0.30153	0.0063778	-0.073535	-0.073229
0.039018	132730.00	2.17	29.946	10.58	1.3122	0.37652	-0.0069944	-0.1497	-0.048252
0.039025	132760.00	2.17	29.952	12.656	1.2868	0.45133	0.012216	-0.2069	-0.047051
0.039009	132700.00	2.17	29.939	14.735	1.2698	0.544	0.033313	-0.29659	-0.024048
0.039019	132740.00	2.17	29.947	16.798	1.2144	0.62954	0.032244	-0.43332	0.0047885
0.038995	132650.00	2.17	29.929	18.849	1.1335	0.68168	0.05384	-0.56633	0.027626

Lift and Drag Error Tables

Table 50. Flexible 10 mph Drag with Errors

	(+) Drag	(-) Drag
Drag (lb_f)	Error (lb_f)	Error (lb_f)
0.003227336	0.017774607	-0.011319936
0.005980339	0.020527611	-0.008566932
0.011601148	0.02614842	-0.002946123
0.018264374	0.032811646	0.003717103
0.027211448	0.041758719	0.012664176
0.037315801	0.051863072	0.022768529
0.047642925	0.062190197	0.033095654
0.062476331	0.077023602	0.047929059
0.066420274	0.080967545	0.051873002
0.069233709	0.08378098	0.054686437
0.072613764	0.087161036	0.058066493
0.075428809	0.08997608	0.060881537
0.076929609	0.09147688	0.062382337
0.079401817	0.093949089	0.064854546
0.083605512	0.098152783	0.069058241
0.094047572	0.108594843	0.0795003
0.105143669	0.11969094	0.090596398

Table 51. Flexible 30 mph Drag with Errors

	(+) Drag	(-) Drag
Drag (lb_f)	Error (lb_f)	Error (lb_f)
0.068986025	0.083533296	0.054438754
0.073834609	0.088381881	0.059287338
0.090970221	0.105517492	0.076422949
0.117027061	0.131574333	0.10247979
0.155791944	0.170339215	0.141244673
0.210926038	0.22547331	0.196378767
0.27928789	0.293835161	0.264740619
0.354730118	0.369277389	0.340182846
0.358369684	0.372916956	0.343822413
0.380125051	0.394672322	0.365577779
0.399682424	0.414229695	0.385135153
0.431079705	0.445626976	0.416532433
0.462602353	0.477149624	0.448055082
0.494383409	0.50893068	0.479836138
0.582596916	0.597144187	0.568049644
0.660226875	0.674774146	0.645679604
0.738224476	0.752771748	0.723677205

Table 52. Flexible 10 mph Lift with Errors

Lift (lb_f)	(+) Lift Error (lb_f)	(-) Lift Error (lb_f)
0.072377041	0.091915286	0.052838796
0.117109837	0.136648082	0.097571592
0.167269583	0.186807828	0.147731338
0.207728002	0.227266247	0.188189757
0.244132801	0.263671046	0.224594556
0.26187838	0.281416625	0.242340135
0.29590438	0.315442625	0.276366135
0.289563329	0.309101574	0.270025084
0.288938284	0.308476529	0.269400039
0.28401864	0.303556885	0.264480395
0.27957502	0.299113265	0.260036775
0.278094549	0.297632794	0.258556304
0.26687816	0.286416405	0.247339915
0.263701	0.283239246	0.244162755
0.260715823	0.280254069	0.241177578
0.258834351	0.278372597	0.239296106
0.261262944	0.280801189	0.241724699

Table 53. Flexible 30 mph Lift with Errors

Lift (lb_f)	(+) Lift Error (lb_f)	(-) Lift Error (lb_f)
0.346396545	0.36593479	0.3268583
0.580607372	0.600145617	0.561069127
0.867353977	0.886892222	0.847815732
1.122296892	1.141835138	1.102758647
1.377729045	1.39726729	1.3581908
1.615517297	1.635055542	1.595979052
1.760785806	1.780324051	1.74124756
1.799871104	1.819409349	1.780332859
1.801724144	1.821262389	1.782185899
1.81211865	1.831656895	1.792580405
1.820122412	1.839660657	1.800584167
1.826407443	1.845945688	1.806869198
1.847468253	1.867006498	1.827930008
1.859243604	1.878781849	1.839705359
1.868461957	1.888000203	1.848923712
1.821248061	1.840786306	1.801709816
1.797454804	1.81699305	1.777916559

Table 54. Rigid 10 mph Drag with Errors

	(+) Drag	(-) Drag
Drag (lb_f)	Error (lb_f)	Error (lb_f)
0.015347309	0.02989458	0.000800037
0.013979047	0.028526318	-0.000568224
0.010894735	0.025442006	-0.003652536
0.009056552	0.023603823	-0.00549072
0.007082439	0.02162971	-0.007464832
0.006761284	0.021308555	-0.007785987
0.009854693	0.024401964	-0.004692579
0.014370424	0.028917695	-0.000176847
0.020980954	0.035528226	0.006433683
0.029232588	0.043779859	0.014685317
0.038897786	0.053445057	0.024350515
0.048839155	0.063386426	0.034291883
0.063177429	0.0777247	0.048630157
0.07318736	0.087734631	0.058640088
0.082787909	0.097335181	0.068240638
0.096902336	0.111449607	0.082355064
0.10945585	0.124003121	0.094908579

Table 55. Rigid 30 mph Drag with Errors

	(+) Drag	(-) Drag
Drag (lb_f)	Error (lb_f)	Error (lb_f)
0.171113859	0.18566113	0.156566588
0.170040853	0.184588124	0.155493582
0.162753806	0.177301077	0.148206535
0.146942395	0.161489666	0.132395124
0.133523165	0.148070437	0.118975894
0.123682754	0.138230026	0.109135483
0.113417323	0.127964595	0.098870052
0.117594048	0.132141319	0.103046776
0.13450707	0.149054341	0.119959799
0.166538052	0.181085324	0.151990781
0.210527837	0.225075109	0.195980566
0.267097479	0.281644751	0.252550208
0.350388194	0.364935466	0.335840923
0.427697518	0.442244789	0.413150247
0.50597456	0.520521832	0.491427289
0.60581559	0.620362861	0.591268319
0.689526554	0.704073826	0.674979283
0.745023389	0.75957066	0.730476117

Table 56. Rigid 10 mph Lift with Errors

	(+) Lift	(-) Lift
Lift (lb_f)	Error (lb_f)	Error (lb_f)
-0.085583048	-0.066044803	-0.105121293
-0.070219693	-0.050681448	-0.089757938
-0.044622428	-0.025084183	-0.064160673
-0.018417063	0.001121182	-0.037955308
0.011438545	0.03097679	-0.0080997
0.065446821	0.084985066	0.045908576
0.112941574	0.132479819	0.093403329
0.149133833	0.168672078	0.129595588
0.169311973	0.188850218	0.149773727
0.198233487	0.217771733	0.178695242
0.217452521	0.236990767	0.197914276
0.230475209	0.250013454	0.210936964
0.267697246	0.287235491	0.248159
0.282696937	0.302235182	0.263158692
0.275812144	0.295350389	0.256273899
0.261017982	0.280556227	0.241479736
0.259766936	0.279305181	0.240228691

Table 57. Rigid 30 mph Lift with Errors

	(+) Lift	(-) Lift
Lift (lb_f)	Error (lb_f)	Error (lb_f)
-0.527231189	-0.507692944	-0.546769435
-0.505014336	-0.485476091	-0.524552581
-0.436874332	-0.417336087	-0.456412577
-0.295426683	-0.275888438	-0.314964928
-0.144164225	-0.12462598	-0.16370247
0.017202981	0.036741226	-0.002335264
0.324525462	0.344063707	0.304987217
0.640126292	0.659664537	0.620588047
0.957548325	0.97708657	0.93801008
1.254307885	1.27384613	1.23476964
1.52690673	1.546444975	1.507368485
1.752158346	1.771696592	1.732620101
1.864665085	1.88420333	1.84512684
1.84963494	1.869173185	1.830096695
1.822862832	1.842401077	1.803324587
1.791541929	1.811080175	1.772003684
1.701298989	1.720837234	1.681760744
1.632432733	1.651970978	1.612894487

Moment Error Tables

Table 58. Flexible 10 mph Moment Error Data

ℓ_cg	*+ ℓ_cg* Error	*- ℓ_cg* Error	*m_cg*	*+ m_cg* Error	*- m_cg* Error	*n_cg*	*+ n_cg* Error	*- n_cg* Error
0.0166	0.01767159	0.015622155	0.06032998	0.063090488	0.057569472	-0.005576232	-0.00425331	-0.006899156
0.0074	0.008255237	0.006626766	0.054981967	0.062140974	0.047822961	-0.006568536	-0.00499732	-0.008139752
-4E-04	0.000401981	-0.001111524	0.047394746	0.059861907	0.034927586	-0.007878733	-0.0058249	-0.009932562
-0.001	-0.000497475	-0.002221416	0.036277783	0.053502235	0.01905333	-0.006590705	-0.00434504	-0.008836374
-0.009	-0.008123128	-0.00947872	0.003785119	0.027051305	-0.019481068	-0.007959337	-0.00550385	-0.010414821
0.0303	0.032635635	0.028013403	-0.04946563	-0.020257179	-0.078674087	-0.001216851	0.00149519	-0.003928892
-0.033	-0.033111657	-0.033280812	-0.04086234	-0.00867027	-0.073054415	-0.005510642	-0.00313966	-0.007881627
-0.053	-0.051906478	-0.053708491	-0.12302685	-0.084638546	-0.161415151	-0.005303261	-0.00329176	-0.007314766
-0.046	-0.045383593	-0.046581798	-0.14048499	-0.100658476	-0.180311513	-0.005477172	-0.00329832	-0.007656021
-0.044	-0.043497844	-0.04451929	-0.16375046	-0.122503941	-0.204996969	-0.003059216	-0.00099184	-0.005126593
-0.025	-0.024345783	-0.024805782	-0.18509911	-0.142493271	-0.227704957	-0.008394955	-0.00577125	-0.011018659
-0.026	-0.025865005	-0.026298197	-0.20916666	-0.164767433	-0.253565893	-0.006425776	-0.00385929	-0.008992265
-0.063	-0.061825666	-0.064359415	-0.27069314	-0.222692527	-0.318693748	-0.000401868	0.001231203	-0.00203494
-0.058	-0.056599181	-0.058677792	-0.30287206	-0.252647031	-0.35309709	-0.002510879	-0.00064219	-0.00437957
-0.049	-0.048238526	-0.049687087	-0.35220242	-0.298371873	-0.406032969	-0.003376448	-0.00139025	-0.005362651
-0.036	-0.035976451	-0.036606738	-0.40266602	-0.344665217	-0.460666831	-0.000270063	0.001499009	-0.002039135
-0.038	-0.038105317	-0.038829201	-0.42111625	-0.360865196	-0.481367308	0.006323065	0.007708644	0.004937487

Table 59. Flexible 30 mph Moment Error Data

ℓ_cg	*+ ℓ_cg* Error	*- ℓ_cg* Error	*m_cg*	*+ m_cg* Error	*- m_cg* Error	*n_cg*	*+ n_cg* Error	*- n_cg* Error
0.0558	0.058042001	0.053530591	0.445111499	0.450434873	0.439788125	-0.008163961	-0.00677777	-0.009550156
0.0183	0.019388137	0.017174646	0.462005395	0.486141806	0.437868983	-0.002648029	-0.00146048	-0.003835581
-0.012	-0.011370923	-0.011707182	0.453373935	0.504760867	0.401987002	-0.005549644	-0.00409194	-0.007007348
-0.036	-0.035269642	-0.03646163	0.405203361	0.484272375	0.326134348	-0.004158574	-0.00272397	-0.005593175
-0.068	-0.066054253	-0.069313036	0.286886225	0.399325597	0.174446853	-0.001716185	-0.0004206	-0.003011766
-0.128	-0.124258208	-0.131700025	0.040575825	0.194869137	-0.113717488	0.016596084	0.01672839	0.016463779
-0.167	-0.162134648	-0.172304934	-0.4182208	-0.21418077	-0.622260836	0.013569584	0.013656576	0.013482593
-0.21	-0.20351348	-0.216844631	-0.91172321	-0.664225412	-1.159221003	0.000926367	0.001327423	0.000525311
-0.227	-0.220216684	-0.234768068	-0.93187407	-0.68254027	-1.181207865	-0.002379796	-0.00184582	-0.002913773
-0.253	-0.244887968	-0.261214554	-1.0702319	-0.808664474	-1.331799319	0.007085482	0.007270563	0.006900401
-0.241	-0.232964169	-0.248420682	-1.13359605	-0.865592186	-1.401599906	0.034983567	0.036940437	0.033026698
-0.221	-0.214164433	-0.228268157	-1.21951308	-0.942896482	-1.496129677	0.044362233	0.04685991	0.041864557
-0.18	-0.174783224	-0.186040332	-1.2934548	-1.007753868	-1.579155741	0.026173657	0.027308888	0.025038426
-0.206	-0.199399783	-0.21245765	-1.43711757	-1.138020082	-1.736215066	0.022264858	0.023269784	0.021259932
-0.331	-0.320503838	-0.342326199	-2.14278251	-1.7859555	-2.499609518	0.060611972	0.064662884	0.056561061
-0.31	-0.299525868	-0.320002284	-2.69567057	-2.297746836	-3.093594298	0.077842583	0.083099151	0.072586015
-0.179	-0.172918908	-0.184378239	-2.90065922	-2.484965304	-3.316353143	0.125905643	0.133903719	0.117907567

Table 60..Rigid 10 mph Moment Error Data

ℓ_cg	$+\ell\_cg$ Error	$-\ell\_cg$ Error	m_cg	$+m\_cg$ Error	$-m\_cg$ Error	n_cg	$+n\_cg$ Error	$-n\_cg$ Error
0.217	0.225587458	0.208460685	-0.00088152	0.006424674	-0.008187713	0.002620569	0.005333162	-9.20251E-05
0.2028	0.210902542	0.194628036	-0.00135869	0.004564438	-0.007281814	0.005907074	0.008487456	0.003326692
0.1821	0.189356574	0.174793748	-0.00072286	0.003012035	-0.004457748	0.00720134	0.009342895	0.005059784
0.1646	0.171318736	0.157959204	0.001071998	0.002663459	-0.000519462	0.008327321	0.01033594	0.006318701
0.1475	0.153341459	0.141624995	-0.00024655	0.001219804	-0.00171291	0.013218153	0.014388589	0.012047717
0.1167	0.121161898	0.11215839	-0.00238335	0.004072694	-0.008839396	0.016702453	0.016954041	0.016450864
0.0963	0.100025988	0.092614277	-0.00333145	0.007670568	-0.014333468	0.021611594	0.021939153	0.021284035
0.0569	0.059481712	0.054352417	-0.00607602	0.008633666	-0.020785698	0.02635535	0.026690808	0.026019892
-0.032	-0.03148381	-0.031919911	-0.0071562	0.009781365	-0.024093762	0.028087973	0.028286913	0.027889034
-0.07	-0.068272079	-0.071107117	-0.00759126	0.012409286	-0.027591798	0.029800577	0.030017898	0.029583255
-0.128	-0.124277839	-0.131830701	-0.00759106	0.014637725	-0.029819848	0.028586606	0.029611903	0.027561309
-0.174	-0.168324812	-0.180110428	-0.00651395	0.017330139	-0.030358047	0.026437927	0.0285255	0.024350353
-0.171	-0.166805796	-0.174460887	-0.00461553	0.023209344	-0.032440401	0.04723095	0.047674141	0.046787759
-0.184	-0.17715397	-0.191270711	0.003599504	0.032718494	-0.025519486	0.029743042	0.033722736	0.025763349
-0.225	-0.218208531	-0.232753427	-0.00522995	0.024459054	-0.034918946	0.033077798	0.034996234	0.031159361
-0.401	-0.387536717	-0.414898052	-0.00068548	0.028192483	-0.029563444	0.022219043	0.024708611	0.019729474
-0.477	-0.461148423	-0.49359337	0.007220201	0.036181815	-0.021741414	0.017837937	0.020126034	0.01554984

Table 61. Rigid 30 mph Moment Error Data

ℓ_cg	$+\ell\_cg$ Error	$-\ell\_cg$ Error	m_cg	$+m\_cg$ Error	$-m\_cg$ Error	n_cg	$+n\_cg$ Error	$-n\_cg$ Error
1.3333	1.371888517	1.294720465	0.014143045	0.05031592	-0.02202983	-0.042941051	-0.0410399	-0.044842203
1.3167	1.354772237	1.278540403	0.017387181	0.052150157	-0.017375795	-0.04046032	-0.038669	-0.042251642
1.2517	1.287919126	1.215405401	0.017881139	0.047934881	-0.012172604	-0.035267244	-0.03370584	-0.036828647
1.1341	1.167100415	1.10109752	0.025694066	0.046614417	0.004773715	-0.010606873	-0.01013727	-0.011076475
1.0403	1.070743181	1.009937967	0.026882586	0.039344911	0.014420262	0.008690143	0.00907489	0.008305396
0.9538	0.981867563	0.92582425	0.027767372	0.039454586	0.016080158	0.028847285	0.030124467	0.027570104
0.8176	0.841789995	0.793363283	0.015654388	0.04728664	-0.015977864	0.052466541	0.054789449	0.050143634
0.7675	0.790584663	0.744464498	0.015086108	0.071046829	-0.040874612	0.096072764	0.100326232	0.091819296
0.7027	0.724222176	0.681232367	0.011561916	0.09332582	-0.070201988	0.1422607	0.148559039	0.13596236
0.5672	0.58500206	0.549355048	0.002322017	0.109650867	-0.105006833	0.182369577	0.190443707	0.174295446
0.3674	0.379625534	0.355134969	-0.01690302	0.115515589	-0.149321624	0.217788432	0.227430756	0.208146107
0.0736	0.077353917	0.069803863	-0.06832491	0.088414321	-0.225064148	0.23180195	0.24206476	0.221539139
-0.432	-0.420167898	-0.444274173	-0.05752236	0.112599112	-0.227643828	0.078624136	0.082105104	0.075143169
-0.826	-0.802552729	-0.849632182	0.001140342	0.171502058	-0.169221375	0.078724617	0.082210103	0.07523913
-1.139	-1.106149921	-1.171305506	-0.05749091	0.120125851	-0.235107678	0.090094841	0.09408367	0.086106011
-1.614	-1.567461975	-1.659747125	-0.02592564	0.154516111	-0.206367392	0.130645839	0.136430008	0.124861671
-2.41	-2.340474723	-2.479563309	-0.0071412	0.171677632	-0.18596004	0.105844181	0.110530248	0.101158113
-3.054	-2.965795915	-3.142707102	0.022913378	0.199037079	-0.153210323	0.088449748	0.092365718	0.084533778

Appendix E: Error Analysis

The *limitations* section presented an overview of the sources of error in this experiment. This appendix will quantify some of those errors in the 10 mph data runs as well as represent the lift, drag and L/D versus angle of attack plots with the quantified errors indicated as *error bars* on the data lines. The same analysis was also performed on the 30 mph data and results presented to provide a parametric comparison of the relative magnitudes of the errors in both sets of data. Lastly, an analysis on the impact of variable battery placement within the electronics bay of the MAV was quantified as changes in the CG and the associated effects on the moment coefficients plotted as error bars.

Sources of Error

The accuracy of the balance is the largest contributor to the error accumulation in each measurement. The ABLE Company's specification sheets state the accuracy of the MK II 8 lb_f balance is 0.25% of full scale. Table 62 shows the smallest point-to-point difference each of the six sensors can accurately discern.

Table 62. Balance Sensor Accuracies

Sensor	Accuracy
N_1	8 lb_f * (0.25/100) = 0.020 lb_f
N_2	8 lb_f * (0.25/100) = 0.020 lb_f
S_1	5 lb_f * (0.25/100) = 0.01250 lb_f
S_2	5 lb_f * (0.25/100) = 0.01250 lb_f
A_1	5 lb_f * (0.25/100) = 0.01250 lb_f
ℓ	2 in-lb_f * (0.25/100) = 0.0050 in-lb_f

Recall from equation **(17)**, the sensor forces resolve into axial, side and normal forces as follows:

$$A = A_1$$
$$Y = S_1 + S_2$$
$$N = N_1 + N_2$$

In addition, recall equation **(19),** which is used to calculate the lift and drag on the MAV:

$$\begin{bmatrix} D \\ S \\ L \end{bmatrix} = \begin{bmatrix} A*\cos\theta*\cos\psi + Y*\sin\psi + N*\sin\theta*\cos\psi \\ -A*\sin\psi*\cos\theta + Y*\cos\psi - N*\sin\theta*\sin\psi \\ -A*\sin\theta + N*\cos\theta \end{bmatrix}$$

The yaw angle, ψ, was zero during the alpha sweep tests; therefore, the equations used to calculate the lift and drag on the MAV reduce to:

$$D = A * \cos\theta + N * \sin\theta$$
$$L = -A * \sin\theta + N * \cos\theta \qquad \textbf{(33)}$$
$$where:$$
$$\theta = \alpha_g$$

The axial force dominates the drag data, while the normal force dominates the lift data. Doing a simple ratio comparison, the drag is comprised of approximately 80% axial force and 20% normal force, and the lift is comprised of about 80% normal force and 20% axial force. Table 63 shows an excerpt of the data taken from the flex wing MAV 10 mph alpha sweeps run. It is clear from the drag data at the lower angles of attack the measured forces are smaller than the axial force sensor is qualified to measure. Further, the lift data is not much higher than the accuracy of the normal force sensor.

Table 63. Sample 10 mph Drag and Lift Data

$\alpha_{corrected}$	Drag (lbf)	Lift (lbf)
-3.8881	0.003227336	0.072377041
-2.0294	0.005980339	0.117109837
0.1953	0.011601148	0.167269583
2.3947	0.018264374	0.207728002
4.4899	0.027211448	0.244132801
6.6252	0.037315801	0.26187838
8.7189	0.047642925	0.29590438
10.882	0.062476331	0.289563329

The next source of error is the quantization of the analog to digital converter 16-bit data acquisition card. The error in the A/D card conversion is 10 Volts / 2^{16} = 0.000152588. Another source of error is in the calculation of the test tare forces, which were calculated from substituting the test angles of attack into the polynomials generated

for each sensor by curve fitting a 4th degree polynomial to the tare alpha data. Table 64 shows the reduced normal and axial force tare data used in the alpha sweeps test runs.

Table 64. Normal and Axial Force Reduced Tare Data

AOA (α)	Yaw (Ψ)	U∞	N1	N2	A1
-4.087	0	0	-0.03117	0.03256	-0.04889
-2.348	0	0	-0.0212	0.02233	-0.0304
-0.174	0	0	-0.004	0.00569	-0.004
1.826	0	0	0.01225	-0.01006	0.02075
3.913	0	0	0.03013	-0.026	0.047
6	0	0	0.04906	-0.04156	0.07475
8	0	0	0.06833	-0.05713	0.09993
10.087	0	0	0.09147	-0.07527	0.12707
12.087	0	0	0.11213	-0.08931	0.15281
14.174	0	0	0.13713	-0.10807	0.179
16.261	0	0	0.162	-0.12331	0.20525
18.348	0	0	0.1885	-0.141	0.23194
20.522	0	0	0.21615	-0.15731	0.25896

From this data, the following 4th degree polynomials were fit to the above values:

$$\mathbf{N_{1,Test}} = -0.18020417148281\alpha^4 - 0.08562090871270\,\alpha^3 + 0.52592827703285\,\alpha^2 + 0.44279016874778\,\alpha - 0.00284270657035$$

$$\mathbf{N_{2,Test}} = -0.40955714464562\,\alpha^4 + 0.52851701372319\,\alpha^3 - 0.21682779198017\,\alpha^2 - 0.42318781268620\,\alpha + 0.00428940386610$$

$$\mathbf{A_{1,Test}} = 2.21383848813841\,\alpha^4 - 1.78777036601298\,\alpha^3 + 0.43684931967164\,\alpha^2 + 0.70040167218878\,\alpha - 0.00208421033696$$

Substituting the test angle of attack into each of these polynomials generates the actual test tare forces, which are subtracted from the test forces yielding the unbiased sensor forces.

Table 65 shows the result of substituting the angle of attack used in the tare run into the normal and axial force tare polynomials.

Table 65. Tare Forces Evaluated with Tare Polynomials

AOA (α)	N_1	N_2	A_1
-4.087	-0.03173	0.03317	-0.04912
-2.348	-0.0201	0.02123	-0.02992
-0.174	-0.00418	0.005573	-0.00421
1.826	0.0118	-0.0094	0.020626
3.913	0.029819	-0.02546	0.047266
6	0.049174	-0.04185	0.074265
8	0.068934	-0.05774	0.100202
10.087	0.090771	-0.07444	0.127134
12.087	0.112812	-0.09048	0.152713
14.174	0.136911	-0.1072	0.179143
16.261	0.16206	-0.12385	0.205377
18.348	0.18818	-0.14042	0.231578
20.522	0.216326	-0.15756	0.259114

The measured normal and axial force tare values in Table 64 were subtracted from the calculated normal and axial force tare values in Table 65 to determine the relative error at each angle of attack. The sum of those errors were divided by the number of measurements to calculate the absolute error in the normal and axial force tare polynomials. Table 66 lists the absolute error for the normal and axial force tare polynomials.

Table 66. Normal and Axial Sensor Tare Polynomial Error

Sensor	Absolute Error
N_1	4.209266569098509e-004
N_2	6.283885674453657e-004
A_1	2.310254453234565e-004

The major contributors to the experimental error have been computed. The net effect of these errors on both the lift and drag were calculated using a weighted sum based on the allocated weighting of axial to normal force sensor influences. Table 67 shows the flexible wing MAV's lift and drag experimental error.

Table 67. Net Weighted Drag and Lift Errors

	Drag	Lift
10 mph	1.45E-02	1.95E-02
30 mph	1.45E-02	1.95E-02

With the lift and drag errors calculated, the error propagation in the 10 mph and 30 mph data was calculated using the standard uncertainty equation (Hosni, Coleman, Steele, 1998):

If f is a function of $(X_1, X_2, X_3, ...X_N)$

Then the Uncertainty in the resultant function, f, is:

$$U_f = \sqrt{\left(\frac{\partial f}{\partial X_1} * \Delta X_1\right)^2 + \left(\frac{\partial f}{\partial X_2} * \Delta X_2\right)^2 + ...\left(\frac{\partial f}{\partial X_N} * \Delta X_N\right)^2} \quad \textbf{(34)}$$

where:

ΔX_N = Uncertainty in Measured Variable

$\partial f / \partial X_N$ = Absolute Sensitivity Coefficient

Therefore, the uncertainty equation for the drag coefficient follows as:

$$C_D = \frac{D}{0.5 * \rho * U_\infty * S}$$
$$U_{C_D} = \sqrt{\left(\frac{\partial C_D}{\partial D}\Delta D\right)^2 + \left(\frac{\partial C_D}{\partial \rho}\Delta \rho\right)^2 + \left(\frac{\partial C_D}{\partial U_\infty}\Delta U_\infty\right)^2} \quad \textbf{(35)}$$

The uncertainty in the freestream velocity is ±0.4 mph and the uncertainty in the pressure transducer used to calculate the air density is 0.5%. The uncertainty in the lift coefficient was also calculated using equation **(38),** and is:

$$C_L = \frac{L}{0.5 * \rho * U_\infty * S}$$
$$U_{C_L} = \sqrt{\left(\frac{\partial C_L}{\partial L}\Delta L\right)^2 + \left(\frac{\partial C_L}{\partial \rho}\Delta \rho\right)^2 + \left(\frac{\partial C_L}{\partial U_\infty}\Delta U_\infty\right)^2} \quad \textbf{(36)}$$

Table 68 lists the propagated errors in the flexible wing MAV 10 mph drag coefficient data.

Table 68. Flex Wing 10 mph Drag Coefficient Errors

$[\partial C_D/\partial D]^2$	$[\partial C_D/\partial U_\infty]^2$	$[\partial C_D/\partial \rho)]^2$	ΔC_D error
0.008182442	2.51618E-06	1.00681E-08	0.09047082
0.008018446	8.38197E-06	3.38781E-08	0.08959276
0.008064796	3.18186E-05	1.28225E-07	0.0899819
0.008121993	7.96917E-05	3.20073E-07	0.09056492
0.008014602	0.000173422	7.01071E-07	0.09049157
0.008016524	0.000326205	1.31871E-06	0.09134576
0.008038353	0.000533925	2.15546E-06	0.09259824
0.008166608	0.000940186	3.76573E-06	0.09544925
0.008112852	0.001052312	4.22816E-06	0.09575695
0.00800948	0.00112147	4.53541E-06	0.09557973
0.00801076	0.001233842	4.98986E-06	0.0961748
0.007972495	0.001321883	5.35853E-06	0.09643514
0.008076446	0.001402006	5.64656E-06	0.09738634
0.007978854	0.001466548	5.94263E-06	0.09721802
0.008046079	0.001646748	6.64402E-06	0.09848589
0.00807839	0.002096274	8.44106E-06	0.10091137
0.008058334	0.002610003	1.05242E-05	0.10333858

Table 69 lists the propagated errors in the flexible wing MAV 10 mph lift coefficient data.

Table 69. Flex Wing 10 mph Lift Coefficient Errors

$[\partial C_L/\partial L)]^2$	$[\partial C_L/\partial U_\infty]^2$	$[\partial C_L/\partial \rho]^2$	ΔC_L error
0.014760158	0.001265478	5.06363E-06	0.1266124
0.014464328	0.003214261	1.29913E-05	0.1330097
0.014547937	0.006614748	2.66566E-05	0.14556559
0.014651113	0.010308457	4.14028E-05	0.15811696
0.014457393	0.013958959	5.64301E-05	0.1687388
0.01446086	0.016065868	6.49475E-05	0.17490476
0.014500238	0.020596174	8.3147E-05	0.18756215
0.014731594	0.02019621	8.0892E-05	0.18710611
0.014634625	0.019913768	8.0013E-05	0.18608709
0.014448154	0.018873224	7.63264E-05	0.18275039
0.014450463	0.018290203	7.39686E-05	0.1811481
0.014381438	0.017968156	7.28377E-05	0.1800623
0.014568952	0.016872869	6.79553E-05	0.17750993
0.014392908	0.016175544	6.55452E-05	0.1750257
0.014514174	0.016013716	6.46094E-05	0.17490712
0.014572459	0.015878035	6.3936E-05	0.1746838
0.014536281	0.016115003	6.49797E-05	0.17526056

The propagated lift and drag errors are plotted as error bars on the lift and drag plots of the 10 mph and 30 mph data respectively. Figure 59 presents the 10 mph and 30 mph flexible wing MAV drag error bars. The plot reveals the discrepancies in the drag lines are much smaller when the magnitude of the 10 mph errors are taken under consideration.

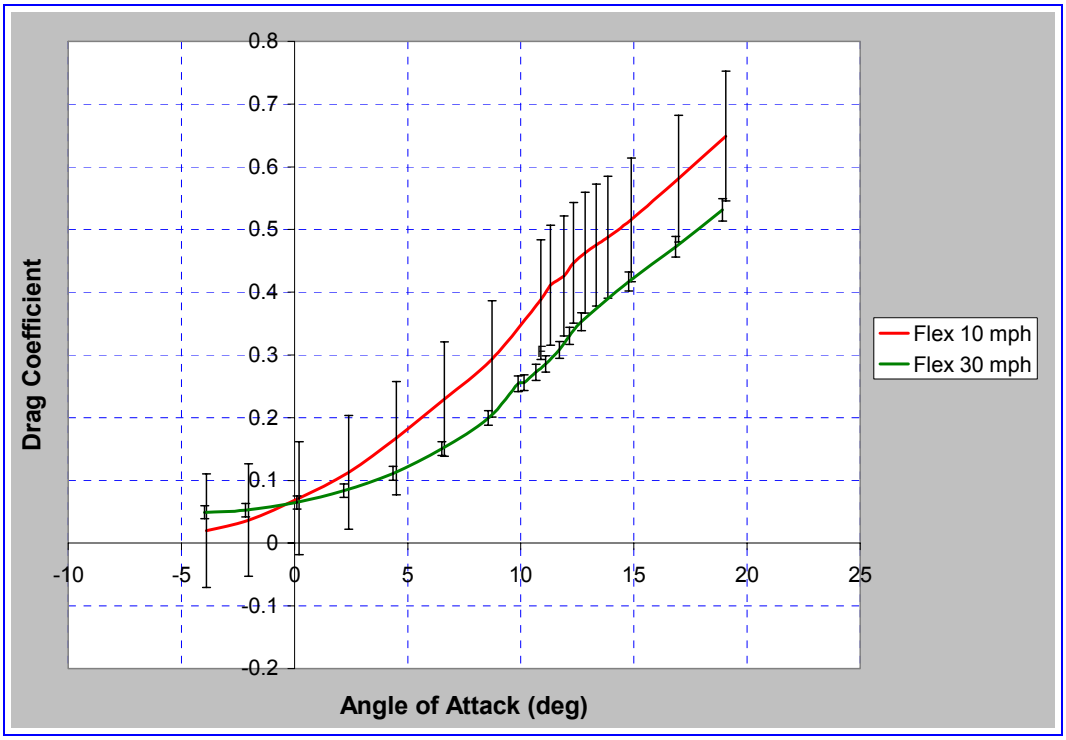

Figure 59. Flex Wing 10 & 30 mph Drag Error Bars

Figure 60 shows the flexible wing MAV 10 mph and 30 mph lift lines plotted with their associated error bars. This plot reveals the differences in the lift lines are not attributable to the propagation of experimental error, but rather are genuinely a result of the aeroelasticity of the flexible wings altering the lift slopes.

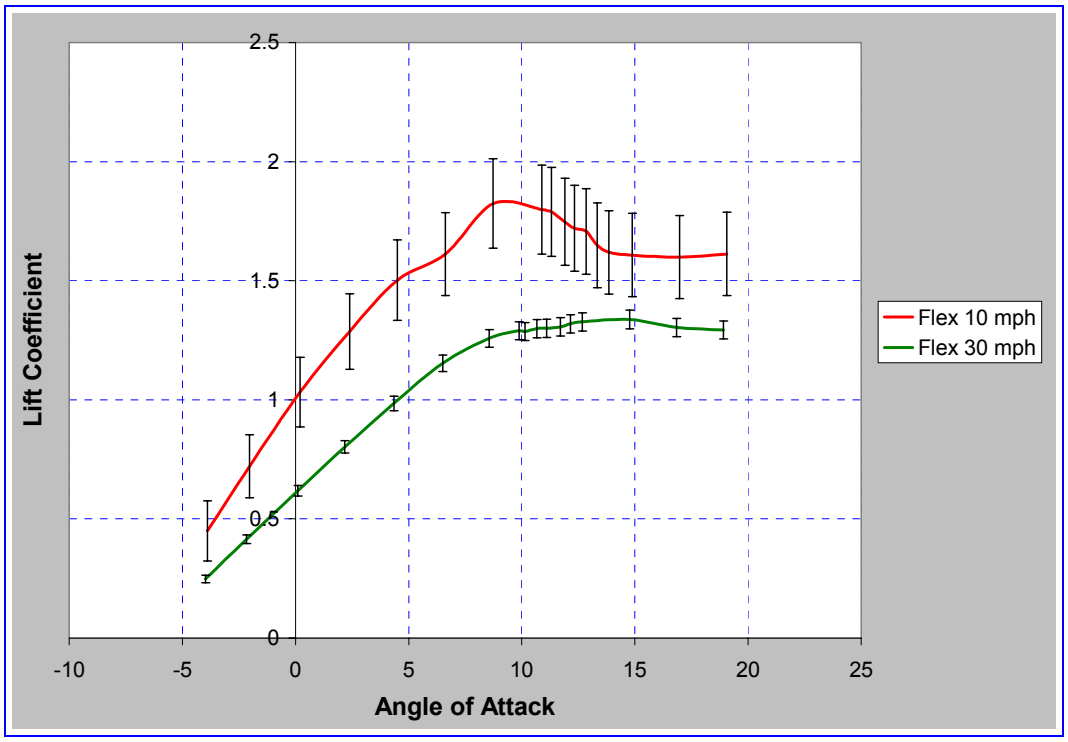

Figure 60. Flex Wing 10 & 30 mph Lift Error Bars

Figure 61 presents the rigid wing MAV 10 mph and 30 mph drag error bars. With the addition of the error bars, the differences in the drag plots nearly vanish after $\alpha = 0°$, while the differences below $\alpha = 0°$ are in the region where the axial and normal forces are smaller than the balance accuracy at those angles.

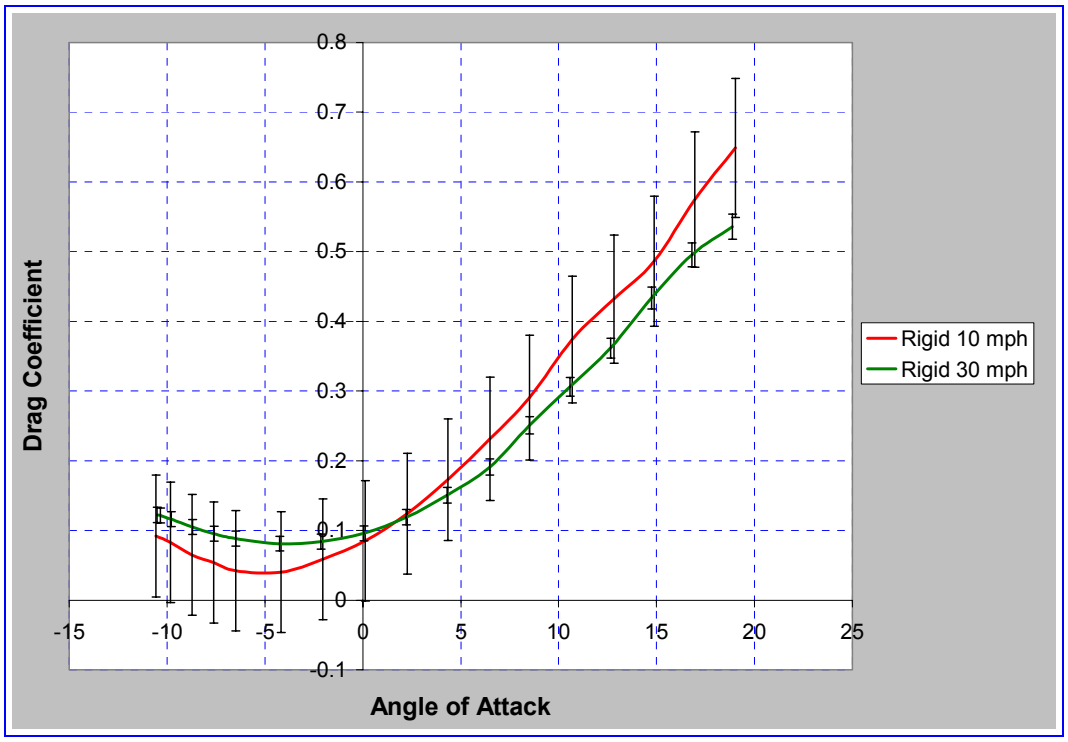

Figure 61. Rigid Wing 10 & 30 mph Drag Error Bars

Figure 62 shows the rigid wing MAV 10 mph and 30 mph lift error bars. Unlike the flexible wing MAV lift error bar plot, the presence of the error bars on the rigid wing MAV lift plot essentially eliminates any discernable differences between the 10 mph and 30 mph lift data. As expected, when comparing the flexible and rigid wing MAVs lift lines, the rigid lift lines are potentially coincident, while the flexible lift lines still show considerable spread resulting from wing deformation under load.

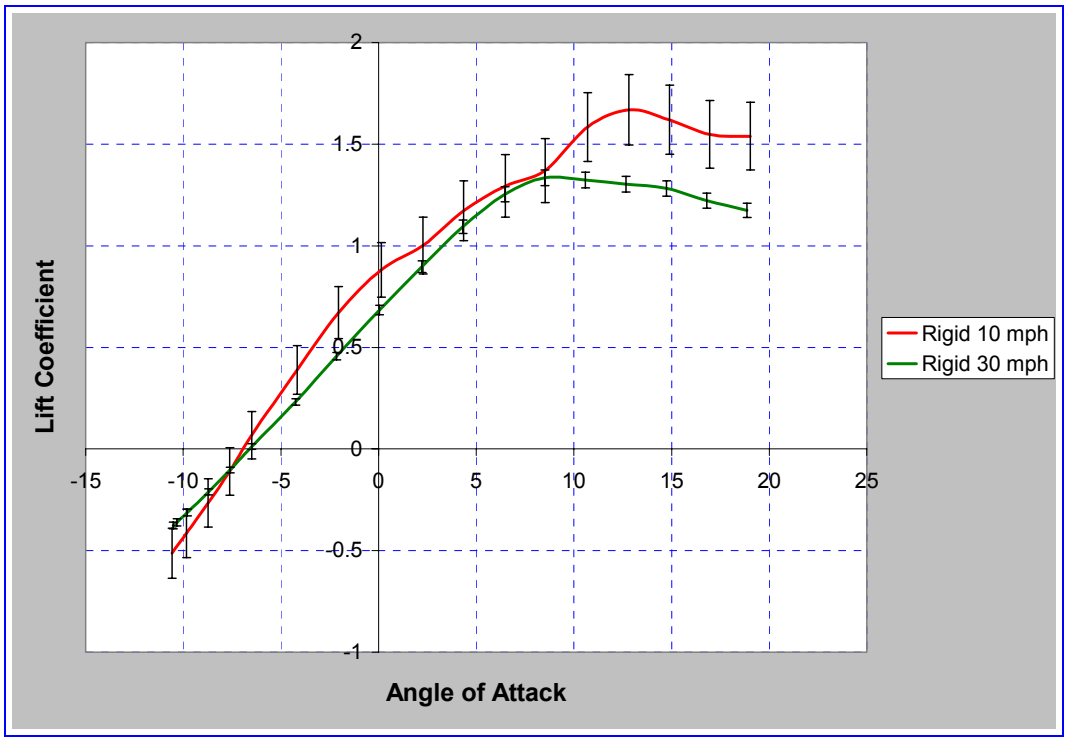

Figure 62. Rigid Wing 10 & 30 mph Lift Error Bars

Lastly, Figure 63 shows a plot of the lift-to-drag ratio without the presence of error bars. It is obvious from the plot that the 10 mph data is increasing without bounds. However, Figure 64 presents the flex 10 mph and 30 mph L/D with error bars and shows the error bars confine the limits of the 10 mph L/D line. The maximum 10 mph L/D is 22.4 and occurs at α = -4°; the maximum L/D with the absolute error included is 22.4 ± 101.3. The maximum 30 mph L/D is 9.6 and occurs at α = -2°; the maximum L/D with the absolute error included is 9.6 ± 1.58.

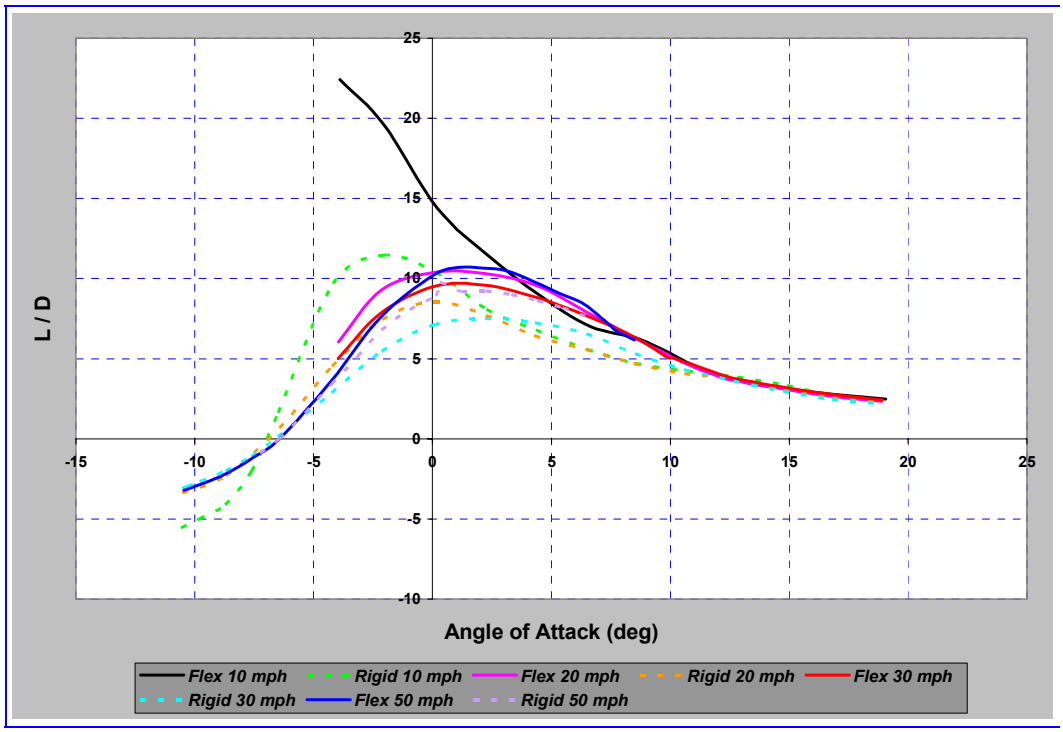

Figure 63. L/D Without Error Bars

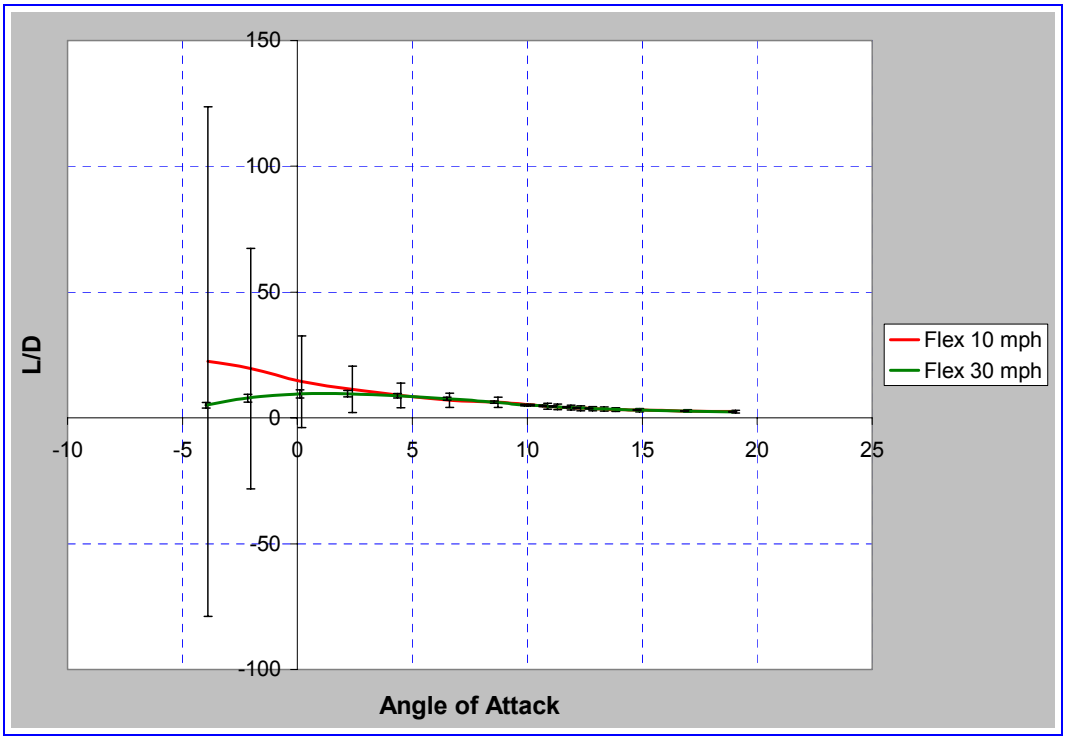

Figure 64. 10 mph and 30 mph L/D with Error Bars

Battery Placement and the Effects on the CG

As stated in the *Limitations* section, the battery is not fixed inside of the electronics bay. I assume AFRL/MNAV did not create a specific battery compartment because they did not assess the effect of the battery location on the CG and subsequent aerodynamic performance consequences. This section will address the amount of potential battery movement, quantify the subsequent CG displacement, and calculate the respective moment coefficient error bars associated with the potential battery displacement.

The mass of the battery is 84 gr. The mass of the flexible wing MAV is 320 gr; therefore, the battery comprises 26.25% of the flexible MAV's mass. The mass of the rigid wing MAV is 360 gr; therefore, the battery comprises 23.33% of the rigid MAV's mass. The battery was placed inside the electronics compartment and the maximum potential displacement was measured in the x-axis from front-to-back and repeated in the z-axis from top-to-bottom. Movement in the y-axis from side-to-side was determined to be negligible. Table 70 summarizes the amount of potential battery displacement and associated CG relocation in the x and z-axes.

Table 70. Battery Displacement and CG Movement

	x-axis Battery	x_{CG} Movement	z-axis Battery	z_{CG} Movement
Flexible	± ¼″	± 0.0656″	± ⅛″	± 0.033″
Rigid	± ¼″	± 0.0583″	± ⅛″	± 0.029″

Once the potential amount of CG displacement was quantified, the errors in the moment coefficients associated with shifting the CG were calculated using equation **(34).** Recall from equation **(22),** the moments in the wind axes, located at the CG, were calculated from:

$$\begin{bmatrix} \ell \\ m \\ n \end{bmatrix}_{wind_{CG}} = \begin{bmatrix} \ell + S*z_{CG} + L*y_{CG} \\ m - L*x_{CG} + D*z_{CG} \\ n - D*y_{CG} - S*x_{CG} \end{bmatrix}_{wind_{bc}}$$

Therefore, applying equation **(34)** to each of the three moments individually, the uncertainties due to the displacement of the CG are readily calculated by:

$$\begin{aligned} \ell_{W_{CG}} &= \ell_{W_{bc}} + S*z_{CG} + L*y_{CG} \\ U_{\ell} &= \sqrt{\left[\left(\ell_{w_{bc}} + S + L*y_{CG}\right)\Delta z_{CG}\right]^2 + \left[\left(\ell_{w_{bc}} + S*z_{CG} + L\right)\Delta y_{CG}\right]^2} \\ m_{W_{CG}} &= m_{W_{bc}} - L*x_{CG} + D*z_{CG} \\ U_{m} &= \sqrt{\left[\left(m_{w_{bc}} - L + D*z_{CG}\right)\Delta x_{CG}\right]^2 + \left[\left(m_{w_{bc}} - L*x_{CG} + D\right)\Delta z_{CG}\right]^2} \\ n_{W_{CG}} &= n_{W_{bc}} - D*y_{CG} - S*x_{CG} \\ U_{n} &= \sqrt{\left[\left(n_{w_{bc}} - D - S*x_{CG}\right)\Delta y_{CG}\right]^2 + \left[\left(n_{w_{bc}} - D*y_{CG} - S\right)\Delta x_{CG}\right]^2} \end{aligned} \quad \textbf{(37)}$$

Figure 65 shows the pitching moment versus angle of attack, $C_{m\alpha}$, for the flexible wing MAV at 10 and 30 mph . As the velocity increases, the effect of moving the CG becomes considerably more pronounced, especially as the angle of attack is increase past 8°. At that point, the MAV is angled such that the pitching moment is highly sensitive to the location of the CG. Moment is the product of force and distance. As the freestream

velocity increases, the lifting force increases, causing an increase in the moments. The CG terms in equation **(22)**, which is used to transfer the moments from the mounting block/set-screws to the MAV CG, are multiplied by the higher forces rendering larger errors than seen at lesser velocities. Figure 66 shows the rigid wing MAV $C_{m\alpha}$ CG error bar plot. Again, the vehicle is showing much higher sensitivity to a change in the CG at 30 mph than 10 mph. In addition, the errors grow increasingly as the angle of attack increases. An interesting aspect of this plot is the effect of the CG on $C_{m\alpha}$ beyond the zero lift line, $\alpha_{LO} \approx 6.5°$, begins to increase similar to the much higher angles of attack.

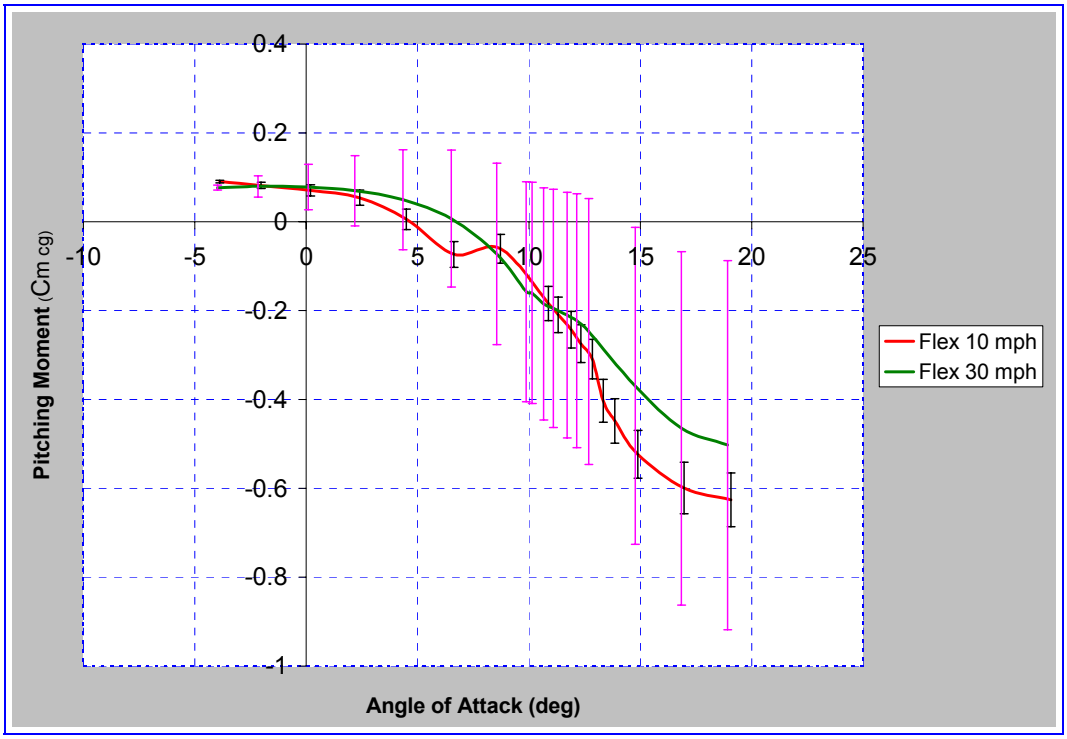

Figure 65. Flexible Wing MAV $C_{m\alpha}$ with CG Error Bars

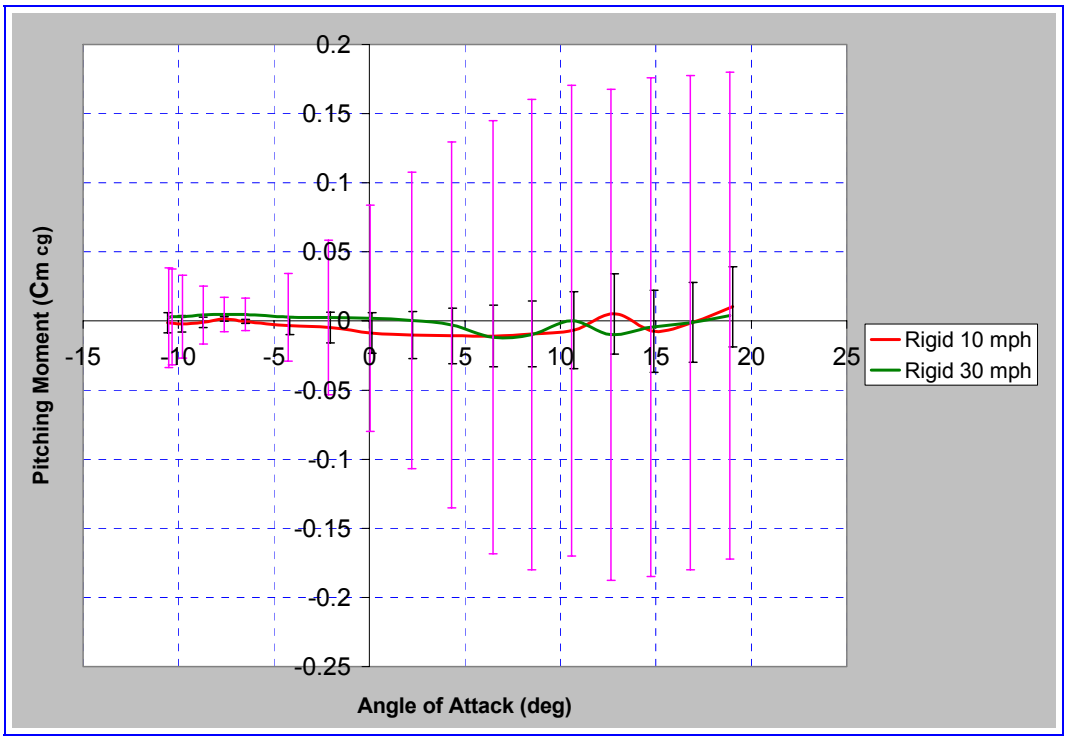

Figure 66. Rigid Wing MAV $C_{m\alpha}$ with CG Error Bars

The next plot, Figure 67, shows the change in rolling moment with angle of attack, $C_{\ell\alpha}$, for different sideslip angles. The magnitude of the errors increase as β increases. In addition, the effect of moving the CG is greater at the lowest angle of attack and decrease as α increases. As the side of the MAV is turned into the flow, changes in x_{CG} appear to most heavily influence the errors. Figure 68 presents the rigid wing $C_{\ell\alpha}$ plot for the one sideslip angle tested. At the lowest angles of attack, the rigid wing MAV's rolling moment errors are not as large as the flexible wing MAV; however, they also do not taper off as much either. The effect of moving the rigid wing CG on $C_{\ell\alpha}$ appears to be more consistent than in the flexible wing MAV.

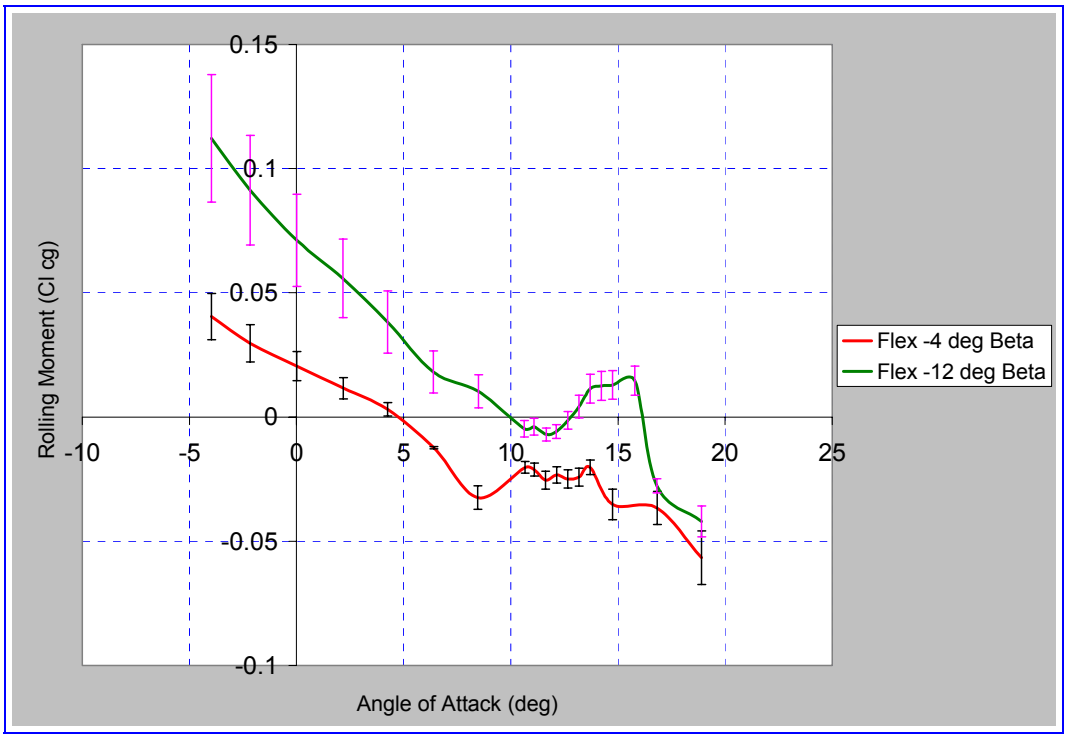

Figure 67. Flexible Wing MAV C_{ℓ_α} with CG Error Bars

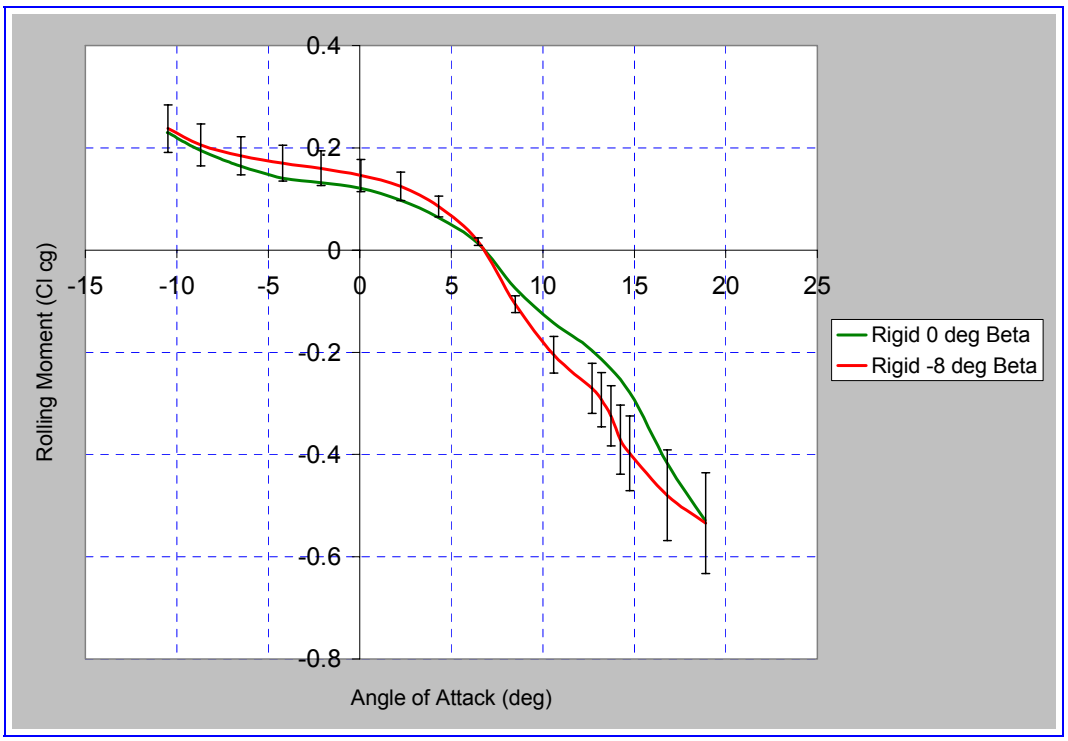

Figure 68. Rigid Wing MAV C_{ℓ_α} with CG Error Bars

Figure 69 shows the change in yawing moment with angle of attack, $C_{n\alpha}$, for different sideslip angles. Obviously, the placement of the CG has a large impact on the magnitude of $C_{n\alpha}$. The errors increase in size as the sideslip angle increases. Furthermore, the errors in each curve are exceptionally large in the trough where α_{stall} occurs. The change in the sideslip angle is in the same plane as the yawing moment is measured; thereby, increasing the susceptibility to changes in CG location. Figure 70 presents the rigid wing $C_{n\alpha}$ plot for the single sideslip angle tested. Not only is the shape of this curve materially different than the flexible wing MAV, but the location of the largest errors associated with a change in CG on the plot differ as well. The largest errors are from $\alpha = 0° - 8°$, and decrease appreciably near α_{stall}.

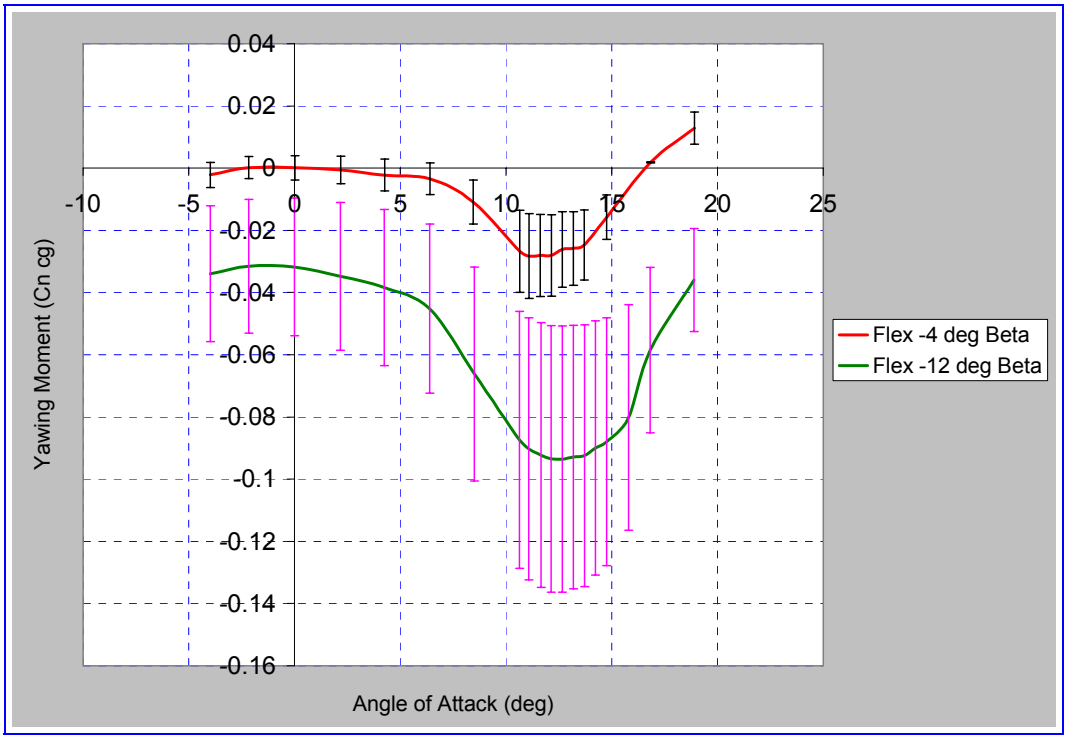

Figure 69. Flexible Wing MAV $C_{n\alpha}$ with CG Error Bars

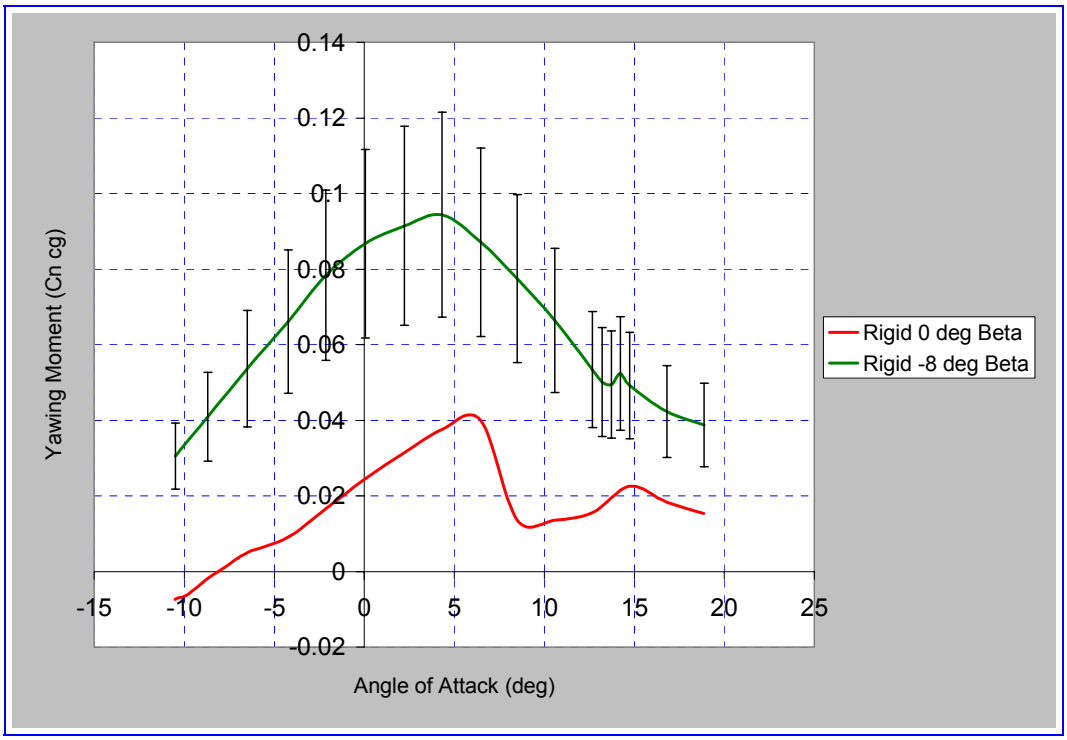

Figure 70. Rigid Wing MAV $C_{n\alpha}$ with CG Error Bars

Appendix F: Strain Gauge Sensors

Metal foil wire strain gauges are a series of thin wire filaments (≈ 0.008″ long) wound in a serpentine fashion attached to an epoxy bonded material. The wire material is selected based on the intended application i.e. high heat, long duration, high maximum loads, cyclic loading etc. These wire gauges are attached such that their longitudinal axis is in the same direction as the applied load. The purpose of looping the wires is to increase the effective length of wire under load, increasing the resistance. Figure 71 shows a standard wire strain gauge with 6 loops (12 wire lengths) and alignment placement tabs.

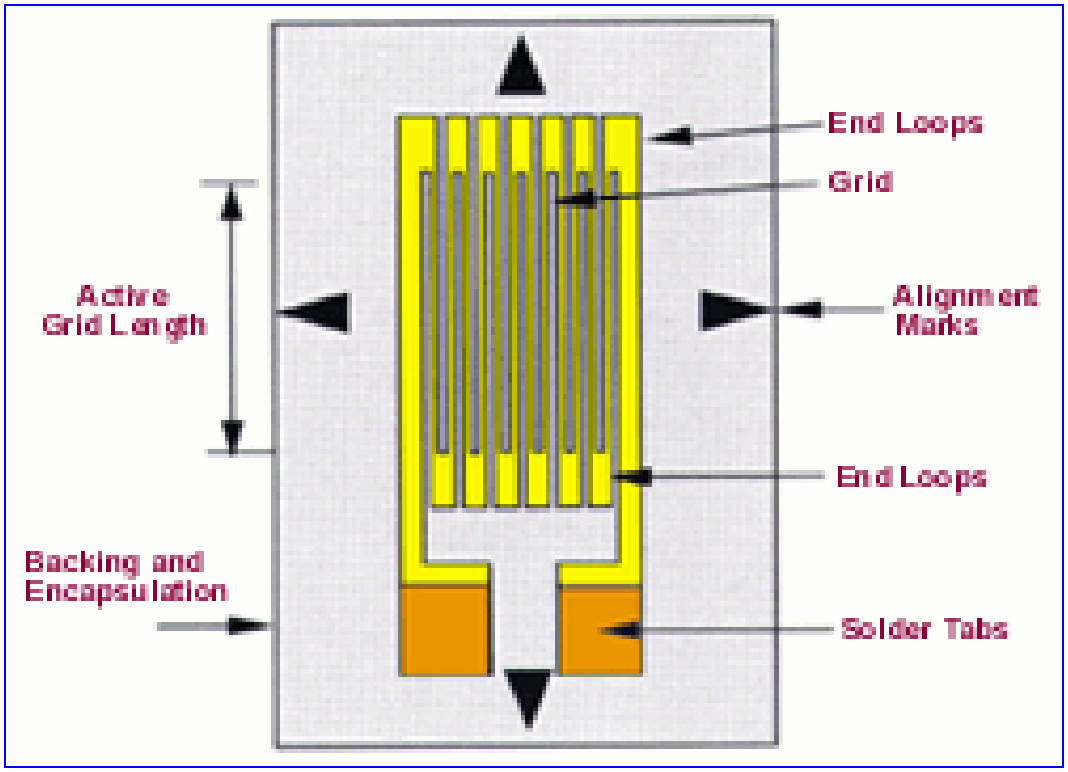

Figure 71. Typical Wire Foil Strain Gauge

The resistance of these wires is dependent on the material itself and is calculated by:

$$R = \rho * \frac{L}{A}$$

$$\begin{aligned} &where: \\ &\rho = resisivity - of - wire \\ &L = Lenth \\ &A = Cross - \text{sec}tional - area \end{aligned} \qquad \textbf{(38)}$$

The strain gauge is placed in a Wheatstone Bridge configured similarly to Figure 72. The bridge is comprised of resistors with a fixed resisivity place at 45° to one another. In Figure 72, resistor R_3 is actually the strain gauge, which has a variable resistance. Voltage is supplied continuously across the bridge, denoted by V_S, and the resulting output voltage, V_O, is measured across the middle legs of the bridge.

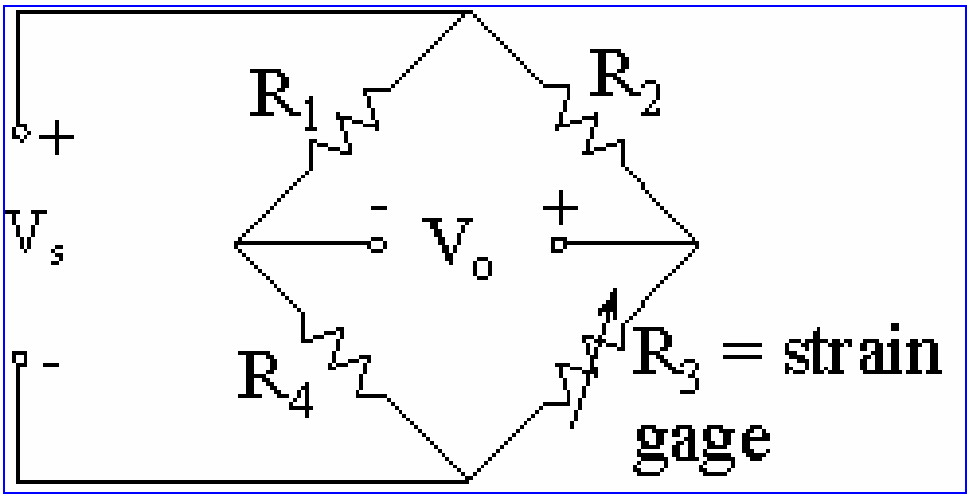

Figure 72. Strain Gauge / Wheatstone Bridge Set-Up

The output voltage is calculated by Ohm's law as follows:

$$V_O = V_S \frac{R_3 R_1 - R_4 R_2}{(R_3 + R_3)(R_1 + R_4)} \quad \textbf{(39)}$$

When no load is applied to the strain gauge, the resistance across each of the four sensors is equal, and the bridge is determined to be balanced, thus $V_O = 0$. However, when a load is applied to the object containing the stain gauge, the wire filaments elongate ($\uparrow \Delta L$), causing a decrease in the cross sectional area ($\downarrow \Delta A$), and an increase in the resistance across sensor R_3 by the amount ΔR_3. Taking the partial derivative of R with respect to L & A:

$$\begin{aligned} &\partial R = \frac{\partial R}{\partial L}\partial L + \frac{\partial R}{\partial A}\partial A \\ &\frac{\partial R}{\partial L} = \frac{\rho}{A} \\ &\frac{\partial R}{\partial A} = -\frac{\rho L}{A^2} \\ &\partial R = \frac{\rho}{A}\partial L - \frac{\rho L}{A^2}\partial A \end{aligned} \quad \textbf{(40)}$$

The strain gauge factor, SF, is given by:

$$\begin{aligned} &SF = \frac{\Delta R / R}{\varepsilon_i} \\ &where: \\ &\varepsilon_i = Strain \\ &\frac{\Delta R}{R} = (1 + 2\nu)\frac{\Delta L}{L} \\ &\nu = Poisson's Ratio \end{aligned} \quad \textbf{(41)}$$

Substitutiing the above results into Ohm's law results in:

$$V_O = V_S \frac{(R_3 + \Delta R_3)R_1 - R_4 R_2}{(R_2 + R_3 + \Delta R_3)(R_1 + R_4)} \approx V_S \frac{\Delta R_3 R_1}{(R_2 + R_3)(R_1 + R_4)} \quad \textbf{(42)}$$

Rearranging the definition for the strain gauge factor and solving for ΔR_3:

$$\Delta R_3 = SF * \varepsilon * R_3 \quad \textbf{(43)}$$

Substituting the above result into the equation for Ohm's law and solving for the strain:

$$\varepsilon = \frac{V_O}{V_S} \frac{1}{SF} \frac{(R_2 + R_3)^2}{R_2 R_3} = 4 \frac{V_O}{V_S} \frac{1}{SF} \quad \textbf{(44)}$$

The strain factor and input voltage are known constants supplied by the manufacturer, the output voltage is measured with the lab collection device; therefore, the strain is easily calculated. Once the strain is determined, Hooke's law can be used to calculate the stress, σ, in the material by:

$$\sigma = E * \varepsilon$$

$$\textit{where}:$$
$$E = \text{Material Modulus of Elasticity} \quad \textbf{(45)}$$

The force can be calculated from the stress in the material by the relation, F = σ*A. This force is the result output by the tunnel's LabView module for each strain gauge rosette.

Bibliography

Barlow, Jewel B., Rae, William H., and Pope, Alan. *Low-Speed Wind Tunnel Testing* (3rd Edition). New York: John Wiley and Sons, 1999

Biber, Kasim, Ol, M., and Tillman, C. "Some Examples of Airfoil Design For Future Unmanned Air Vehicle Concepts," *42nd AIAA Aerospace Sciences Meeting and Exhibit.* AIAA Paper 2004-1050, Istanbul, Turkey 34870 and Air Force Research Laboratory, Air Vehicles Directorate, Aeronautical Sciences Division, WPAFB OH. 5-8 January 2004.

Gad-el_Hak, Mohamed. "Micro-Air-Vehicles: Can They be Controlled Better," *Journal of Aircraft*, Vol 38:419-429 (May-June 2001).

Hosni, M.H., Coleman, H.W., Steele, W.G. "Application of Mathcad® Software in Performing Uncertainty Analysis Calculations to Facilitate Laboratory Instruction," Kansas State University, University of Alabama in Huntsville, Mississippi State University. n. pag.. http://www.mathcad.co.uk/mcadlib/apps/asee. 30 January 1998.

Jacob, J.D. "On the Fluid Dynamics of Adaptive Airfoils," *Proceedings of the 1998 ASME International Mechanical Engineering Congress and Exposition.* ASME paper, Anaheim Ca. 15-20 November 1998

Kellog, Michael I. and W. Jerry Bowman. "Parametric Design Study of the Thickness of Airfoils at Reynolds Numbers From 60,000-150,000," *42nd AIAA Aerospace Sciences Meeting and Exhibit.* AIAA Paper 2004-1054, Brigham Young University, Provo UT. 5-8 January 2004.

Keuthe, Arnold, M. and Chuen-Yen Chow. *Foundations of Aerodynamics-Bases of Aerodynamic Design* (5th Edition). New York: John Wiley & Sons, 1998.

McMichael, James M., and Michael S. Francis. (Col Ret). "Micro Air Vehicles – Toward a New Dimension in Flight," Online paper. n. pag. 18 December 1997 http://www.darpa.mil/tto/mav/mav_auvsi.html.

Mueller, Thomas J. "Aerodynamic Measurements at Low Reynolds Numbers for Fixed Wing Micro-Air-Vehicles," *To be presented at the RTO AVT/VKI special course on, "Development and Operation of UAVs for Military and Civil Applications"*. VKI Belgium, 13-17 September 1999.

Mueller, Thomas J. and Gabriel E. Torres. "Aerodynamic Characteristics of Low Aspect Ratio Wings at Low Reynolds Numbers," *Progress in Astronautics ans Aeronautics,* Vol 195:115-141, 2001.

Munday, D., Jacob, J., Huang, G. "Active Flow Control of Separation on a Wing with Oscillatory Camber," *40th AIAA Aerospace Sciences Meeting and Exhibit.* AIAA Paper 2002-0413, Reno NV, 14-17 January 2002.

Mustin, Jeff, 1st Lt, USAF. "Future Employment of Unmanned Aerial Vehicles," *Aerospace Power Journal,* 3rd Qtr:86-97, (Summer 2002).

Nechyba, Michael and Peter Ifju. "Towards Autonomous Flight of Micro Air Vehicles (MAVs): Vision-Guided Flight Stability and Control," Informational Briefing-Audience Unknown, Department of Electrical and Computer Engineering and Department of Aerospace and Mechanical Science, University of Florida, Gainesville Florida, 2002.

Nelson, Robert, C. *Flight Stability & Automatic Control* (2nd Edition). Boston: McGraw Hill Press, 1998

Subramanian, C. S. Class Handout , Aero 627, Introduction to Turbulence. School of Engineering and Management, Air Force Institute of Technology, Wright-Patterson AFB OH. Winter Qtr 2003.

Tennekes, H. and J.L. Lumley. *A First Course in Turbulence*. Cambridge: The MIT Press, 2001.

Waszak, Martin R and Luther N. Jenkins. "Stability and Control Properties of an Aeroelastic Fixed Wing Micro Aerial Vehicle," *AIAA Atmospheric Flight Mechanics Conference.* AIAA Paper 2001-4005, Montreal Canada, 6-9 August 2001.

White, Frank, M. *Fluid Mechanics* (2nd Edition). New York: McGraw-Hill Press, 1986

Vita

Captain Anthony M. DeLuca was born in Sterling Heights, Michigan. He graduated from Henry Ford II High School in Utica, Michigan in 1991. He received an appointment to the United States Military Academy in West Point, New York and graduated with a Bachelor of Science degree in Mechanical Engineering in June 1995. Upon graduating from West Point, he was one of seven selected out of twenty-five for a commission in the Air Force.

His first assignment was at Kirtland AFB, New Mexico from September 1995-February 1999. He was assigned to the Space and Missile Test directorate of the Head Quarters Air Force Operational Test and Evaluation Center (AFOTEC). He held numerous positions at AFOTEC and won the 1998 Company Grade Officer of the Year. While at Kirtland, Captain DeLuca enrolled in the Albuquerque Campus of the University of Phoenix where he earned a Masters of Business Administration in Technology Management degree in February of 1999.

His second assignment was at Eglin AFB, Florida from March 1999-August 2002. He was assigned to the Area Attack Systems Program Office (SPO) of the Air Armament Center (AAC) as a Systems Engineer. He served as the BRU-57 *Smart Rack* Systems and Developmental Test Engineer until 2001 and then as the Joint Standoff Weapon (JSOW) Lead Systems Engineer. In September 2002, Captain DeLuca entered the School of Engineering and Management, Air Force Institute of Technology, Wright-Patterson AFB, OH.

REPORT DOCUMENTATION PAGE

Form Approved
OMB No. 074-0188

1. REPORT DATE *(DD-MM-YYYY)*	**2. REPORT TYPE**	**3. DATES COVERED** *(From – To)*
23 Mar 04	**Master's Thesis**	September 2002 – March 2004

4. TITLE AND SUBTITLE

EXPERIMENTAL INVESTIGATION INTO THE AERODYNAMIC PERFORMANCE OF BOTH RIGID AND FLEXIBLE WING STRUCTURED MICRO-AIR-VEHICLES

5a. CONTRACT NUMBER

5b. GRANT NUMBER

5c. PROGRAM ELEMENT NUMBER

6. AUTHOR(S)

DeLuca, Anthony, M., Captain, USAF

5d. PROJECT NUMBER
ENR #2003-046

5e. TASK NUMBER

5f. WORK UNIT NUMBER

7. PERFORMING ORGANIZATION NAMES(S) AND ADDRESS(S)
Air Force Institute of Technology
Graduate School of Engineering and Management (AFIT/EN)
2950 Hobson Way
WPAFB OH 45433-7765

8. PERFORMING ORGANIZATION REPORT NUMBER

AFIT/GAE/ENY/04-M06

9. SPONSORING/MONITORING AGENCY NAME(S) AND ADDRESS(ES)
Air Force Research Lab / MNAV
Attn: Lt. Michael Simonich (for Maj. John Anttonen)
1865 4th Street
Eglin AFB, FL 32542 DSN: 872-8876 ext. 3335

10. SPONSOR/MONITOR'S ACRONYM(S)
AFRL/MNAV

11. SPONSOR/MONITOR'S REPORT NUMBER(S)

12. DISTRIBUTION/AVAILABILITY STATEMENT
APPROVED FOR PUBLIC RELEASE; DISTRIBUTION UNLIMITED.

13. SUPPLEMENTARY NOTES

14. ABSTRACT

The Air Force Research Lab, Munitions Directorate, Eglin Air Force Base, Florida has designed a man-portable carbon-fiber Micro-Air-Vehicle (MAV) used for on-the-spot surveillance by Special Operations Forces (SOF) for enemy reconnaissance as well as post-strike Battle Damage Assessment (BDA).

The main goals of this experiment are: 1) characterize the flow quality of the new AFIT 3' x 3' wind tunnel and 2) determine the aerodynamic performance characteristics of the 24″ span, 6″ chord flexible and rigid wing MAVs. The turbulent intensity of the wind tunnel was approximately 2%. Both MAVs had an average lift slope within 3.5% of the theoretical value. Flexible wings deformed in response to perturbations in local flow field conditions, promulgating the delay of wing stall by nearly double. Aeroelastic effects begin to dominate low speed, laminar Reynolds number effects at tunnel velocities greater than 30 miles per hour. The flexible wing MAV displayed static stability in all three principal control axes (Pitch, Roll, Yaw), while the rigid MAV was not definitively stable in any axis. All flexible wing control surface configurations resulted in predictable and consistent performance between -10° and +10° elevon deflection. Reponses declined steadily after ±10° showing dramatic direction changes.

15. SUBJECT TERMS
Test Methods, Wind Tunnel Tests, Wind Tunnels, Air Force Research, Thin Wings, Test Facilities, Aeroelasticity

16. SECURITY CLASSIFICATION OF:			**17. LIMITATION OF ABSTRACT**	**18. NUMBER OF PAGES**	**19a. NAME OF RESPONSIBLE PERSON**
REPORT	**ABSTRACT**	**c. THIS PAGE**			Dr. Mark F. Reeder
U	**U**	**U**	**UU**	174	**19b. TELEPHONE NUMBER** *(Include area code)* (937) 255-3636, ext 4530; e-mail: Mark.Reeder@afit.edu

Standard Form 298 (Rev: 8-98)
Prescribed by ANSI Std. Z39-18